NOVA SCHOOL OF SCIENCE & TECHNOLOGY

DEPARTAMENT OF
Material Sciences

Filipe Amaral Lopes

BSc in Mining and Geo-Environmental Engineering

PARTICLE SIZE ANALYSIS AND 3D MODELING OF MINERALS FOR MINERAL PROCESSING OPTIMIZATION: A CASE STUDY OF NEVES-CORVO

MASTER IN Advance Materials: Innovative Recycling

NOVA University Lisbon

4 November, 2023

NOVA SCHOOL OF
SCIENCE & TECHNOLOGY

DEPARTAMENT OF
Material Sciences

PARTICLE SIZE ANALYSIS AND 3D MOD-ELING OF MINERALS FOR MINERAL PROCESSING OPTIMIZATION: A CASE STUDY IN NEVES-CORVO

Filipe Amaral Lopes

BSc in Mining and Geo-Environmental Engineering

Adviser: José António de Almeida
Associated Professor with Habilitation of the FCT - NOVA University of Lisbon

Co-advisers: Carla Candeias
Auxiliar Researcher, Geosciences Department, GeoBioTec, University de Aveiro.

Examination Committee:

Chair: Dr. Alexandre José da Costa Velhinho,
Assistant Professor, FCT-NOVA

Rapporteurs: Dr. Joaquim Eduardo Sousa Goís,
Assistant Professor, FEUP

Adviser: José António de Almeida
Associated Professor with Habilitation of the FCT - NOVA

MASTER IN Advance Materials: Innovative Recycling

NOVA University Lisbon
4 of November, 2023

PARTICLE SIZE ANALYSIS AND 3D MODELING OF MINERALS FOR MINERAL PROCESSING OPTIMIZATION: A CASE STUDY OF NEVES-CORVO

To my parents...

ACKNOWLEDGMENTS

I would like to acknowledge the people who have helped me in the making of my thesis. This work would not exist without them.

I would like to extend my heartfelt gratitude to SOMINCOR for their invaluable contribution of minerals. Your generosity in providing these materials is greatly appreciated, and it will undoubtedly play a pivotal role in advancing my research.

I am deeply grateful to Professor Alexandre Velhinho for seeking and finding a thesis topic amongst his peers.

I would like to express my most sincere gratitude to Professor José Almeida. He offered me the possibility of working under his guidance when I needed it the most. I have learned so much from his expertise and work on the topic of geostatistics.

I extend my gratitude to Eng. Carlos Galhano, for helping me in the lab cutting the samples into smaller ones, although not directly within the scope of supervision, have significantly aided in advancing the research.

The support and resources extended by the University of Aveiro, under the guidance of Professor Carla Candeias, are also gratefully acknowledged.

I would also like to thank Eng.ª Cristina Sequeira, from UA/GeoBioTec, who carried out all the analyses and maps of the samples.

I would like to sincerely thank my parents, Graça and Silvio, for the important role they played throughout the redaction of this thesis, my studies, and my life in general. They constantly believed in me, even when I didn't, they loved me and have supplied me with large quantities of coffee for as long as I can remember. I have no words to express my gratitude.

A special thanks to my brother José, for putting up with me while I wrote this project, for all the help he gave me and for his companionship.

Finally, I would like to mention the many friends with whom I have shared my academic journey. Those who provided their advice for this work, those who helped me in my darkest moments, and those with whom we leave our fate to the roll of a die.

"Life before death. Strength before weakness. Journey before destination."

Brandon Sanderson

ABSTRACT

This pilot study focused on the characterization and quantification of grains for the metals copper (Cu), lead (Pb), and zinc (Zn) in samples collected from the Neves-Corvo mining complex (Alentejo, Portugal). Six samples of sulphide ores were carefully prepared and analysed using a scanning electron microscope with Energy Dispersive Spectroscopy (SEM-EDS) for semi-quantification through mapping of Cu, Pb, and Zn. Out of these six samples, three were selected, and SEM-EDS images were transformed into binary representations for the sulphide grains of these metals.

Subsequently, these images were binarized, and their basic statistics and experimental variograms were evaluated. This phase of the work was concluded with the fitting of a theoretical variogram model. Considering that SEM-EDS images are two-dimensional, and the assessment of grain size is three-dimensional, in the next step, simulated images of the presence of mineral particles or the surrounding matrix were generated. The simulated images represent the three-dimensional construction by modelling the morphology of the relationship between ore particles and the matrix. With these simulated images, an evaluation was carried out regarding the relationship between grain size (hypothetical milling) and grain purity (fraction of metallic sulphide particles or matrix) for three purity levels.

The preliminary findings from this study based on the simulated images are promising, indicating the effectiveness of this approach in improving flotation efficiency in relation to the dimensions of sulphide particles.

Keywords: Sulphide ores, stochastic simulation, sequential indicator simulation, ore concentration optimization

RESUMO

Este estudo piloto concentrou-se na caracterização e quantificação de grãos dos metais cobre (Cu), chumbo (Pb) e zinco (Zn) em amostras coletadas no complexo mineiro de Neves-Corvo (Alentejo, Portugal). Utilizaram-se seis amostras de minérios de sulfuretos que foram cuidadosamente preparadas e analisadas por meio de microscópio eletrônico de varrimento com Espectroscopia de Energia Dispersiva (SEM-EDS) para a semi-quantificação por mapeamento de Cu, Pb e Zn. Dessas seis amostras, foram selecionadas três, para as quais as imagens SEM-EDS foram transformadas em representações binárias para os grãos de sulfuretos desses metais.

Posteriormente, essas imagens foram binarizadas, determinaram-se os seus estatísticos básicos e variogramas experimentais. Essa fase do trabalho foi concluída com o ajuste de um modelo teórico de variograma. Considerando que as imagens do SEM-EDS são bidimensionais e a avaliação da dimensão do grão é tridimensional, na etapa seguinte, foram simuladas imagens da presença das partículas minerais ou da matriz envolvente. As imagens simuladas representam a construção tridimensional pela modelação da morfologia da relação entre as partículas de minério e a matriz. Com essas imagens simuladas, procedeu-se à avaliação da relação entre a dimensão do grão (hipotética moagem) e a pureza do grão (fração de partículas de sulfuretos metálicos ou matriz) para três graus de pureza.

As descobertas preliminares deste estudo a partir das imagens simuladas são promissoras, indicando a eficácia desta abordagem em melhorar a eficiência da flutuação em relação às dimensões das partículas de sulfuretos.

Palavras chave: Minérios de sulfuretos, simulação estocástica, simulação sequencial da indicatriz, otimização da concentração de minérios

CONTENTS

LIST OF FIGURES

LIST OF GRAPHS

LIST OF TABLES

LIST OF Equations

ACRONYMS

SEM-EDS	Scanning Electron Microscopy with Energy Dispersive Spectroscopy
GRID	Geostatistical Resource Information and Display

1 INTRODUCTION

This initial section is intended to elucidate the context, objectives, and structure of this dissertation.

1.1 Context

The evolution of geostatistics, marked by transformative milestones, has emerged as a cornerstone in decoding the enigmatic phenomena that shape our planet. Georges Matheron's visionary ingenuity in the 1960s began the journey, revealing the nuances of spatial continuity with variograms and providing us with the ability to quantify spatial variability. In the 1970s, the introduction of the kriging method, redefining the way we estimate resources, exploiting the complexities of the spatial fabric to predict values even in uncharted territories.

As the decades passed, the 1980s witnessed geostatistical accessibility flourishing with the advent of user-friendly software such as GSLIB, while the 1990s wove the threads of geostatistics and Geographic Information Systems (GIS) into a rich tapestry of spatial knowledge. In the 21st century, the adoption of multivariate and spatio-temporal methodologies, coupled with the ability to meet the challenges posed by large volumes of data, has reinforced geostatistics as an invaluable tool for navigating the complexities of geological data.

In the dynamic arena of mineral extraction, where efficiency and sustainability collide, the implications of suboptimal analysis of ore grains extend far and wide. It is here, during the intricate dance of particles, that the aim of this work shines through to estimate the size of ore grains and barren grains. It is also important to note that the minerals under investigation were obtained directly from the Neves Corvo Mine, giving the study real authenticity. Before starting the geostatistical analysis, a meticulous scanning electron microscopy (SEM) analysis was carried out, adding a layer of precision to the subsequent geostatistical efforts.

This SEM analysis serves as the foundation on which the geostatistical methodology will be constructed, infusing empirical knowledge into the process. The goal is profound yet pragmatic - to assess when to begin the intricate process of fragmentation, an artistic ballet that has the potential to unlock efficiency and minimize waste. This undertaking transcends mere analysis; it holds the power to orchestrate the symphony of mineral processing with finesse, optimizing yield and minimizing environmental impact.

The path to this goal finds its foundations in the field of Geostatistics - a discipline that has matured from its nascent statistical roots into a tool of unparalleled sophistication, ready to unravel the mysteries of grain size estimation and guide the hands of extraction in harmony with the rhythms of our planet. As we embark on this journey, the resonance of geostatistics, together with the goal of optimizing

fragmentation, is destined to echo far beyond the confines of the laboratory and the mine, resonating in the realms of economic growth, environmental management, and sustainable progress.

The method of constructing variograms based on scanning electron microscopy (SEM) images of ores plays a crucial role in the characterization and analysis of mineral samples. This significantly contributes to understanding the spatial distribution of mineral elements in each sample, providing crucial insights into mineralogical heterogeneity. The ability to examine variations in mineral concentration as a function of geographical position is particularly relevant to the mining industry, aiding in the identification of areas with the highest potential concentration of minerals and guides the development of more effective exploration strategies.

The ore concentration analysis method, which allows detailed analysis of the geological and mineralogical characteristics of samples, provides essential information for making informed decisions in mining operations and mineral resource management. By revealing the stability and randomness in the distribution of minerals in each sample, it contributes to a better understanding of the complexity of geological formations.

1.2 Overview of Industrial Uses and Main Ores of the Studied Metals

1.2.1 Copper

Copper is a metal of great importance to industry, finding diverse applications in construction, electronics, healthcare and more. It is among the most widely used metals globally, with substantial economic value (Advameg, s.d.).

Chalcopyrite stands out as the most common mineral worldwide. The EU countries collectively possess a total reserve base of approximately 41 Mt of copper, enhancing the significance of the European community in the global market, even though this share constitutes less than 5% of global reserves (Krzak, 2021).

In civil construction, copper is utilized for electrical wires and cables due to its high electrical conductivity, enhancing energy transmission efficiency. Its corrosion-resistant nature makes it ideal for outdoor applications like building facades and roofs. Additionally, its resistance properties make it suitable for plumbing systems, ensuring longer service life for pipes.

In industry, copper is crucial for manufacturing metal alloys such as bronze and brass. Bronze, an alloy of copper and tin, is used in the manufacture of musical instruments, decorative pieces and status items. Brass, an alloy of copper and zinc, finds applications in household utensils such as taps, door handles and keys. Copper is also a key material in electronic equipment manufacturing, especially printed circuit boards, owing to its high electronic conductivity and ability to moldability (electronicstakeback, 2008).

In healthcare, copper plays a vital role in medical applications, including surgical equipment and prostheses. Its antimicrobial properties make it useful in preventing hospital-acquired infections. Copper is also used in food supplements and medicines to treat nutritional deficiencies like anemia.

Copper recycling in Europe is a robust and sustainable endeavour taking place across the continent. Recycling facilities in urban centres and industrial zones efficient collect and process copper scrap from various sources, including electrical wiring, plumbing components, and discarded electronic devices. This environmentally conscious efforts in Europe not only reduces the demand for primary copper production but also minimize waste, energy consumption, and greenhouse gas emissions, aligning with the region's commitment to a circular economy and environmental preservation (Copper allience, 2022).

In various applications, copper holds significant economic importance, being one of the most utilized metals globally with a yearly estimated global footprint in the millions of tons.

1.2.2 Zinc

Zinc is a metal of great significance to the industry, finding diverse applications in construction, electronics, healthcare, and more. It ranks among the most widely used metals globally, possessing substantial economic.

Zinc, the 23rd most abundant element in the earth's crust, is primarily sourced from sphalerite, a zinc sulphide (National Minerals Information Center, 2023). According to the USGC, in Europe, Russia and Sweden are the prominent players in zinc production and reserves (Tolcin, 2023).

In the construction industry, zinc is extensively utilized in the production of corrosion-resistant roof tiles and ruffles, due to its malleability. It serves as coating to protect metal structures, enhancing their durability.

In industry, zinc plays a pivotal role in manufacturing metal alloys like brass, which is a combination of copper and zinc used for household items such as taps, door handles, and keys. Galvanization, a process involving coating metals with zinc, is widely applied to protect against corrosion, particularly in automotive and construction applications.

In electronics, zinc is crucial for discharge batteries, including lithium-ion batteries widely used in electronic devices such as smartphones, tablets, and laptops. It is also employed in the production of electronic components like connectors and circuitry (electronicsforu, 2020).

In healthcare, it is essential for the functioning of the immune system and for the wound healing process. It is used in food supplements and medicines to treat nutritional deficiencies, such as zinc deficiency. It is used in creams and ointments to treat acne and other skin conditions (ODS, 2022).

In Europe, zinc recycling is a contribution to sustainable practices, demonstrating the region's commitment to environmental conservation. Recycling facilities in urban centres and industrial zones efficiently collect and process zinc scrap from a myriad of sources, including galvanized steel, batteries, and old metal goods. Through meticulous sorting, refining, and processing, high-quality zinc is recovered. These eco-friendly practices not only reduce the dependency on primary zinc production but also minimize waste, energy consumption, and greenhouse gas emissions, aligning with Europe's pledge to a circular economy and environmental preservation (Monier, et al., 2017).

Due to its widespread applications, zinc holds significant economic importance, with an estimated global footprint in the millions of tons per year.

1.2.3 Lead

Lead is a vital metal with diverse applications across various sectors, including construction, manufacturing, energy storage, and health. The most abundant lead mineral is galena, and countries like Russia, Sweden, and Turkey have substantial lead reserves (Tolcin, 2022).

In construction, lead's malleability and corrosion resistance make it a preferred material for roofing, flashing, and waterproofing walls. Despite reduced use due to environmental concerns, lead's durability and ability to create tight seals remain noteworthy.

In industry, lead finds its place in the production of batteries. Lithium-acid batteries have been widely used to store and supply electrical energy in applications ranging from automotive vehicles to backup power systems. These batteries are known for their reliability and cost-effectiveness, making them essential for a variety of industries.

Lead's affordability and low melting point contribute to its significance in manufacturing, being used in the production of items like ammunition, radiation protection, and cabin lining. Its ability to absorb vibrations and dampen sound adds value in the manufacture of machine components.

The economic value of lead extends to the energy sector, where it is utilized in photovoltaic solar cells, contributing to energy production through sustainable means.

In the field of healthcare, the historical applications of lead have evolved from its early uses to recognizing it as a hazardous substance. Lead poisoning poses severe health risks, particularly for children, leading to its prohibition in various consumer products such as paint and petrol. Current efforts are directed at minimizing exposure to lead and addressing its detrimental health impacts.

Lead recycling in Europe plays a significant role in promoting environmental sustainability. Recycling facilities strategically located in urban centres and industrial zones facilitate the efficient collection and processing of lead scrap. This scrap originates from various sources, including lead-acid batteries, old plumbing, and electronic components. Rigorous sorting, processing, and refining methods are employed to recover high-quality lead. These environmentally conscious initiatives not only diminish reliance on primary lead production but also contribute to waste reduction, energy conservation, and a decrease in greenhouse gas emissions (Monier, et al., 2017).

1.3 Objectives

This dissertation aims to test if geostatistical methods can optimize the processing plant and flotation cells, while also demonstrating the feasibility of using these methods to predict the sizes of minerals in the study, including Cu, Pb, and Zn.

The specific objectives include:

1) **Data Collection and Sample Preparation**:

    a) Conducting detailed SEM-EDS mapping of the selected ore samples to generate high-resolution mineralogical maps at the grain scale.

2) **Variogram Analysis**:

   a) Applying geostatistical techniques to create variograms from SEM data.

   b) Analysing spatial dependencies and correlations to understand the distribution of mineral grain sizes.

3) **Geostatistical Simulation**:

   a) Employing Sequential Indicator Simulation (SIS) to predict the distribution of valuable grain minerals within the samples.

   b) Calculating the probabilities of obtaining desired mineral grades at various mesh sizes.

   c) Proposing optimization strategies based on the generated data.

These objectives form the framework of this report, enabling a comprehensive exploration of geostatistics in characterizing mineral grain sizes and optimizing mineral processing for valuable mineral recovery.

1.4 Document Organization

This thesis is structured into six core sections, commencing with the "Introduction," which provides a comprehensive overview of the research's context, objectives, and the elements under scrutiny. The subsequent section, "Framework," delves into the geological, geographic context, ore types, mining and concentration methods and the processing plant. Section "Methods and Theory" follows, focusing on the theoretical foundations of mining techniques, geostatistics and SEM-EDS analysis. The four sections, "Case Study," details data descriptions, processing, and simulation results. Section five, "European Institute of Innovation & Technology (EIT)," assesses the project's ecological implications and its potential for enhancing sustainability. Lastly, section "Final Remarks" encapsulates conclusions and future research directions.

2 FRAMEWORK

In this section of the dissertation, we delve into the foundational aspects of the Neves-Corvo Mine, establishing its geographic and geological framework. Our exploration encompasses an in-depth analysis of the diverse types of mineralization found within the mine, including massive sulphides and fissure-type mineralization (stockwork). Also, it delved deeper into the mining world, exploring the principles of mining and concentration methods. Additionally, it evaluates the intricate workings of the processing plant.

2.1 Geographic Framework

The Neves-Corvo Mine, situated within the western expanse of the Iberian Pyrite Belt spanning southern Spain and Portugal, serves as a testament to the geological wealth inherent in this region. Nestled within the Alentejo province of southern Portugal, the mine's strategic location places it approximately 15 kilometres southeast of the town of Castro Verde. This region, steeped in a rich history of mineral exploration and extraction, contributes significantly to the mineral resources of southern Europe (lundinmining, s.d.).

The Neves-Corvo Mine is located between the parishes of Santa Bárbara de Padres and Senhora da Graça de Padres, within the municipalities of Castro Verde and Almodóvar. Geographically, the mine's coordinates pinpoint its precise location at a latitude of 37° 34 '25"N and a longitude of 07° 58' 20"W within UTM Zone 29S, corresponding to UTM coordinates 590757E and 59004N. This geographical positioning aligns the Neves-Corvo Mine with the larger tapestry of geological formations and landscapes that have shaped this part of the Iberian Peninsula (Figure 2.1).

The mining operation, orchestrated by the collaboration between the Portuguese state and SOMINCOR, unfurls within a concession area spanning 28 square kilometres. The Neves-Corvo ore body has copper, zinc, and silver deposits that can be explored and exploited by this vast expanse. The breadth of the mining concession, coupled with the extensive prospecting area encompassing around 140 square kilometres, underscores the potential mineral bounty residing beneath the surface (Figure 2.2).

Figure 2.1 – Neves Corvo Mine, marked with a distinctive red dot on the map of Portugal. (lundinmining, s.d.)

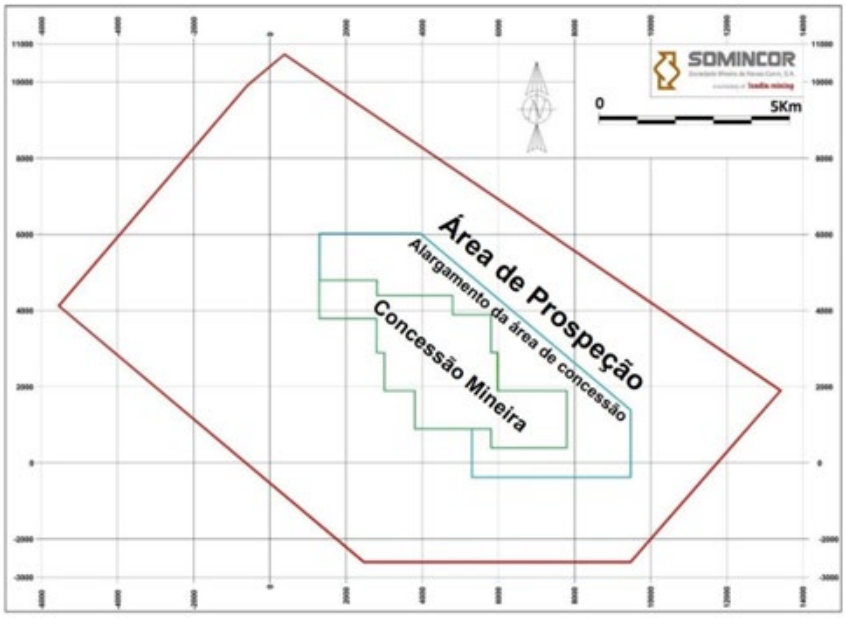

Figure 2.2 – Prospecting area of SOMINCOR (lundinmining, s.d.)

The climate in Castro Verde, Portugal, exhibits notable variations throughout the year, defining distinct seasons. In the summer months of June to August, the region experiences elevated temperatures, with average highs reaching 30°C and low precipitation. Winter, spanning from December to February, sees decreasing temperatures, with average lows nearing 5°C, and increased precipitation, particularly in

December. Spring and autumn, characterized by moderate temperatures ranging between 10°C and 20°C, showcase transitional features. Overall, Castro Verde's climate displays marked seasonality, featuring hot and dry summers, cold and wet winters, and intermediary seasons marked by gradual transitions in temperature and precipitation.

The influence of Castro Verde's climate is evident in seasonal patterns that impact local activities and the natural environment. Warm and dry summers facilitate outdoor activities like agriculture and tourism, although limited rainfall may affect water resource availability. On the other hand, colder and wetted winters contribute to soil revitalization and aquifer recharge, crucial for regional agriculture. The intermediary seasons provide diverse climatic conditions, enabling a gradual adaptation to seasonal changes. In summary, Castro Verde's distinctive climate not only shapes local lifestyles but also influences the ecology, economy, and culture of the region (lundinmining, s.d.).

2.2 Geological Framework

2.2.1 Regional Framework

The Neves Corvo Mine is situated in South Alentejo, within the Iberian Pyrite Belt (IPB), recognized as the most significant province of polymetallic volcanic sulfuric masses globally based on the mineralogical area's size and the substantial number of deposits, including eight deposits each exceeding 100Mt.

The South Portuguese Zone (SPZ) holds geological importance, covering a substantial portion of the southern Iberian Peninsula known as the South Portuguese Zone (Zona Sul Portuguesa or ZSP). With an about extension of 250 kilometres in length and variable widths ranging from 30 to 50 kilometres, the SPZ stretches from the northern vicinity of Grândola in Portugal to the vicinity of Seville in Spain. The SPZ exhibits an orientation shift, transitioning from a north-south orientation north of Grândola to an east-west direction near the Spanish border, maintaining this orientation up to Seville.

The SPZ's present-day area was occupied by a shallow sea during the Upper Devonian period, resembling the North Sea, with a width exceeding 200 kilometres. The conclusion of the Devonian era marked the initiation of tectonic extension within the continental crust underlying this sea. This extension led to the development of deep-seated faults that introduced a horst and graben-style tectonic regime. These tectonic features served as conduits for mantle-derived magmas, which interacted with crustal materials to form many volcanic structures.

As a result of this tectonic regime, subsiding grabens created basins on the seafloor, serving as repositories for fine sediments, intercalated black shales, and volcanic products. Volcanic rocks accumulated to considerable thicknesses, up to 500 meters, in proximity to volcanic centres, while distal regions witnessed the deposition of fine volcaniclastic materials mingled with terrigenous sedimentation.

The paleogeographic setting facilitated the proliferation of siliceous-shelled microorganisms (radiolarians), leading to accumulations of cherts and jaspers. The sedimentary strata of the Mértola Formation, within which the presence of goniatites provides chronological constraints, dates the formation to the Late Visean Age. The Late Visean period marked a transition in geodynamic conditions,

shifting from a distensive to a compressional regime due to the Variscan Orogeny, triggered by the closure of the Rheic Ocean and the collision of Laurussia and Gondwana supercontinent.

This tectonic transition induced inversion, potentially triggered by the collision between the SPZ and the Ossa-Morena Zone (Zona Ossa Morena or ZOM), juxtaposed through the Ferreira-Ficalho thrust. This tectonic event led to the uplift of the sea bottom, resulting in widespread exposure and extensive terrestrial erosion. The eroded materials were transported to the southern oceanic realm, culminating in the deposition of the Lower Alentejo Flysch Group.

From a scientific standpoint, the SPZ's significance lies in its abundant volcanic-hosted massive sulphide (VHMS) deposits, boasting notable world records for VHMS occurrences. The SPZ hosts over 1700 million tons of ore distributed across 90 deposits, encompassing the largest VHMS deposit (Rio Tinto) and the highest copper and tin grades (Neves Corvo). The VHMS deposits within the SPZ are dated to approximately 359 million years corresponding to the Late Devonian period.

In terms of lithostratigraphy, the SPZ includes the Filito-Quartzitic Group (PQ Group) at the base, overlain by the Volcano-Sedimentary Complex (CVS) characterized by alternating sedimentary and volcanic rocks. The Flysch Group is represented by the Mértola Formation, comprising a turbiditic succession of black shales and graywackes, reaching thicknesses exceeding 3000 metres.

Within Portuguese territory, the SPZ exhibits two distinct branches: the northern and southern branches. The northern branch constitutes an essentially autochthonous region marked by complex tectonic thrusting. In contrast, the southern branch encompasses the anticlinal structure of Panóias, housing three principal anticlines, including the Rosário/Neves Corvo anticline. The Neves Corvo mine occupies the southeastern terminus of this anticline (Alexandra Gomez Escobar, 2021) (Oliveira, et al., 2013).

2.2.2 Methanogenesis and Mineralization’s

Considering both massive sulphides and stockwork mineralization’s at Neves-Corvo Mine, the cumulative tonnage of polymetallic sulphides in the Iberian Pyrite Belt (IPB) exceeds 2,500 million metric tons (Mt), distributed across approximately 88 giant deposits (over 100 Mt) and supergiant deposits (over 200 Mt; e.g., Neves-Corvo). All dated deposits within the IPB indicate that the hydrothermal activity responsible for mineralization predominantly occurred between the Famennian and the end of the Tournaisian. (Rosa, et al., 2008) (Moura, 2008)

Chemical sediments of siliceous nature of hydrothermal origin are present at various stratigraphic levels of the Central Volcanic Sequence (CVS), marking the mineralized horizons both above massive sulphides and laterally. The hydrothermal sediment facies are represented by red hematitic jaspers (affected by reducing alteration) above the mineralized bodies, which are valued as effective prospecting criteria. (Oliveira, et al., 2013)

From a geochemical perspective, the Neves-Corvo deposit is exceptional within the metallogenic province and globally (Oliveira, et al., 2013). The geochemistry of the massive sulphide ores at Neves-Corvo contrasts with typical IPB deposits. The copper content and its ratio ($100Cu / (Cu + Zn) > 50$) significantly deviate from the characteristic values in this province ($15 < 100Cu / (Cu + Zn) < 25$). Valuable high concentrations of copper and zinc draw attention to the presence of concentrate-

enhancing elements such as silver and indium. The mineralization results from the protracted activity of a hydrothermal system with multiple fluid and metal contributions, dividing into two main mineralizing episodes: i) an early episode leading to massive cassiterite precipitation and ii) a subsequent episode that generated the massive sulphides.

In the case of hydrothermal origin deposits, the paragenetic sequence exhibits common characteristics and follows the order in terms of decreasing geochemical metal abundance. Oxides form in the first phase of mineralized fluid evolution, followed by the formation of iron, zinc, and copper sulphides, and, later, silver precipitation. Gold is one of the last elements to precipitate. It should be noted that each deposit possesses a unique paragenetic sequence (Oliveira, 2013).

Massive Sulphides – The massive sulphides at Neves-Corvo occur interbedded with the black shales of the Neves Formation in zones with significant silicate content. These lenses of massive sulphides are interconnected and form a single mineralization horizon at Neves-Corvo. Pyrite is the most abundant mineral, followed by chalcopyrite (Moura, Metallogenesis at the Neves Corvo VHMS deposit (Portugal): A contribution from the study of fluid inclusions, 2008).

Fissured-Type Mineralization – The fissured-type mineralization (or stockwork), occurring adjacent to the massive sulphides, is of the stockwork type and is associated with the black shales of the hanging wall and underlying acidic tuffs. It exhibits vein-like characteristics, generally discordant with the deposit's macrostructure. The veins and veinlets have variable thickness and intersect the host rock of the hanging wall. In the contact zone between the black shales and the massive sulphides, there is structural concordance with a tendency to develop a banded texture. The fissure network is denser towards the top of the acidic tuffs and black shales of the hanging wall, diminishing towards the base of the volcanic pile. The presence of cassiterite in the fissure-type mineralization always occurs below chalcopyrite, which develops at the top, adhering to Neves-Corvo's vertical zonation (Moura, 2008).

In the table 2.1 there is an overview of the different types of mineralization found in the Neves-Corvo mining complex.

Table 2.1 – Table of the different types of ores present in the Neves-Corvo Mine. (Somincor, 2023)

Ore or waste rock	Mineralization	Code
Zinc ore	Massive zinc and lead sulphide	MZP
	Stockwork zinc	FZ
	Massive zinc	MZ
Copper	Massive copper and zinc sulphide	MCZ
	Massive copper	MC
	Stockwork copper	FC
Tin	Stockwork tin	FT
	Massive tin	MT
Waste	Massive waste	FE
	Stockwork waste	ME

2.3 Extraction and Concentration Methods

In the subchapter on Extraction and Concentration Methods, the techniques and processes involved in extracting valuable minerals in geological deposits and subsequently separating them from ore are delved.

2.3.1 Extraction

2.3.1.1 Open-pit mining

Open-pit mining is a prominent surface mining technique used to extract economically valuable minerals or ores near the Earth's surface. This method involves removing of overlying geological strata, including rock, soil, and ancillary materials, to access and retrieve the targeted mineral resources such as coal, copper, gold, and iron.

Characterized by a distinctive pit geometry, open-pit mines consist of horizontal stratifications known as "benches." The thickness of these benches is contingent upon various factors such as the specific deposit type, the mineral being extracted, and the equipment utilized. In sizeable mining operations, these benches may reach dimensions of approximately 12 to 15 meters. Mining activities generally transpire concurrently across multiple benches. Each individual bench serves as a distinct working level, and accessibility to different levels is achieved through a network of ramp structures. The width of these ramps is contingent upon the machinery used, generally spanning between 20 to 40 meters. The commencement of mining on a novel level is initiated through the gradual extension of a descending ramp. This initial cut, referred to as the "drop cut," is subsequently expanded to constitute the nascent pit bottom.

The determination of pit wall angles involves a compendium of factors, such as the cohesive properties of the rock mass, geological substrates, and safety considerations. The significance of the integrity and stability of these walls, individual benches, and groups of benches cannot be overstated, especially with the increasing depth of the pit. Even a minor adjustment in the pit slope angle can significantly impact stripping costs and ore recovery rates. Therefore, the implementation of ongoing slope-stability programs is considered imperative. These programs encompass the collection and analysis of structural data, hydrogeologic insights, and operational practices, with a particular focus on blasting methodologies. In larger open-pit mining facilities, the utilization of multiple slope angles may be necessary.

As the pit deepens, an increasing amount of waste rock must be removed to expose the desired ore. There comes a point where the costs associated with removing waste exceed the revenues generated from ore extraction. At this juncture, mining operations are usually discontinued. The "overall stripping ratio" is the ratio of waste rock extraction to ore recovery. The "break-even stripping ratio" is based on economic factors, including the ore value and operational expenses.

The inaugural phase of open-pit mining engenders the determination of ore reserves. This exigent task entails the perforation of probe holes to garner intelligence about the deposit's extent, configuration, and intrinsic attributes. The locations of these boreholes are cartographically plotted, and vertical cross-sections extracted from the boreholes furnish insights into the ore body's vertical expanse. Typically, ore reserves are calculated in terms of horizontal sections, with the thickness of each section corresponding to the height of a bench. These sections are subdivided into blocks along coordinate lines, with each block evaluated for its ore grade. Economic variables are subsequently superimposed, culminating in the formulation of an economic block model. The floating cone technique is a frequently employed stratagem for determining the configuration of the ultimate pit (Hustrulid, Britannica, 2023).

2.3.1.2 Underground Mining

Underground mining is a method employed to extract valuable minerals and ores from beneath the Earth's surface. This approach becomes necessary when ore bodies are located at significant depths, rendering surface mining impractical or uneconomical. Underground mining methods are traditionally categorized into three classes: unsupported, supported, and caving methods. These categories reflect the geomechanical competency of the ore body and the surrounding rock.

Drilling and Blasting: The underground mining process begins with drilling, which is done using various methods depending on the size of the opening and the rock type. After drilling, explosives are used to break the rock and create space for access and extraction. This crucial step prepares the underground environment for subsequent mining activities.

Loading and Hauling: Following the blasting, mining equipment, such as haul trucks or conveyors, is employed to load the fragmented rock and transport it to the surface for processing. Loading and hauling are fundamental for the safe and efficient movement of materials within the mine.

Scaling and Reinforcing: To ensure the safety of underground spaces, scaling and reinforcing are carried out. Scaling involves removing loose rock from the walls and roof of the mine to prevent accidents, while reinforcing includes measures like installing support systems such as roof bolts and mesh to enhance stability.

Room and Pillar Mining: This prevalent method in underground mining involves creating rooms by extracting ore, leaving pillars of unmined material to support the roof. It is suitable for relatively shallow ore bodies with strong surrounding rock.

Narrow Vein Stopping: In cases where ore bodies are confined to narrow veins, narrow vein stopping is employed. This method involves creating tunnels along the veins and systematically extracting the ore.

Large-Scale Mechanized Mining: For extensive and deep ore bodies, large-scale mechanized mining is adopted. This method utilises heavy machinery and advanced technology to extract minerals efficiently (Hustrulid, 2023)

2.3.2 Concentration Methods

Concentration methods in mineral processing unequivocally serve as the linchpin of the extraction process, holding paramount importance in the pursuit for economic viability. The fundamental rationale behind this centrality lies in their ability to enhance the overall mineral product's grade, thereby streamlining the extraction of precious minerals. By concentrating high-value minerals, these methods effectively reduce mining, transportation, and processing expenditures, ultimately optimizing the returns on investment. Moreover, the scope of concentration processes extends to the recovery and recycling of valuable minerals from secondary sources, aligning with the principles of the circular economy and sustainability. Significantly, these processes concurrently reduce waste volume, thus mitigating the environmental impact of waste disposal. In summary, concentration methods represent a pivotal and multifaceted stage, indispensable in ensuring the cost-effectiveness, environmental responsibility, and resource efficiency of mineral extraction endeavours (Hustrulid, 2023).

2.3.2.1 Overview

Concentration techniques are fundamental processes in mineral processing, aiming to separate valuable minerals from waste rock, thereby improving their grade and economic viability. Several key concentration techniques are commonly employed:

- **Jigging:** Jigging is a gravity-based separation technique that relies on the oscillatory motion of water within a jigging apparatus. This motion leads to the stratification of particles based on their respective densities. In this process, denser minerals precipitate more rapidly, while lighter gangue constituents are entrained and displaced. Various jig designs, encompassing diaphragm jigs and centrifugal jigs, are employed in this technique.
- **Flotation:** Froth flotation represents a specialized sub-technique within flotation that excels in the separation of a diverse array of minerals. It depends on the adhesion of hydrophobic particles to air bubbles. Flotation, a widely employed method, capitalizes on different surface properties of minerals to effect separation. In this process, minerals are differentially affixed to air bubbles and transported to the liquid-gas interface, generating a froth, while gangue materials remain suspended in the aqueous pulp. Froth flotation exhibits pronounced effectiveness, particularly in the processing of sulphide ores.
- **Gravity Separation:** Gravity separation methodologies, exemplified by devices like spiral concentrators, shaking tables, and centrifugal concentrators, harness distinctions in particle densities. This strategy capitalizes on the disparity in gravitational response times, causing heavier minerals to settle more expediently, thus facilitating efficient separation.
- **Magnetic Separation:** This technique utilizes magnets to selectively attract and segregate minerals with diverse magnetic susceptibilities from their non-magnetic gangue counterparts.
- **Dense Media Separation (DMS):** DMS is an approach that relies on a high-density medium, frequently a suspension comprising ferrosilicon or magnetite, for the separation of minerals

predicated on their density. Minerals with higher density precipitate while less dense materials are buoyant.

- **Leaching:** This method involves the dissolution of valuable minerals from ores using chemical solutions, and it is particularly applicable to minerals like gold and uranium.
- **Electrostatic Separation:** This method exploits variations in electrical conductivity and charge to segregate minerals, effectively distinguishing between conductive and non-conductive mineral species.

Each concentration technique presents specific applications and advantages, and the selection of a method depends on the characteristics of the mineral and the specific objectives within the realm of mineral processing (Hustrulid, 2023); (Silva, 2019).

2.3.2.2 Gravity Separation

Gravity-based techniques utilize differences in mineral density for concentration purposes. In heavy-media separation, a finely ground heavy mineral or a technical product like magnetite or ferrosilicon is suspended in water, creating a medium with a density higher than water. When crushed ores are introduced into this suspension, gangue constituents, characterized by lower density, tend to float and are extracted as tailings, while valuable mineral particles, with their higher density, gravitate and are separated. The magnetite or ferrosilicon content in the tailings can be recovered through magnetic separation for recycling.

Jigging involves applying pulsating motion to a water stream, achieved by upward and downward motion via pistons through the material bed. This oscillatory influence stratifies the bed into layers of varying densities, with the densest material forming the lowest layer and the least dense product occupying the highest. Effective jigging requires meticulous classification of the feed, as particles measuring less than one millimetre cannot be effectively isolated through this method.

Finer particles, ranging from 1 millimetre to 50 micrometres, can be efficiently segregated within a flowing water stream, either on horizontal or inclined planes. Additional forces come into play in many systems, such as the centrifugal force acting on spirals or the impact forces inherent in shaking tables. Spirals, with a vertical channel of oval cross-section, enable heavier particles to concentrate on the inner side of the stream as the pulp traverses from the top to the bottom of the channel, allowing their removal through specialized openings.

Inclined planes are used for gravity concentration through shaking tables. These tables may be smooth or grooved and experience reciprocal lateral vibrations perpendicular to the water flow. As the pulp descends along the incline, it undergoes stratification, resulting in the separation of heavy and light layers in the water. Furthermore, the vibrations contribute to particle separation in the direction of impact (Hustrulid, 2023); (Silva, 2019).

2.3.2.3 Froth Flotation

Froth flotation stands as the predominant technique for concentrating finely granulated minerals, taking advantage of differences in the physicochemical surface properties of minerals, especially their wettability. This property can be inherent or artificially modified through chemical reagents. By manipulating mineral particle surfaces to be either hydrophobic (exhibiting water-repellent characteristics) or hydrophilic (demonstrating water-attracting tendencies), the capacity is created to induce mineral adhesion to air bubbles traversing a flotation cell or to retain them within the pulp. Air bubbles rise to the upper pulp surface, forming a froth that incorporates the attached hydrophobic minerals, enabling their removal. Conversely, the hydrophilic minerals, located within the tailings, are extracted from the lower section of the cell.

Flotation techniques are particularly effective in processing complex, intermingled ores containing constituents such as copper, lead, zinc, and pyrite. These techniques allow the separation of such ores into distinct concentrates and tailings, an achievement that would be unattainable through gravity-based, magnetic, or electrostatic separation methodologies (Hustrulid, 2023); (Silva, 2019)

2.3.2.4 Magnetic Separation

Magnetic separation hinges upon the divergence in magnetic susceptibility exhibited by various minerals when subjected to the influence of magnetic fields. Effective magnetic separation mandates that the dimensions of the feed particles conform to a specific size range, typically ranging from 0.1 to 1 millimetre. In cases where favourable outcomes are observed, minerals with strong magnetic properties, such as magnetite, franklinite, and pyrrhotite can be effectively separated from accompanying gangue minerals using low-intensity magnetic separators. Alternatively, high-intensity magnetic devices are capable of separating oxide iron ores, including limonite and siderite, as well as iron-bearing manganese, titanium, tungsten ores, and iron-bearing silicates (Hustrulid, 2023); (Silva, 2019).

2.3.2.5 Electrostatic Separation

The electrostatic separation method serves to discriminate particles based on disparities in their electrical charges and, where feasible, differences in size. When particles exhibiting distinct polarity are subjected to an electrical field, they traverse distinct trajectories and can be isolated individually. This electrostatic separation technique finds application in all facilities engaged in the processing of heavy mineral sands containing minerals such as zircon, rutile, and monazite. Furthermore, electrostatic methodologies are integral to the purification of specific iron ore and cassiterite concentrates, along with the separation of cassiterite-scheelite ores (Hustrulid, 2023); (Silva, 2019).

2.4 Processing Plants

The Neves Corvo mine houses a mineral processing plant crucial for the extraction and refinement of copper and zinc ores. This facility serves as a pivotal element in transforming raw ore into valuable metal concentrates. In this discussion, we will provide an overview of the Neves Corvo processing plant, highlighting its key processing steps and their significance in the overall ore beneficiation process. This analysis seeks to provide insights into the essential functions of the plant, fostering a fundamental comprehension of its role in the effective extraction and refinement of mineral resources (Somincor, 2023).

2.4.1 Copper Plant

The Copper Plant at Neves Corvo operates at a substantial capacity of 2.8 million metric tons annually, playing a crucial role in processing various copper ore types, including Massive Copper (MC), Massive Copper-Zinc (MCZ), Copper Stockwork (FC), and Massive Copper with elevated penalty elements (MH). Each ore type presents distinct processing characteristics; for example, FC stockwork ores are physically hard with coarser grains, while MC, MH, and MCZ ores are fine-grained. Despite these differences, the processing plant adeptly manages this ore blend, encompassing operations such as pre-screening, crushing, grinding, flotation, filtration, concentrate storage, and dispatch, while handling utilities and tailings (Somincor, 2023). The flowsheet of the Copper Plant is showed in the Figure 2.3 bellow.

The coarse ore from the mine is transported to surface stockpiles using a conveyor and mobile stacker system. These stockpiles serve as the initial source for ore reclamation, with ore either directed to a pre-screening section or crushers via variable plate feeders. A pre-screening unit is positioned before the crushers to remove fines (<19mm) from the run-of-mine ore, particularly beneficial for high-moisture-content ore.

The output from the pre-screening process is carefully managed, with undersized material directed to a fine ore storage silo, providing flexibility for supplying grinding lines. An alternative method involves loader reclamation via a chute to the silo to feed the second grinding line. Screen oversize, including reclaimed materials, is reintroduced to the crushing circuit for further processing.

Operational efficiency takes precedence, with peak throughput achieved during off-peak hours to optimize energy costs and maintenance. This scheduling ensures a consistent feed supply for downstream operations. A capacious silo with extensive rod mill feed storage complements the ore handling system.

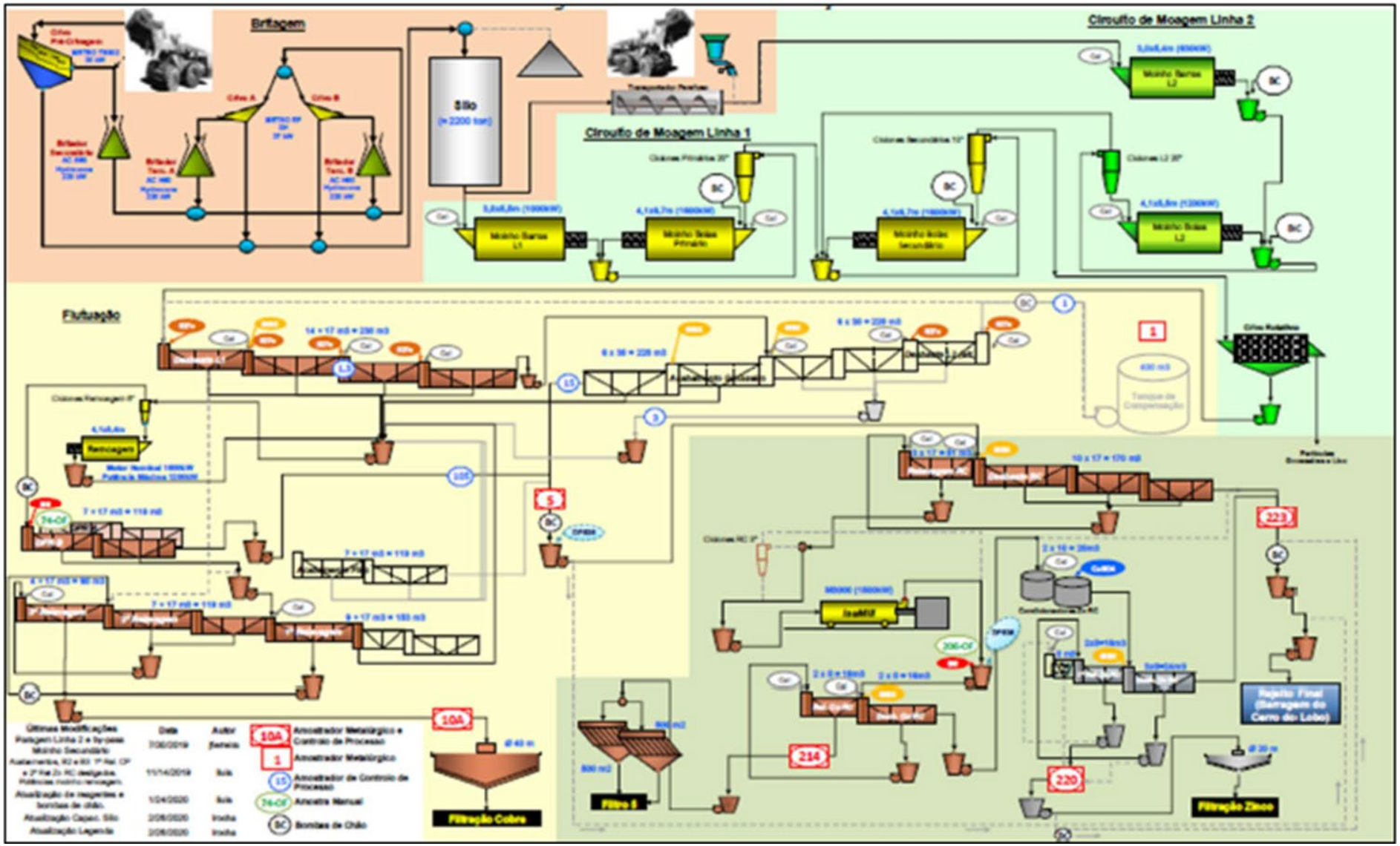

Figure 2.3 – Flowsheet of the copper plant (Somincor, 2023)

2.4.1.1 Grinding and regrinding

The Neves Corvo mining operation is equipped with two main grinding lines: Line 1 and Line 2. Line 1 consists of an open-circuit rod mill and a closed-circuit primary ball mill with hydrocyclones. Line 2 is fed from the fine ore stockpile via a screw feeder or front-end loader and includes an open-circuit rod mill and a closed-circuit primary ball mill with hydrocyclones. Both primary ball mills discharge into a shared secondary ball mill, which, in turn, delivers the feed to Sala cyclones. The overflow from the secondary cyclones is directed to the flotation circuit through a rotating trash screen.

Neves Corvo aims for milling rates of 260 tph for Line 1 and 80 tph for Line 2. A copper regrind mill operates in a closed circuit, receiving feed from a series of cyclones, which is essential for achieving the desired particle size distribution with a d_{80} between 18-25µm. The utilization of hydrocyclones in closed circuits and precise control of particle size distribution in the grinding circuit play a crucial role in efficiently preparing the ore for subsequent flotation processes.

2.4.1.2 Copper Flotation

The flotation circuit at the Neves Corvo mining operation plays a crucial role in their mineral extraction process, emphasizing efficient ore separation. It comprises two rougher section configurations: one with 14 cells of 17m³ capacity and another with 12 cells of 38m³. Lime is utilized for pH control, and copper collectors (D527e and sodium isobutyl xanthate - SIBX) aid in copper recovery. The rougher cells generate a concentrate that undergoes cycloning, with the cyclone underflow directed to a regrind ball mill.

After regrinding, the concentrate advances to the DPR (rougher regrind) cells, consisting of 7 x 17m³ cells. Sodium metabisulphite is introduced to depress sphalerite and pyrite before the DPR concentrate undergoes a comprehensive cleaning process. Cleaning involves three stages with different cell configurations: banks of 9, 7, and 4 cells, each with a capacity of 17m³. There is an option for a fine scavenger stage. The focus is on optimizing the cleaning circuit to better align with current requirements. This includes resizing specific flotation banks to match available cell volumes and reduced flowrates, enhancing circuit responsiveness, and reducing power and maintenance demands.

2.4.1.3 Tailings Retreatment (RC) Circuit

The Neves Corvo plant features an RC (Regrind-Cleaner) circuit designed to recover copper and zinc from Copper Plant tailings. This circuit comprises rougher and cleaner stages, making use of 13 flotation cells, each with a capacity of 17m³. The produced concentrate undergoes specialized grinding to attain a particle size of less than 12µm. Following regrinding, conditioning agents are introduced to depress zinc ore and enhance copper flotation in 8m³ cells, resulting in a 3% increase in copper recovery.

2.4.1.4 Filtration

The final copper concentrate undergoes a thickening process in a large-diameter thickener, achieving a solids content ranging from 65% to 68%. After concentration, it is transferred to a storage tank within the filter plant, allowing pumping to a set of high-capacity pressure filters. A subset of these filters is in operation, while one is reserved for maintenance purposes.

2.4.1.5 Plant Performance

The Copper Plant at the Neves Corvo mining operation reached its peak treatment rate of 2.7 million metric tons per annum (Mtpa) in 2018. However, recent years have witnessed a decline in copper recoveries, attributed to factors such as increased processing of challenging MH ore types, lower head grades, and deteriorating process water quality from paste tailing thickeners. Although copper concentrate grades have generally remained stable, a slight decrease has been observed recently, with an average grade of 22.7% Cu in 2021. Contaminant levels in the concentrate, including arsenic (As), antimony (Sb), and lead (Pb), have increased due to the processing of more complex MH ore types. The plant's head grade has declined from 2.55% Cu to 1.76% Cu over the past six years, posing ongoing operational challenges (Somincor, 2023).

2.4.2 Zinc Plant

The expansion project of the Zinc Plant (ZEP) at the Neves Corvo mining operation was initiated in 2018. This project involved the integration of existing process equipment, from the 1.15 million metric tons per annum (Mtpa) capacity Zinc Plant alongside new equipment to raise the plant's capacity to 2.5 Mtpa. Due to covid-19, the construction process faced challenges, delays, and cost pressures, to be precise. The challenges prompted reviews aimed at reducing costs and simplifying the expansion plan. So, the implementation of the lead circuit was deferred during the production ramp-up phase, affecting the current treatment capacity and recoveries for both lead and zinc. The revised lead cleaning circuit is slated for full implementation by August 2024. Despite these setbacks, there are optimistic expectations for the ZEP's planned throughput to increase from 1.7Mt in 2022 to 2.5Mt in 2024.

The current flowsheet for the Zinc Plant, wherein only 50% of the lead is treated, is illustrated in Figure 2.4 below.

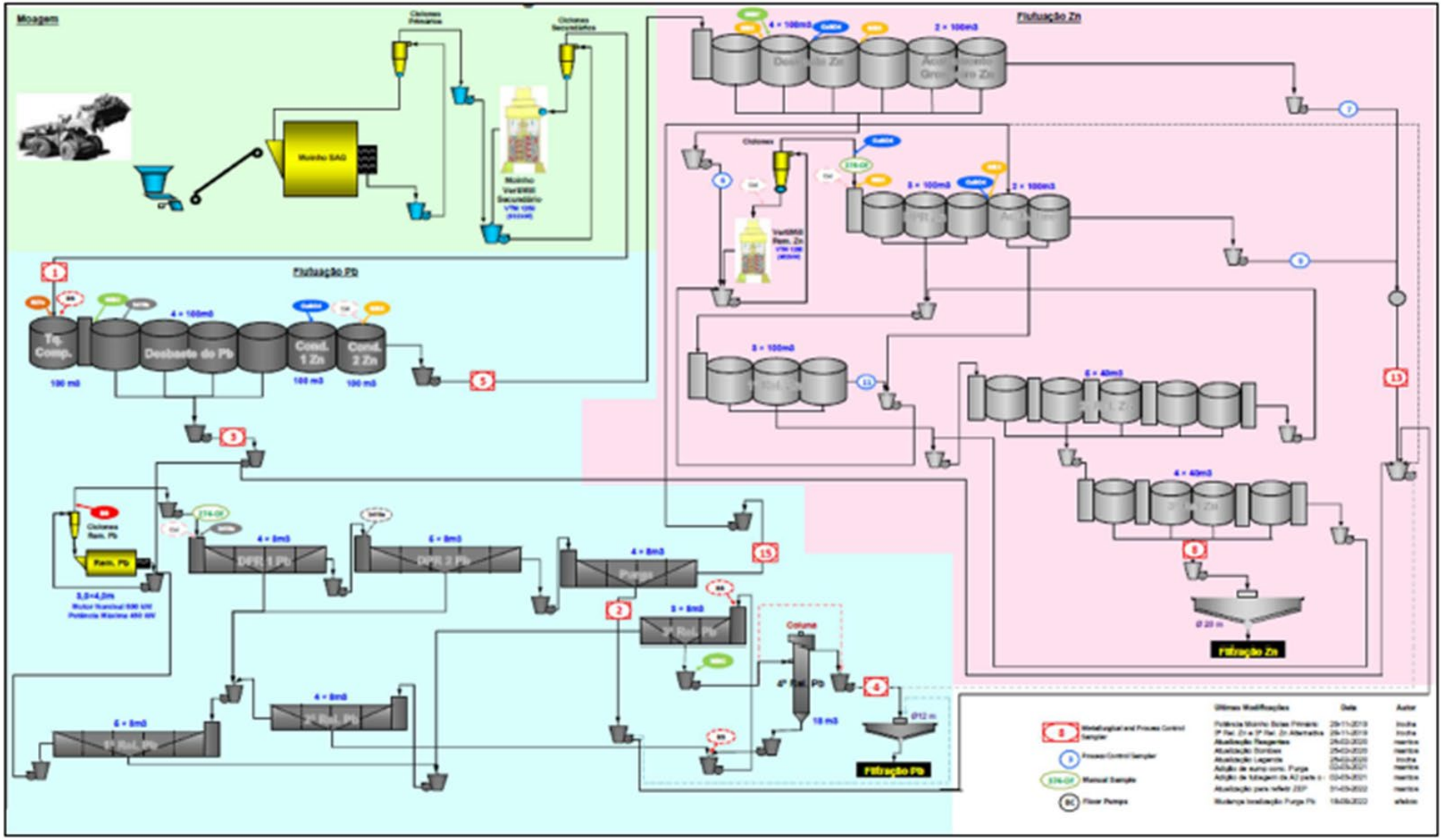

Figure 2.4 – Zinc and Lead production flowsheet (Somincor, 2023)

2.4.2.1 New Grinding and Flotation Buildings

In the new Flotation Building at Neves Corvo Mine, a configuration of two parallel rows, each consisting of 6 x 100m³ tank cells, has been implemented. Specifically, one row is dedicated to lead (Pb) roughers and scavengers, while the other serves zinc (Zn) roughers and scavengers. These cells are strategically positioned on a sloping concrete floor, leveraging the natural terrain to create a total height difference of 5.5 meters. This innovative design not only optimizes the utilization of the landscape but also contributes to cost-effective construction practices. Furthermore, concentrate and tailings pump boxes, along with their associated pumps, are situated at the eastern end of the building, positioned approximately 2 meters below the final flotation cells in each row.

2.4.2.2 Copper-Lead Bulk Flotation

The Neves Corvo plant adopts a copper-lead bulk flotation process, primarily due to the low copper levels in the zinc ore. Operating in a "50% Pb Production" mode, half of the lead rougher concentrate undergoes flotation, while the remaining half is directed to final tailings. The copper-lead rougher flotation is carried out in four large cells, with a portion of the rougher concentrate undergoing regrounding. Challenges arise from the elevated sulphosal content in the ore, effectively serving as an aeration stage.

The reground concentrate undergoes four stages of conventional cleaning, with the first stage referred to as the DPR stage and employing nine cells. Lead DPR tailings undergo processing in scavenger cells before reaching the final tailings. The DPR scavenger tailings then proceed to the zinc DPR stage. The DPR concentrate undergoes three additional cleaning stages, utilizing both conventional cells and a flotation column to ensure the desired concentrate quality. A key requirement is that the combined copper (Cu%) and lead (Pb%) content exceeds 31%, meeting the targeted grade.

2.4.2.3 Concentrate Thickening and Filtering

The zinc plant expansion anticipates an upsurge in lead concentrate production. To facilitate this, a 12-meter diameter high-rate thickener has been strategically positioned south of the lead concentrate loadout building. To accommodate the higher production capacity, a new lead filter with 36 plates has been introduced alongside the existing 12-plate filter.

The final copper-lead concentrate undergoes loading into 20-foot shipping containers, which are hermetically sealed to prevent oxidation during transportation. On the other hand, the final zinc concentrate undergoes thickening in a 20-meter diameter high-rate thickener. Following thickening, the concentrate is pumped to a storage tank and subsequently subjected to filtration through three filter presses. The resulting material is then transported to a covered zinc concentrate storage building. Within the plant, an efficient water recycling system combines water recovered from concentrate thickening with water from the filtration process.

2.4.2.4 Plant Performance

From 2017 to 2021, lead concentrate grades at Neves Corvo varied between 4.05% and 5.87% for copper (Cu) and 23.07% to 28.8% for lead (Pb). However, copper and lead recoveries remained consistently low during this period, with average values of 22.6% for Cu and 27.6% for Pb until 2021. In Q1 2022, during the initial ramp-up phase of the Zinc Expansion Project (ZEP), there was a further decline in copper and lead recoveries, reaching 6.0% and 15.4%, respectively. These reduced recoveries were attributed to limitations within the 50% lead circuit.

Conversely, zinc concentrate grades from 2017 to 2021 exhibited a narrower range, fluctuating between 45.6% and 47.2% for zinc (Zn). Zinc recoveries over this period showed a range of 76.2% to 80.7%. However, during the early phase of the ZEP ramp-up in Q1 2022, zinc recovery averaged 67.4%, indicating the transitional nature of the expansion. Silver recoveries between 2017 and 2021 averaged 14.1% for the lead concentrate and 26.4% for the zinc concentrate (Somincor, 2023).

3 METHODS AND THEORY

In this chapter, the theoretical foundations and methodology that constitute the backbone of this study are described, encompassing sample preparation and image acquisition through SEM/MEV, as well as data processing and geostatistical modelling techniques. In this context, the theoretical foundations of the Scanning Electron Microscope (SEM) are outlined, which was the crucial instrument for image acquisition in this study. As the 3D reconstruction methodology is grounded in geostatistical simulation, the theoretical fundamentals of geo-statistics are subsequently presented, such as variography, kriging estimation, and sequential indicator simulation.

3.1 Scanning Electron Microscopy – Energy Dispersive Spectroscopy (SEM-EDS)

Scanning Electron Microscopy (SEM) is a high-resolution imaging device that utilizes electron beams to capture detailed images of object surfaces. Its applications span various fields, including geology and materials engineering, allowing for nanoscale surface and structural analysis.

3.1.1 Theorical Principles

SEM is grounded in quantum physics, specifically the tunnel effect, where electrons can penetrate potential barriers despite lacking the necessary energy. This principle forms the basis for SEM's capability to explore the characteristics of object surfaces. SEM comprises three essential components: an electron source, a lens system, and an electron detector. The electron source generates the beam used for illuminating the sample, the lens system controls electron paths, and the detector captures and transforms scattered electrons into images.

Energy-Dispersive X-ray Spectroscopy (EDS) is a highly sophisticated analytical technique used for precisely determining the elemental composition of materials. Primarily operating within electron microscopes, EDS begins when a concentrated beam of high-energy electrons interacts with the specimen, leading to inner-shell electron excitation and the generation of characteristic X-rays. These X-rays, each uniquely associated with a specific element, are detected by an X-ray detector, allowing for their characterization based on energy. The theoretical foundation of EDS culminates in the creation

of an X-ray spectrum, visually representing the distribution of X-ray energies and facilitating the identification of elements. This fundamental process, combining energy analysis and spectral data, plays a crucial role in EDS' invaluable contribution to materials analysis and scientific research.

3.1.2 SEM Imaging Techniques

Secondary Electron Imaging is a microscopy technique that involves measuring secondary electrons generated when an electron beam interacts with a sample. These secondary electrons are emitted from the sample's surface due to the interaction with the incident electron beam. The intensity of these secondary electrons is directly related to the topography of the sample's surface, making it possible to produce high-resolution surface images (Davuluri, 2018).

On the other hand, Backscattered Electron Imaging is an electron microscopy technique that measures electrons backscattered when an electron beam interacts with a sample. These backscattered electrons are emitted from the sample's surface and interior due to the interaction with the incident electron beam. The intensity of backscattered electrons correlates with the density of the sample's matter. Consequently, this technique provides valuable information about the internal structure and composition of the sample, revealing variations in material density, elemental composition, and crystallography within a specimen (Davuluri, 2015).

3.1.3 Working Principles of SEM-EDS

The tunnelling effect, a fundamental phenomenon in quantum mechanics, plays a crucial role in electron-sample interactions. When the electron beam is directed towards the sample surface, it encounters electrical barriers created by atomic or molecular structures on the sample surface. In classical physics, these incident electrons would be repelled by the positive charges in the nucleus of the sample, preventing penetration of the surface.

However, the peculiar behaviour of tunnelling, owing to its quantum nature, defies classical expectations. Even in the presence of energy barriers, some incident electrons exhibit the phenomenon of tunnelling, being deflected upwards and entering the sample. This behaviour highlights the unique quantum mechanical aspect where particles can penetrate potential barriers, contrary to classical predictions.

This tunnelling phenomenon has important implications in the SEM, leading to two significant outcomes. First, as some of the incident electrons pass through the surface barrier, they lose energy and are captured by the sample atoms. This capture process results in the emission of secondary electrons from the sample surface. These secondary electrons carry valuable information about geomorphology and surface properties. In SEM imaging, they are essential for high-resolution image formation, as their intensity reflects changes in surface height and composition.

Other incident electrons that undergo tunnelling may not lose enough energy to be captured within the sample. Instead, they are scattered backward (backscattered) due to interactions with the sample's

nuclei. These backscattered electrons tend to be higher in energy and provide compositional information about the sample. The intensity of backscattered electrons correlates with the density of atomic nuclei in the sample. Therefore, materials with heavier elements or greater atomic density scatter electrons more effectively, resulting in stronger backscattered signals.

EDS operates on the fundamental principles of X-ray emission and spectral analysis. When a high-energy electron beam is directed onto a sample within an electron microscope, such as a Scanning Electron Microscope (SEM) or Transmission Electron Microscope (TEM), interactions between the beam and the electrons residing within the atoms of the specimen occur.

These interactions lead to the excitation or displacement of inner-shell electrons. Upon their eventual return to their original positions, the inner-shell electrons release energy in the form of X-rays. Critically, these emitted X-rays exhibit energies that are inherently tied to the specific atomic structure of the elements within the sample. The unique energy signature of each element allows for its differentiation in the subsequent analysis.

The X-rays emitted by the sample are collected by an X-ray detector placed in proximity to the specimen. Within the detector, these X-rays are sorted and categorized based on their distinct energies. It is crucial to recognize that each element has its own characteristic X-ray energy spectrum. Therefore, the detection and analysis of the energy distribution of these emitted X-rays serve as the foundation for both element identification and quantification.

The culmination of this process leads to the generation of an X-ray spectrum, effectively encapsulating the diversity of X-ray energies emitted by the sample. By scrutinizing this spectrum, researchers and analysts can pinpoint the elemental composition of the specimen and gauge the relative concentrations of its constituent elements. Furthermore, EDS is equipped to provide quantitative data through the comparison of X-ray intensities with established standards, allowing for the precise determination of element percentages (Swapp, 2023).

3.2 Geostatistics

Geostatistics is an applied discipline that specifically deals with the statistical analysis of georeferenced data. To this end, it incorporates traditional statistical concepts with spatial considerations to model the variability and spatial correlation of these variables. The main objective of geostatistics is to make inferences in unsampled locations based on the available observations.

Geostatistics was initially used in the mining industry but is now widely applied in various areas of science and engineering. For example:

Extractive Industry: It uses geostatistics in various aspects of a mining project. Initially, to quantify mineral resources and assess the economic feasibility of the project. Later, in day-to-day operations, it is used to decide which materials are directed to the plant and which are considered waste, using updated information as it becomes available.

Environmental Sciences and Engineering: Geostatistics is used to estimate pollutant levels and decide if they pose a threat to environmental or human health, justifying the need for remediation (Kanevski, et al., 2004).

Precision Agriculture: Mapping soil nutrient levels (nitrogen, phosphorus, potassium, etc.) and other indicators (such as electrical conductivity) to study their relationships with crop yield and prescribe precise amounts of fertilizers for each location in the field.

Meteorological Applications: Prediction of temperatures, rainfall, and associated variables (such as acid rain) (Kanevski, et al., 2004).

Public Health: More recently, there have been several applications of geostatistics in public health, such as predicting environmental contaminant levels and their relation to cancer incidence rates (Diggle & Giorgi, 2019).

In all these examples, the common context is that variables occur in space or space-time (the level of soil, water, or air contamination by a pollutant; the content of gold or some other metal in a mine, etc.). It is important to note that studies with exhaustive sampling are expensive and time-consuming, so geostatistics attempts to make predictions for unsampled locations with a more limited number of samples and in an optimization perspective of estimation error, also indicating the uncertainty of predictions.

3.2.1 Fundamentals of Geostatistics

Geostatistics encompasses several fundamental concepts crucial for understanding and analysing spatial data. One central concept is the variogram, also known as the semivariogram (Chu & Journel, 1994). The variogram plays a pivotal role in geostatistics by quantifying the spatial variability within a dataset. It achieves this by calculating the variance or semivariance between pairs of data points at different distances from each other. Examining the shape and range of the variogram provides valuable insights into the spatial correlation structure of the data (Olea, 1994).

Spatial autocorrelation is another critical concept in geostatistics, measuring the degree of similarity between values at different geographical locations. Positive spatial autocorrelation suggests that similar values tend to be close to each other in space, indicating a pattern of spatial clustering. Conversely, negative spatial autocorrelation indicates dissimilarity between neighbouring values, suggesting a pattern of spatial dispersion.

Kriging, a geostatistical interpolation technique, is essential in geostatistics. It estimates values at unsampled locations by considering spatial correlation and variogram information. Kriging provides more accurate predictions compared to traditional interpolation methods because it incorporates both nearby data values and the underlying spatial correlation structure (Srivastava, 1994).

Spatial dependence is another fundamental concept in geostatistics, acknowledging that data at one location are not independent of data at neighbouring locations. Instead, nearby values tend to influence each other, reflecting the idea that geographical proximity matters in spatial data analysis (Srivastava, 1994).

Not less important, anisotropy is the directional dependence of spatial correlation. In certain cases, the strength and nature of correlation between data points may vary based on the direction of separation. This phenomenon is crucial to consider when modelling spatial data, recognizing that spatial relationships may not be uniform in all directions (Goovaerts, 2006).

3.2.2 Variograms

In geostatistical analysis, variograms play a crucial role in quantifying spatial variability and spatial dependence within datasets. Variograms offer insights into the correlation structure of geospatial data and are instrumental in various applications, including environmental modelling, resource estimation, and risk assessment.

There are several geostatistical tools for measuring the spatial continuity of characteristics in a natural resource or natural phenomenon. The most favored element for assessing spatial continuity is the pair of points (separated by h), which allows evaluating the variation of spatial continuity in different directions (Almeida, 2018); (Goovaerts, 2006).

Taking a given quantitative characteristic of (x), diagrams representing pairs of points $Z(x)$ vs $Z(x+h)$, calculated based on the pair of points for different values of h, constitute statistics that contain more elaborate information about the spatial continuity of $Z(x)$. The representation of such diagrams results in scatter plots, where the more scattered they are, the lower the correlation between the samples. However, it is necessary to synthesize these scatter plots to improve their interpretation and enable the visualization of the evolution to which they are subjected with h (Soares, 2006).

If the mean of the squared differences between (x) and $Z(x\ +\ h)$ is applied to each scatter plot, the spatial continuity of $Z(x)$ can be determined by the variogram estimator for different values of h:

$$\gamma(h) = \frac{1}{2N(h)} \sum_{\alpha=1}^{N(h)} [Z(x_\alpha) - Z(x_\alpha + h)]^2$$

Equation 3.1 – Experimental Variograms Calculation

where (h) is the number of pairs of points for each h value.

Experimental variograms can be calculated for various directions in space, allowing for the characterization of the variation of the attribute $Z(x)$ in space.

Once the values of the variograms for different directions are calculated based on a set of samples from an area A, it is necessary to proceed with their modeling through a general and representative function. In other words, fitting the variograms through an attenuated mean curve, a function of a small number of parameters that quantify the spatial continuity of $Z(x)$. This adjustment of the experimental variogram by a theoretical model is conditioned by prior knowledge of the spatial phenomenon under study; in addition, the function used for interpolating the experimental points ensures that the variogram is positive.

As such, there is a limited number of functions that can be applied, providing a generalized coverage of spatial phenomena dispersion situations: spherical, exponential, and Gaussian models. In this work, only the first two were used.

All those theoretical models use two parameters, plus the nugget effect if exists:

- Sill C –The sill represents the maximum value that the variogram can attain, encapsulating the complete variability present in the dataset. It is observed when spatial correlation reaches its full development, beyond which increasing the lag distance no longer influences it.
- **Range (*h* = a)** – The range signifies the distance at which spatial correlation reaches its maximum extent, often referred to as the "sill." Essentially, it delineates how far apart data points must be situated before they lose their correlation.
- The **nugget effect C_0**, a crucial concept in geostatistics, appears as a discontinuity originating from the variogram's origin. This effect incorporates both measurement error and small-scale variability, emphasizing the importance of distinguishing between pure nugget effect (indicating no spatial correlation) and partial nugget effect (suggesting some spatial correlation, albeit limited to very short distances).

The spherical model has the following expression (Equation 3.2) (Oliver & Webster, 2014):

$$\gamma(h) = \begin{cases} C_0 + C\left[1{,}5\,\frac{h}{a} - 0{,}5\left(\frac{h}{a}\right)^3\right] & if\ h \le a \\ C_0 + C & if\ h > a \end{cases}$$

Equation 3.2 – Spherical Variogram Model Equation

Conversely, the exponential variogram model is applied when spatial correlation decreases exponentially with distance. It is expressed as (Equation 3.3):

$$\gamma(h) = C_0 + C\left[1 - e^{-3h/a}\right]$$

Equation 3.3 – Exponential Variogram Model Equation

In this model, the variogram asymptotically approaches the sill value $C_0 + C$ and the range a is the distance at which the model reaches 95% of the sill: $\gamma(h) = 0{,}95\mathrm{C}$.

Another variogram model is the gaussian, and is used to fit very continuous variables (Equation 3.4):

$$\gamma(h) = \begin{cases} 0, & h = 0 \\ C_0 + C_1(1 - e^{-\frac{h^2}{a^2}}, & x \ge 0 \end{cases}$$

Equation 3.4 – Gaussian Variogram Model Equation

Like the spherical and exponential models, it includes parameters such as sill (C0), nugget effect (C1), and range (a). (Supergeo, s.d.)

It's worth noting that the variogram is closely associated with the covariance function. The covariance function $C(h)$ serves as a complementary measure to the variogram, providing insights into the degree of association between data points across varying distances. The relationship between the variogram and the covariance function is articulated as $C(h) = C0 - \gamma(h)$, where $\gamma(h)$ represents the variogram. This relationship highlights the interplay between these two fundamental aspects in geostatistical analysis.

Now, having discussed the significance of variograms in analysing the spatial correlation of data, let's naturally progress to a powerful technique widely used for interpolating values at unsampled locations - Kriging. Kriging relies on the information derived from variograms to generate more accurate estimates, considering not only nearby values but also the underlying spatial correlation structure. We will explore how Kriging works and how it relates to variograms in our geostatistical analysis.

3.2.3 Simple Kriging and Ordinary Kriging

Kriging is a fundamental geostatistical interpolation technique used to estimate values at unsampled locations based on spatial correlation and variogram information. Two employed kriging methods are Simple Kriging and Ordinary Kriging, each with its specific characteristics and applications.

Simple Kriging assumes that the mean of the variable being estimated is known and constant throughout the study area. It is well-suited when dealing with data where the mean is accurately known or when the analysis aims to assess only spatial variability around that known mean. Simple Kriging does not estimate the mean but rather interpolates the variance around it. This method assumes that the estimation errors are normally distributed and stationary across the study area (Equation 3.4) (Williams, 1998).

$$Z*(x_0) = \left(\sum_{i=1}^{n} \lambda_i . [Z(x_i) - m]\right) + m = \sum_{i=1}^{n} \lambda_i . Z(x_i) + \left[1 - \sum_{i=1}^{n} \lambda_i\right] * m$$

Equation 3.5 – Simple kriging equation

Ordinary Kriging, on the other hand, relaxes the assumption of a constant mean and estimates both the spatial variability and the mean simultaneously. It is a more flexible method and is commonly used when the mean of the variable is not precisely known or when there may be slight spatial variations in the mean. Ordinary Kriging estimates not only the variance around the mean but also the mean itself, making it suitable for situations with more complex spatial patterns (Equation 3.5) (Williams, 1998) (Kobylińska, 2016) and (Almeida, 2018).

$$Z*(x_0) = \sum_{i=1}^{n} \lambda_i * Z(x_i)$$

Equation 3.6 – Ordinary kriging equation

3.2.4 Indicator Variables Formalism

3.2.4.1 Concept

The implementation of geostatistical models for binary or indicator variables allows obtaining the estimated probability of any point in the study area belonging to a region, based on sampling in the vicinity of that point. For this purpose, it is necessary to work with an indicator variable, obtained by assigning values of 1 and 0 to a variable $Z(x)$ under study based on a parameter, such as a specific type of mineralization. Samples corresponding to the desired type of mineralization will be classified as 1, while the others will be assigned a value of 0.

$$I(x_i) = \begin{cases} 1 \; se \; z(x_i) = m \\ 0 \; se \; z(x_i) \neq m \end{cases}$$

3.2.4.2 Sequential Indicator Simulation

Sequential Indicator Simulation (SIS) is a geostatistical technique used for simulating categorical or discrete variables. This method is applied in various fields, including geology, mining, hydrogeology, and environmental science, where the analysis and representation of spatial distribution through categorical variables are crucial. Importantly, it is employed to delineate and predict the presence or absence of geological or environmental features across a spatial domain.

The process of Sequential Indicator Simulation involves several key steps:

Data Preparation: It starts with collecting categorical data at specified locations within the study area. These data points represent distinct categories characterizing the variable of interest, such as the presence or absence of a specific mineral or other geological characteristics.

Indicator Variogram Modeling: Variogram or semi-variogram models are constructed based on the collected data. These models quantify the spatial correlation and variability inherent in the categorical variable. Variograms illustrate how the similarity between data values changes concerning both distance and direction, forming the foundation for the subsequent simulation process.

Simulation of Categorical Variable: The core of SIS lies in generating multiple realizations of the categorical variable across the spatial domain. The main goal is to create a spatial distribution that aligns with the observed data and the spatial correlation described by the variogram. This is accomplished through sequential simulation, where values are generated in succession. Typically, the process starts

from one end of the study area and systematically progresses throughout it randomly. SIS integrates Indicator Kriging to estimate the probability of the categorical variable belonging to a specific category at simulated locations, where no data has been collected. In essence, it provides a probability distribution associated with the categorical variable's values across the spatial domain.

The Sequential Simulation Indicator (SSI) of a variable $Z(x)$ is based on the standard procedure of sequential simulation, where conditional distribution functions are estimated using the indicator formalism (Almeida, 2018); (Goovaerts, 2006).

The principle of sequential simulation is relatively simple and relies on the application of the Bayes' relation in successive steps. Thus, the simulation is performed through several iterations equivalent to the number of grid nodes to be simulated, with increasing conditioning based on the information available at the previous points already simulated.

The Bayes' relation can be generalized to a set of variables:

$$\mathrm{F}(\mathrm{Z}_1, \mathrm{Z}_2, \mathrm{Z}_3, \dots \mathrm{Z}_\mathrm{N}) = \mathrm{F}(\mathrm{Z}_1)\, \mathrm{F}(\mathrm{Z}_2|\mathrm{Z}_1)\, \mathrm{F}(\mathrm{Z}_3|\mathrm{Z}_2, \mathrm{Z}_1) \dots \mathrm{F}(\mathrm{Z}_\mathrm{N}|\mathrm{Z}_1, \mathrm{Z}_2, \mathrm{Z}_3, \dots, \mathrm{Z}_{\mathrm{N}-1})$$

Consider the joint distribution law of N random variables and n initial experimental conditioning values $\mathrm{F}(\mathrm{N}) = (\mathrm{Z}_1, \mathrm{Z}_2, \mathrm{Z}_3, \dots \mathrm{Z}_\mathrm{N}|(n))$. The simulation process of $F(N)$ can be summarized in the following steps:

i) **Initialization (if conditional simulation)**: Initialize the random variables $\mathrm{Z}_1, \mathrm{Z}_2, \mathrm{Z}_3, \dots \mathrm{Z}_\mathrm{N}$ based on the available information and the initial experimental conditioning values (n).

ii) **Simulation of a z_1 value** involves considering the cumulative distribution function $F\,(\mathrm{Z}_1|(n))$. Once the location z_1 is simulated, this value is added to the conditioning dataset, for the subsequent simulation steps, and the conditioning data increases from n to $n + z_1$;

iii) **Simulation of another value z_2** from the conditional distribution $F\,(\mathrm{Z}_2|(n+1))$, considering the $(n+1)$ previous data values plus the simulated grid nodes. Update of the conditioning dataset to $(n+2) = (n+1) + Z_2$;

iv) **Repetition** of the sequential process until the simulation of all N variables (locations) is completed.

It is important to remark that the N dependent random variables $\mathrm{Z}_1, \mathrm{Z}_2, \mathrm{Z}_3, \dots \mathrm{Z}_\mathrm{N}$, can represent the same variable or parameter georeferenced in N grid nodes of the area to be simulated. If the n initial conditioning values corresponding to the experimental data are considered, then:

$$F(N) = (Z(x_1), Z(x_2), Z(x_3), \dots, Z(x_N)|(n)).$$

This sequential simulation method relies on the knowledge of the N conditional cumulative distribution functions:

$$Prob\{\, Z(x_1) < z \,\big|\, (n)\,\}$$

$$Prob\{\, Z(x_2) < z|(n+1)\}$$

$$Prob\{ Z(x_3) < z|(n+2)\}$$

…

$$Prob\{ Z(x_N) < z|(n+N-1)\}$$

The knowledge of these functions is crucial for the implementation of SIS. According to (Goovaerts, 2006) and (Langetepe, 2010), indicator kriging serves as a tool for estimating these functions. SIS ensures conditioning to the indicator variograms and histograms of the experimental data.

It is a common practice to generate multiple realizations or simulations to address the inherent uncertainty in the spatial distribution of the categorical variable. These multiple realizations offer a range of plausible scenarios that align with both the observed data and the spatial correlation model.

As we delve into the predictive capabilities of geostatistical techniques, such as Kriging and Sequential Simulation, it becomes evident that while these methods provide valuable insights into the spatial distribution of elements, a more in-depth examination of the mineralogical composition within the estimated areas is warranted. This transition from 2D SEM analysis to 3D geostatistical images represents a pivotal phase in our study, enabling us to discern the liberation status of these key elements within the host rock matrix and thus optimize the flotation process (Goovaerts, 2006); (Jinchi Chu, 1994).

3.3 Methodology

In this subchapter, the stages of the methodology applied in this study are described. This includes the selection and preparation of ore samples from the Neves Corvo Mine, the obtainment of 2D images from SEM-EDS that binaryly depict the presence or absence of metallic elements of interest such as copper, zinc, and lead (indicating the shape and size of the grains containing these metals), the 3D geo-statistical modelling simulation of grain morphology, and the statistical processing of simulation results. Figure 3.1 illustrates this sequence of stages in a flowchart.

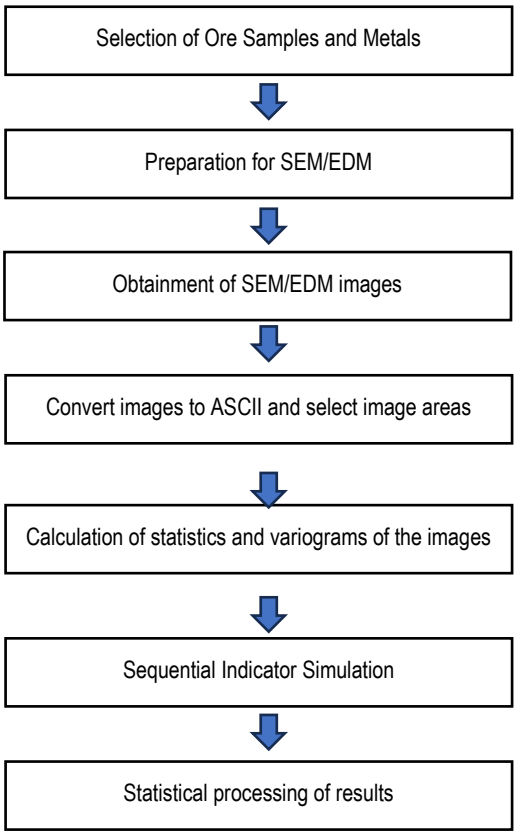

Figure 3.1 – Flowchart with the samples analysis stages

3.3.1 Selection of Ore Samples and Metals and Preparation to SEM/EDS

In the pursuit of a comprehensive analysis of the geological composition of the Neves-Corvo mine's ore at the scale of the grains, five distinct mineral samples were provided by Lundin Mining Company (owner of the Neves Corvo Mine) for study (Figure 3.2 to 3.6) (Table 3.1). These ore samples were selected based on the criterion of being significantly different from each other and serving as examples to conduct this pilot study.

Table 3.1 – List of the selected samples and identifications within this study

Samples designation	Identification
M_{Zn} (zinc ore)	Sample #1
M_{Cu} (copper ore)	Sample #2
M_{Cu} (copper ore)	Sample #3
F_{Cu} (stockwork copper ore)	Sample #4
F_{Cu} (stockwork copper ore)	Sample #5

Figure 3.2 – Sample #1

Figure 3.3 – Sample #2

Figure 3.4 – Sample #3

Figure 3.5 – Sample #4

Figure 3.6 – Sample #5

Following that, these ore samples with dimensions on the order of a few centimetres were cut with a rock saw into small cubes of approximately 1 cm^3, primarily with one flat face for SEM/EDS analysis. Images of these fragments can be viewed in the Figures 3.7 to 3.11.

	Figure 3.7 – Sample #1, prepared for SEM-EDS analysis.
	Figure 3.8 – Sample #2, prepared for SEM-EDS analysis.
	Figure 3.9 – Sample #3, prepared for SEM-EDS analysis.
	Figure 3.10 – Sample #4, prepared for SEM-EDS analysis.
	Figure 3.11 – Sample #5, prepared for SEM-EDS analysis

3.3.2 SEM analysis

Each of the five samples underwent a cutting process to achieve a final flat surface of approximately 0.6 cm on each side. This step aimed to improve the quality of the resulting maps while minimizing potential effects of oxidation or other non-representative reactions within the sample. Subsequently, a carbon coating was applied to enhance electrical conductivity and facilitate the reflection of incident electrons.

After manually defining and digitally recording the markers on the samples, the samples were placed on a Stage carousel for the scanning electron microscopy investigations. The microscope used was a Tescan, model VEGA LMU equipped with a high-voltage electron gun and two spectrometers, at GeoBioTec Research Unit, Geosciences Department from the University of Aveiro (Figure 3.12). The working distance was chosen and set at 15 mm and the electron beam voltage at 20 keV. Focus, contrast, and brightness were adjusted according to the desired image reproduction. Some of the SEM-EDS maps are possible to see in the figures 3.13 to 3.15 below.

Figure 3.12 – Representation of the equipment used to make the SEM-EDS Mapping, Tescan VEGA LMU, taken from (Tescan, s.d.)

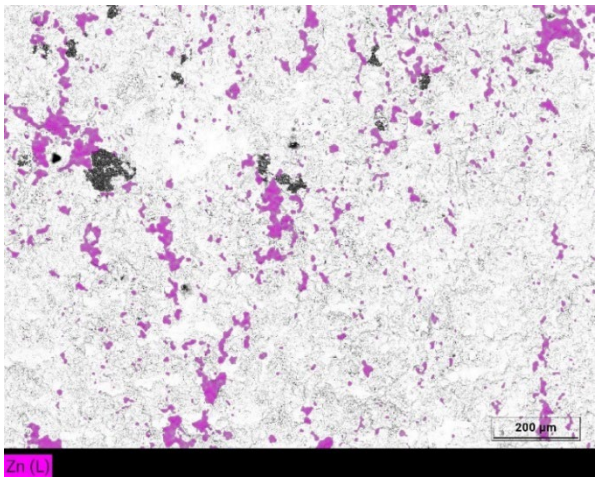

Figure 3.13 – Example of one of the 16 images of Ore gains with Zn generated by SEM-EDS for sample #1

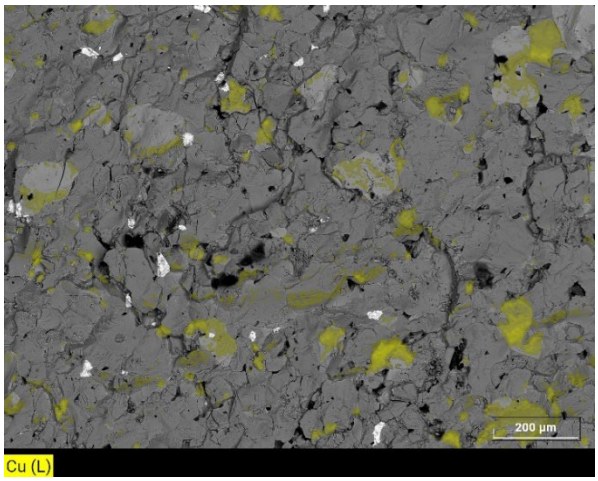

Figure 3.14 – Example of one of the 16 images of Ore gains with Cu generated by SEM-EDS for sample #2

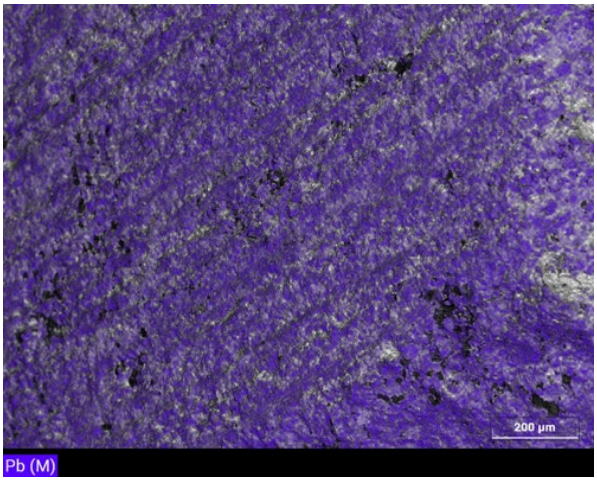

Figure 3.15 – Example of one of the 16 images of Ore gains with Pb generated by SEM-EDS for sample #3

The SEM/EDS images are stored as PNG format files. Essentially, these images have a grey background that shows the relief of the image, and then a coloured patch overlays, indicating the occurrence of a specific chemical element, in this case, one of the metals of interest (copper, zinc, or lead). For example, in the image in Figure 3.13, the occurrence of zinc ore grains (sphalerite) is represented by pink colour, while in the image in Figure 3.14, the occurrence of copper ore grains (chalcopyrite or another) is represented by yellow, and in the image in Figure 3.15, lead ore grains (galena) are represented by blue.

To process these images in the geostatistics software available at FCT-NOVA (GeoMS), the PNG images were converted to binary images and then written into ASCII files. It is worth noting that areas of the images without colour are where the selected metals are not present, and in this case, the RGB colour value is equal or similar for all three components (red, green and blue).

This format conversion (from PNG to ASCII) was carried out by a Python code specifically developed for this dissertation. Initially, the program reads the PNG file with colour values (ranging from 0 to 255) for the red, green, and blue components. It then calculates the differences between these values pairwise and applies a maximum allowable threshold to the sum of differences. If the sum of differences is less than this threshold, the pixel assumes the value zero (absence of the metal); otherwise, it assumes the value 1 (presence of the metal). In summary, the program scans for colour occurrences and binarizes the result to separate the two patches in the images.

Simultaneously with image binarization, the Python code selects a useful area of the image with 1000 by 1000 pixels, excluding areas near the threshold and the area of the image containing the scale. It is important to mention that the scale is the same for all images, and from one image and counting the pixels of the scale, a physical dimension could be associated with the pixels.

Still, within the same Python code, the various images for each sample (#1 to #5) are saved in ASCII within the same cube. In the “geoView” module of “GeoMS”, the three binary images equivalent to those in Figures 3.13 to 3.15 are illustrated (Figures 3.16 to 3.18).

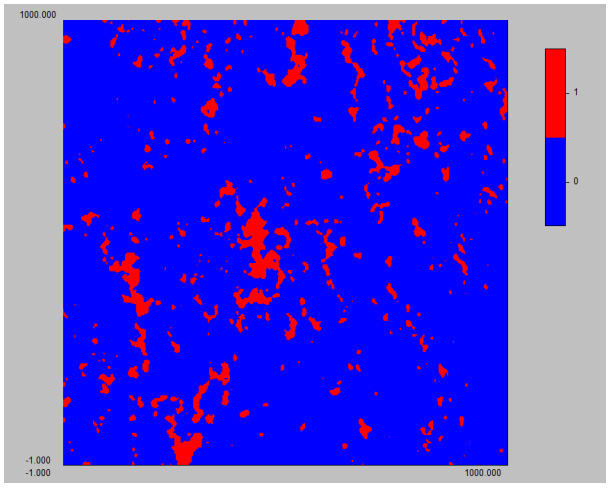

Figure 3.16 – Binary image of the Zn SEM/EDS image for sample #1

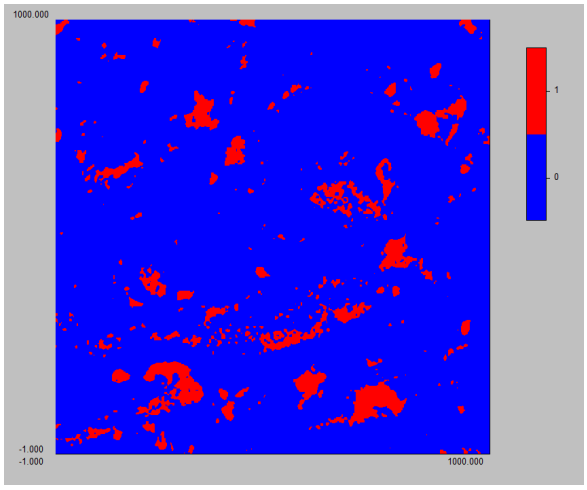

Figure 3.17 – Binary image of the Cu SEM/EDS image for sample #2

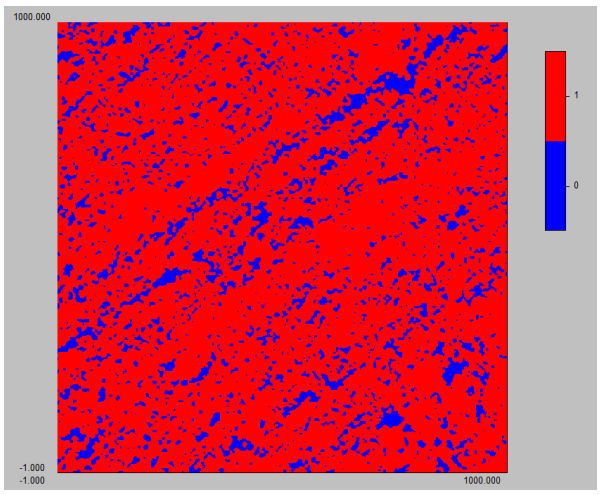

Figure 3.18 – Binary image of the Pb SEM/EDS image for sample #3

3.3.3 Geostatistical Modelling and Post Processing

The first procedure of geostatistical modelling is the calculation of the experimental variograms of the binary images converted from SEM/EDM. The variograms were calculated for each cube of data (set of images of each ore sample), meaning that the calculated variograms are treated as averages of each sample. Variograms within the cube of images were computed in the two main directions of the grid. The calculation of variograms involved the module “GeoVag” of the GeoMS software. As said before, variograms are a fundamental tool in geostatistical analysis, allowing for the quantification of spatial variation of elements within the samples.

After the calculation of experimental variograms, a theoretical model was fitted in the module “GeoMod” of the GeoMS. This iteration between “GeoVag” and “GeoMod” enabled obtaining more refined

estimates of the variograms, considering the spatial structure of the elements of interest within the samples. The results obtained with “GeoVag” were used to condition the simulations.

A noteworthy general finding emerges from the analysis of the variogram parameters, specifically the range values. It is observed that these values exhibit a relatively consistent order of magnitude across the various samples and elements, ranging from approximately 15 to 40 pixels, and the variograms are very consistent. Also, variograms are all isotropic as expected for sulphide mineral grains. This uniformity in the scale of the range parameter signifies that the spatial correlation ranges for the elements under investigation tend to share a similar magnitude, and in the case of a binary image means size of the grains. Also, the nugget effect was inexistent due to the use of images to compute the variograms and meaning that the images capture well the grain sizes.

After the calculation of variograms and fitting of a theoretical model for each sample / metal, the simulation of images was finally performed by SIS. The SIS was a crucial phase in this study, where each sample and metal presence were meticulously modelled. Each 3D simulated image reproduces a possible realization of the reality, enabling the generation of 3D patterns of the grains from 2D SEM/EDS images.

The SIS algorithm was executed to generate a 3D cube of pixels measuring 200 x 200 x 200 units (8 million of pixels each). Also, as this study has an exploratory behaviour, only one realization was made for each sample / metal. It is important to remark that simulations are made unconditional to data, and the range of the variogram is significatively lower than the 200 unis, this each image cam be seen as representative of the reality. The simulation images are bellow figures 3.19 to 3.21.

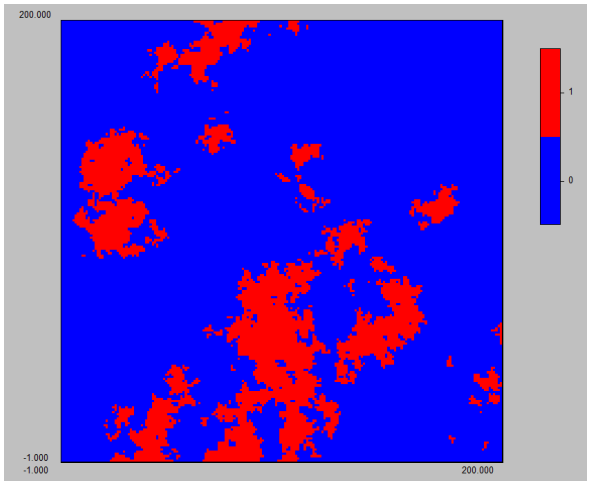

Figure 3.19 – Example one simulated realization of SIS for Zn of sample #1

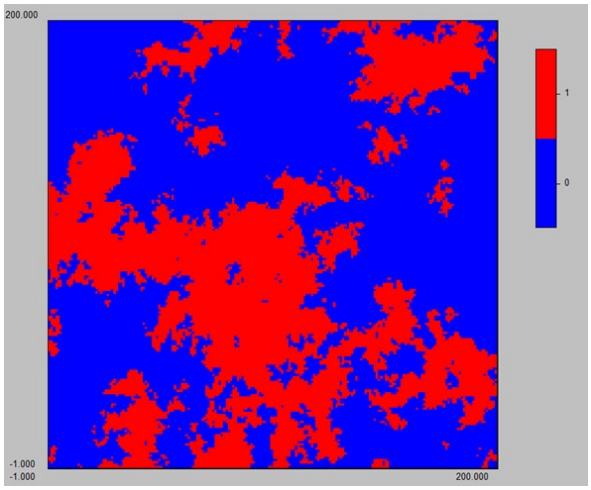

Figure 3.20 – Example one simulated realization of SIS for Cu of sample #2

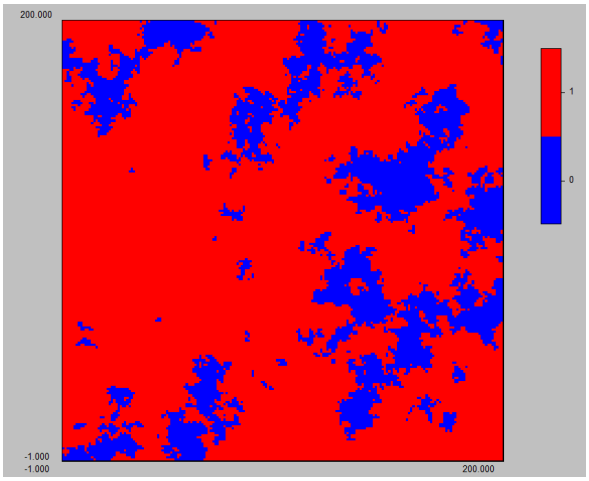

Figure 3.21 – Example one simulated realization of SIS for Pb of sample #3

In this phase of the work, a second Python script was developed to investigate the statistical distribution of a specific mineral within a simulated grid. Thus, this step acts as simulated different mill sizes and evaluating the fraction of pure metal grains, mixed and no metal grains.

This Python function imports the simulated binary cube and evaluates grain statistics as follows:

I. Selection of a 3D grain size, corresponding to a 3D template (5x5x5, 10x10x10, etc.).

II. Random selection of a pixel in the analysed cube and placement of the template for analysis.

III. Statistical evaluation of pixels of type "1" versus those of type "0". The results can be 100% (template with 100% metal), 0% (template with 0% metal), or an intermediate value, which is the most common. This statistical analysis is conducted in 3D.

IV. Return to II) for the random selection of a new position until the required templates, numbering in the order of a few million, are generated.

V. Return to I), change the template size, and repeat points II) to IV).

The summary of the methodology applied during the project is presented in the sketch below, figure 3.22.

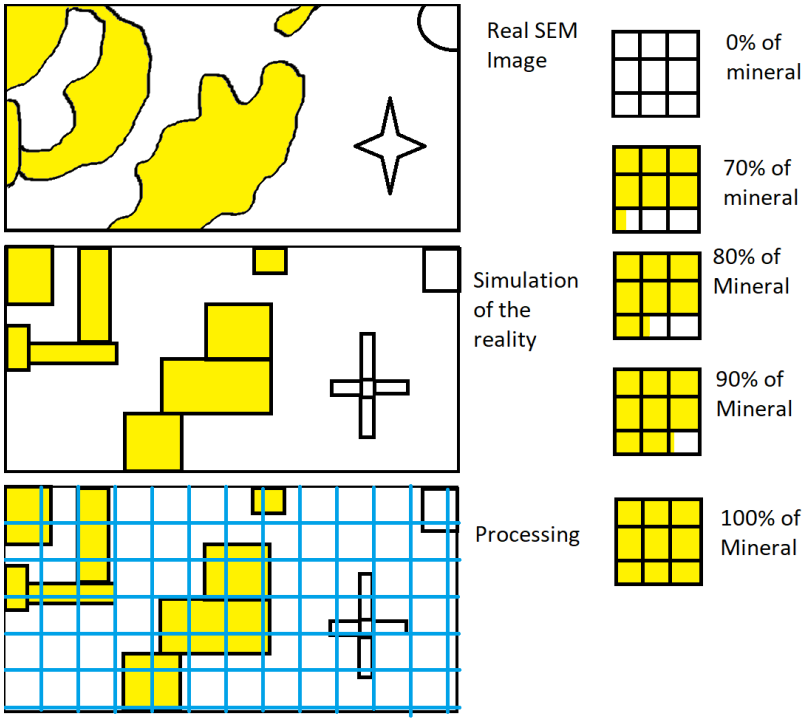

Figure 3.22 – Sketch of the methodology applied during this post-processing step.

The primary objective was to examine how the presence of this mineral varied across different spatial scales, represented by grids of varying sizes. Each grid cell within the simulation had a binary value: '1' signifying the presence of the target mineral and '0' indicating its absence or non-mineral content. Values of the template between '0' and '1' represented mixed grains, potentially containing both the mineral and non-mineral components.

The general findings presented here provide valuable insights into the initial outcomes of the procedure. As we move into the main discussion and case study, these findings will establish a foundational understanding of how varying grid sizes and mineral concentrations influence the results. The observed trends, the role of variograms, and the successful execution of the procedure, except for unusually high lead concentrations, set the stage for a comprehensive analysis in the subsequent sections. In the upcoming case study, we will delve into greater detail, explore potential implications, and draw meaningful conclusions to contribute to our broader understanding of mineral distribution within the simulated grid.

4 CASE STUDY

In the forthcoming case study chapter, a thorough examination of the variograms of the binary images and the Sequential Indicator Simulation (SIS) results is presented. These critical findings contribute to a deeper understanding of the patterns in mineral distribution across our samples. By engaging in careful interpretation and analysis, our objective is to unravel the intricacies exposed through variogram modelling, shedding light on the distinct behaviours of various minerals within the samples.

4.1 Statistics of SEM Images

Table 4.1 outlines the composition of three selected samples for this practical case study, denoted as sample #1, sample #2, and sample #3, with respect to mineral and matrix contents. Each sample exhibits varying percentages of Cu, Pb, and Zn, alongside their corresponding matrix components.

Table 4.1 – Summary of the statistics of the images

Samples	Number of images	Metal present	Mineral (%)	Matrix (%)
#1	18	Copper	8.83	91.17
		Lead	94.73	5.27
		Zinc	18.65	81.35
#2	16	Copper	34.77	65.23
		Lead	65.50	34.50
		Zinc	12.21	87.79
#3	16	Copper	17.46	82.54
		Lead	77.53	22.47
		Zinc	21.91	78.09

4.2 Indicator Variograms

As previously discussed, variograms play a pivotal role in our geostatistical analysis. Employing the "GEOMod" module within GEOMS, we computed experimental indicator variograms for grain images to extract valuable insights into the spatial relationships among minerals. These variograms serve as a foundational tool in our endeavour to generate precise and informative 3D simulations.

4.2.1 Sample #1, M_{Zn}

Figures 4.1 to 4.3 presents each one an example of one binary image of minerals (red) grains vs matrix (blue) for sample #1. Graphics 4.1 to 4.3 presents the correspondent experimental variograms and the theoretical model fitted.

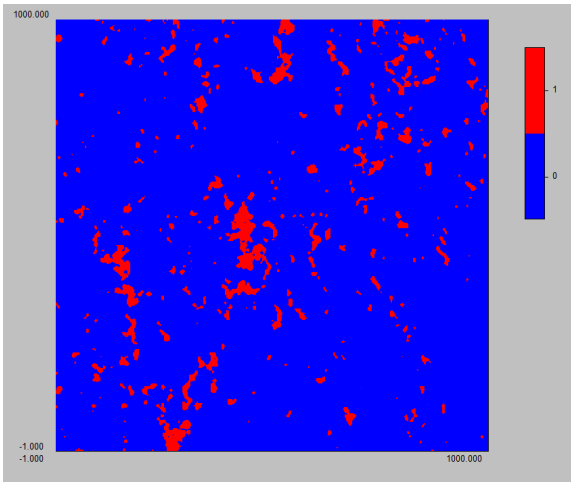

Figure 4.1 – Binary image of Cu map from sample #1

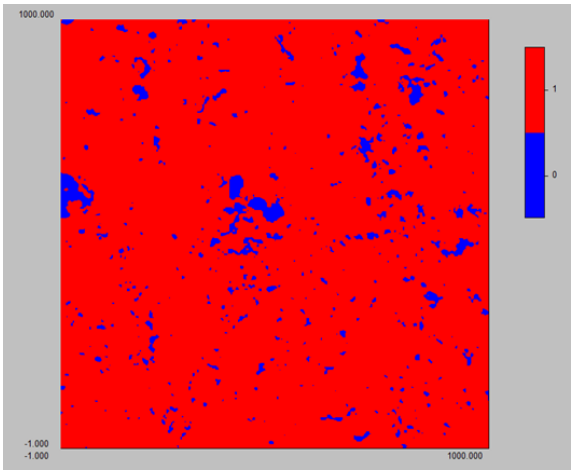

Figure 4.2 – Binary image of Pb map from sample #1

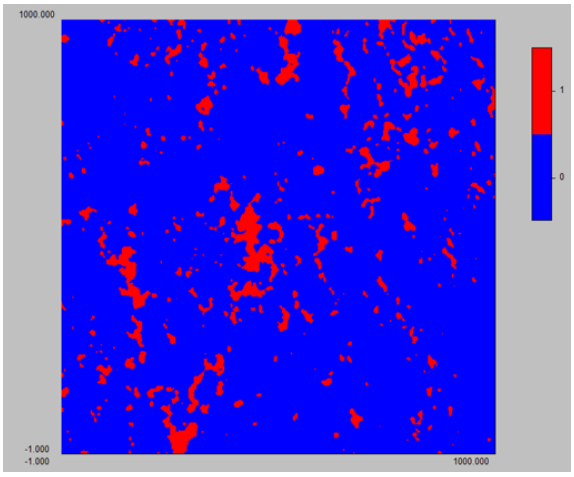

Figure 4.3 – Binary image of Zn map from sample #1

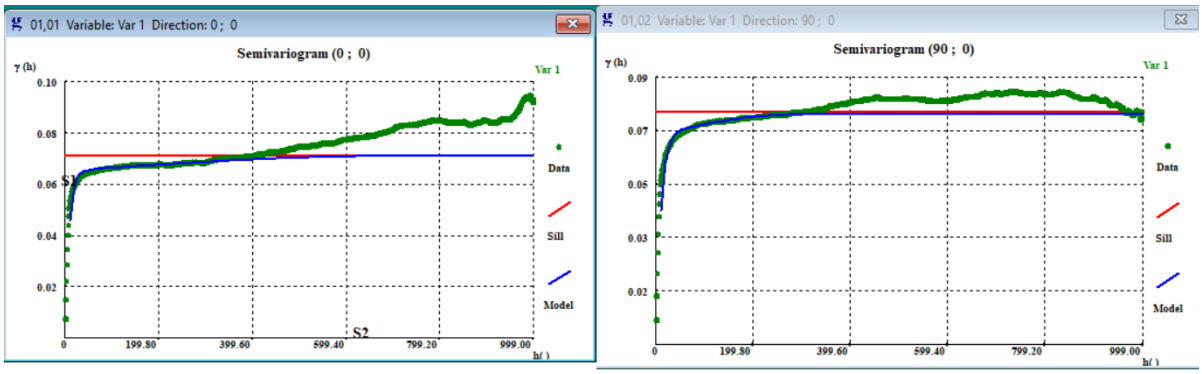

Graphic 4.1 – Variograms for both directions (0;0) and (90;0) for Cu from sample #1

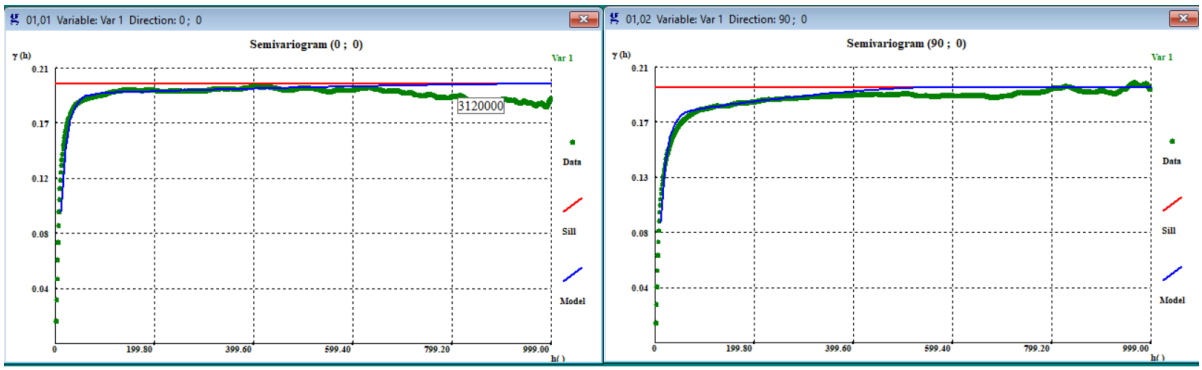

Graphic 4.2 – Variograms for both directions (0;0) and (90;0) for Pb from sample #1

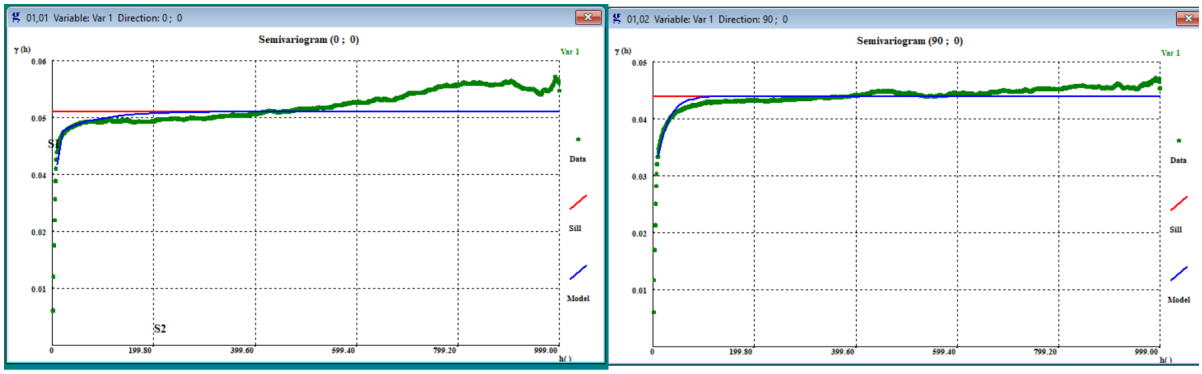

Graphic 4.3 – Variograms for both directions (0;0) and (90;0) for Zn from sample #1

4.2.2 Sample #2, M_{Cu}

For sample #2, figures 4.4 to 4.6 presents each one an example of one binary image of minerals (red) grains vs matrix (blue). Graphics 4.4 to 4.6 presents the correspondent experimental variograms and the theoretical model fitted.

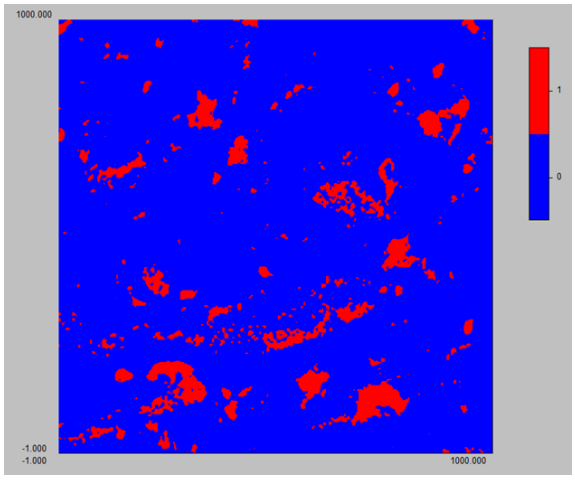

Figure 4.4 – Binary image of Cu map from sample #2

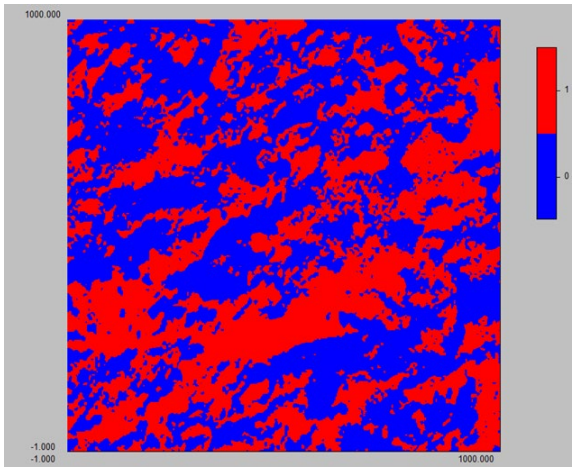

Figure 4.5 – Binary image of Pb map from sample #2

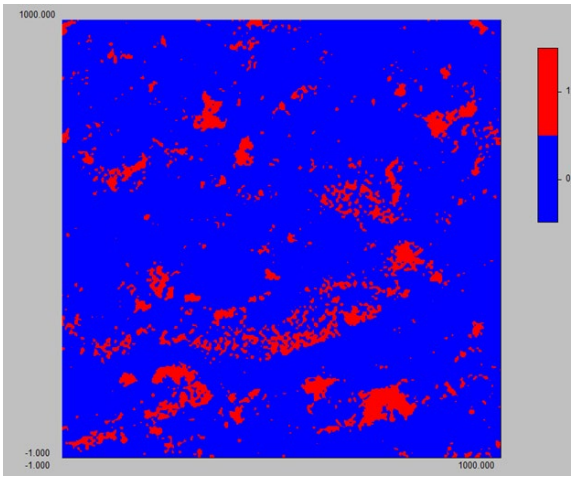

Figure 4.6 – Binary image of Zn map from sample #2

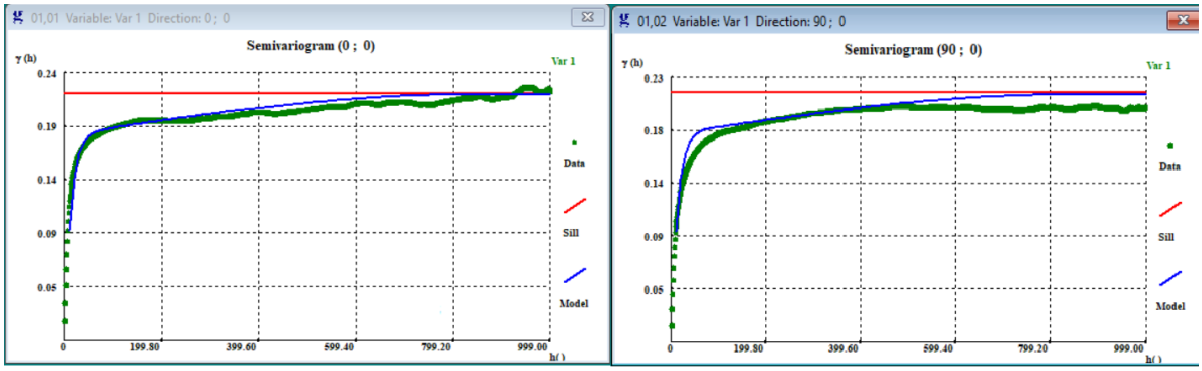

Graphic 4.4 – Variograms for both directions (0;0) and (90;0) for Cu from sample #2

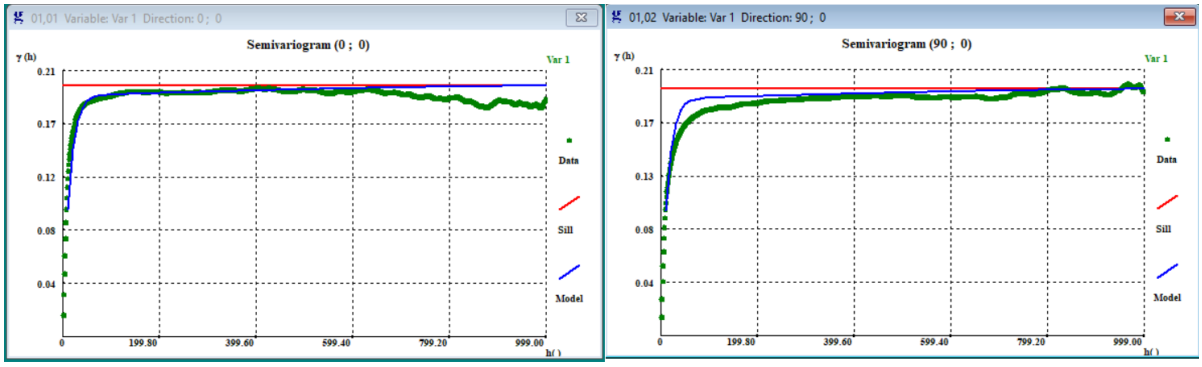

Graphic 4.5 – Variograms for both directions (0;0) and (90;0) for Pb from sample #2

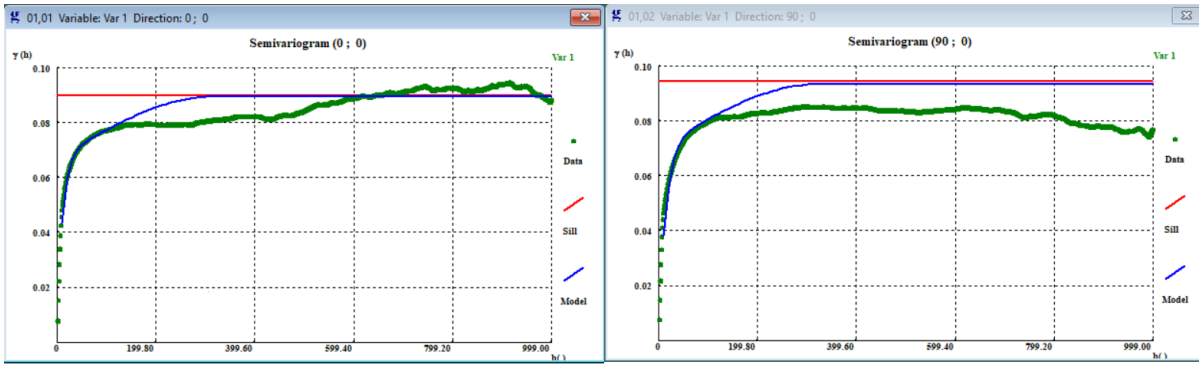

Graphic 4.6 – Variograms for both directions (0;0) and (90;0) for Zn from sample# 2

4.2.3 Sample #3, M_{Cu}

To complete this analysis, figures 4.7 to 4.9 presents each one an example of one binary image of minerals (red) grains vs matrix (blue) for sample #3. Graphics 4.7 to 4.9 presents the correspondent experimental variograms and the theoretical model fitted.

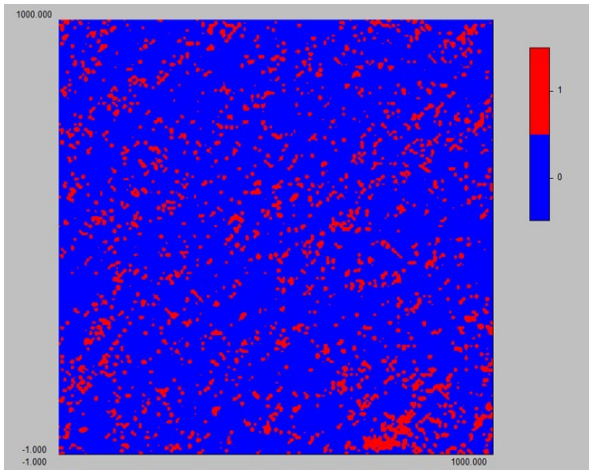

Figure 4.7 – Binary image of Cu map from sample #3

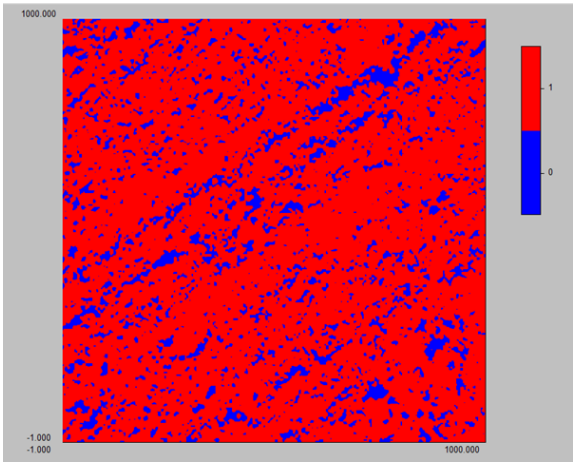

Figure 4.8 – Binary image of Pb map from sample #3

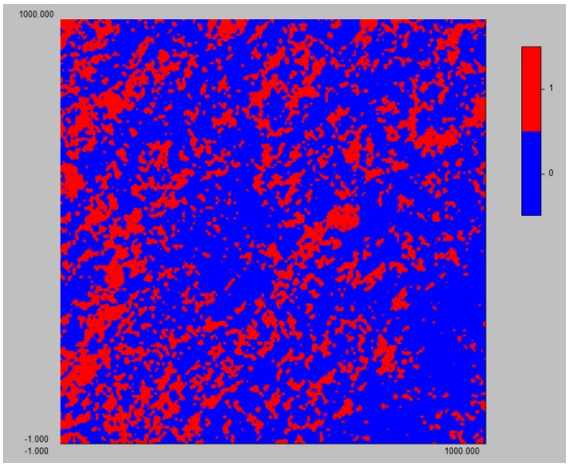

Figure 4.9 – Binary image of Zn map from sample #3

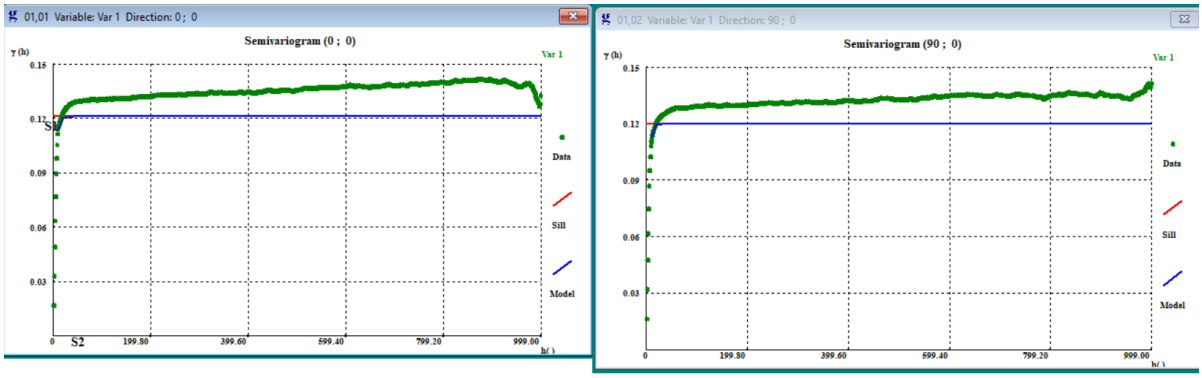

Graphic 4.7 – Variograms for both directions (0;0) and (90;0) for Cu from sample #3

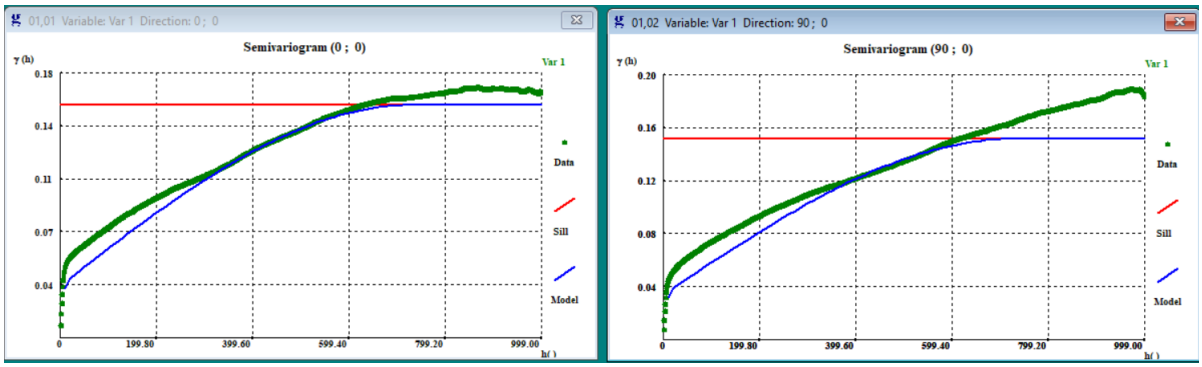

Graphic 4.8 – Variograms for both directions (0;0) and (90;0) for Pb from sample #3

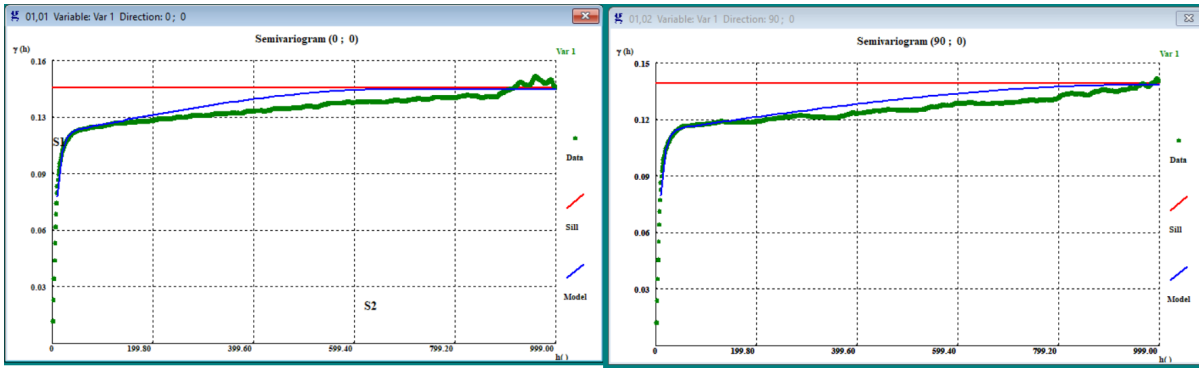

Graphic 4.9 – Variograms for both directions (0;0) and (90;0) for Zn from sample #3

4.2.4 Summary of Results

A summary table of theoretical variogram models' parameters is presented in Table 4.2. The corresponding graphs (from 4.1 to 4.9) below illustrate the visual representation of these variograms.

Table 4.2 – Summary of the variables of the variograms (E-exponential model; S-Spherical model)

Sample	Element	C0	Model 1			Model 2		
			Type	C_1	a_1	Type	C_2	a_2
#1	Cu	0	E	0.068	25	S	0.006	700
	Pb	0	E	0.188	40	S	0.008	1120
	Zn	0	S	0.043	15	E	0.005	220
#2	Cu	0	E	0.181	40	S	0.035	840
	Pb	0	E	0.188	40	S	0.008	1120
	Zn	0	E	0.07	30	S	0.0235	310
#3	Cu	0	E	0.118	10	S	0.001	40
	Pb	0	E	0.035	15	S	0.12	725
	Zn	0	E	0.116	25	S	0.025	680

4.2.4.1 Comparison between Copper variograms

The analysis of the variogram model parameters for copper mineral grains has the potential to relate to the spatial distribution and variability of metal mineral grains in each sample.

The variogram analysis of ore samples #1, #2, and #3, focused on copper properties, reveals the absence of variability at a small scale (nugget effect), and the points of the experimental variogram fit well with two functions in all analysed cases, combining a first exponential-type structure (Model E) with a second spherical-type structure (Model S). In all cases, the first structure is the most significant, with a significantly higher sill compared to the sill of the second structure. Another important aspect is that there is isotropy in all the mages / results.

For example, sample #1 is fitted with a first exponential function and a range of 25 units (a1), while the second function is spherical with a range on the order of 700 units (Graph 4.1). These two common

structures in most samples suggest that the grains have a regular-sized pattern (first structure) and that the grains tend to cluster in patches with the dimension of the second structure.

Focusing on sample #2, which has the highest copper fraction, the sill values are higher due to greater variability (variance) in the image, but this aspect is not relevant in the analysis of grain size. An important aspect is that the range is higher in both structures (see Graph 4.4) compared to samples #1 and #3, suggesting that mineral patches are larger in this sample #2 than in the other two analysed.

To conclude this analysis, sample #3, which has the lowest fraction of copper mineral grains, exhibits relatively smaller sill and range values. These observations align with the expected lower fraction of copper minerals in this sample, reinforcing the validity of the variogram analysis.

4.2.4.2 Comparison between Lead variograms

In the case of lead minerals, the nugget effect is also consistently equal to zero, revealing that the grains and matrix tend to exhibit very regular and without discontinuous random features at very small scale.

Regarding the sills of the two structures, it is observed that in samples #1 and #2, the first sill is much more significant than the second, while in sample #3, the magnitude of the sills is reversed. In this case, structure 2 is much more relevant than structure 1, meaning a more continuous structure.

An exploration of the range parameter further clarifies the spatial dependence of lead content. Samples #1 and #2 exhibit identical range values for both structures, suggesting similar spatial dependence characteristics. This convergence in variogram characteristics highlights a similarity in the spatial distribution of lead mineral content in these samples, despite the expected variation in zinc minerals. The implication of a possible correlation between zinc and lead distribution patterns in these samples emerges from this observation (graphs 4.2 and 4.5).

Sample 3, characterized by its lower lead content, is distinguishable by slightly lower sill values than samples #1 and #2. It also exhibits reduced amplitudes, indicating that the spatial dependence of lead content is confined to more restricted distances in contrast to the other samples (graph 4.8).

4.2.4.3 Comparison between Zinc variograms

Also, for the images of zinc minerals, the nugget effect (C0) is consistently set to 0, suggesting a notable small-scale continuity without random transitions.

The sills of the three samples have significant differences, especially sample #3, which exhibits the highest values, with the variance of this sample being higher than the others.

The fitted functions are always the sum of 2 structures, with sample #1 combining a spherical model with an exponential model, and samples #2 and #3 summing an exponential function with a spherical function.

Regarding samples #1 and #2, the amplitudes are considerably lower than those of sample #3, with a greater emphasis on the amplitude of the second structure. This lower amplitude, associated with

increased variability indicated by the sill, suggests a more dispersed distribution of zinc content throughout the samples (#1 and #2) and in small grains (see graphs 4.2 and 4.5). Sample #3 emerges with higher amplitudes, indicating both a more extensive spatial dependence range and higher overall variability in zinc content (graph 4.8).

4.2.5 Discussion Summary

The three studied samples exhibit distinctive intrinsic characteristics in their mineral composition and grain size, pertaining to the distribution of copper, lead, and zinc minerals, which can be partially quantified through their experimental variograms and theoretical models.

To begin with, all sample variograms were fitted without a nugget effect, indicating the absence of small grains scattered throughout the sample, including both the analysed minerals in the matrix and their inverses.

Likewise, the variograms of all images were fitted with two structures (spherical plus exponential or vice versa), and the weight of each structure is gauged by the relationship between the sills one and two. The magnitude of the sum of the sills is not inherently crucial, as it is associated with the variance of the image, and the variance, in turn, is linked to the ratio between ones and zeros. As the balance between zeros and ones equalizes, the variance increases to a theoretical maximum of 0.25, reached when the proportion of zeros equals the proportion of ones (50/50).

Regarding the variogram ranges, the amplitudes of the first structure for all samples fall within the range of 10-40 units (pixels), while the second range is in the order of several hundred, and even thousands of pixels (in this case, the amplitude is estimated by extrapolation, for example, Pb in sample #2). These two structures and amplitudes are associated with the grain size (amplitude of the first structure) and the spatial arrangement of the grains (amplitude of the second structure). Thus, the grains have dimensions between 10 and 40 pixels, forming clusters or patches with dimensions of a few hundred pixels.

In addition to these considerations, it is crucial to reiterate that all variograms are isotropic in the analysed planes, all variograms are calculated in 2D, and each variogram represents an average not of one but of several images (see Table 4.2).

4.3 Simulation of Mineral Particles

In this section, the simulation of the 3D indicatrix of the spatial distribution of copper, lead, and zinc mineral grains is carried out by SIS, followed by the evaluation of the relationship between grain dimensions and the fraction of the minerals of interest or the host rock. The simulated images are conditioned to the basic statistics of the samples from the SEM (see Table 4.1) and the variogram

models adjusted in the previous section. Due to processing capacity constraints, the simulation is performed in 3D in a cube with 200x200x200 cells (8 million cells), while the original information remains as 2D images with 1000x1000 cells. Since the images are generated without conditioning, only one image is considered for each sample and metal under analysis.

To interpret the results in the context corresponding to real-world dimensions, the actual dimension of the cells was determined based on the analysis of the captions of scanning electron microscope (SEM) images. Thus, each 2D cell corresponds to a square with 0.9090 µm sides.

The statistical results for each image are presented in tables and bar charts. In each table, the fraction of copper mineral grains, mixed grains, and non-copper grains is listed for three grain purity cut-off values, respectively 70%, 80%, and 90%. The assessment is conducted by sampling the simulated cubes for grain sizes ranging from 10x10 cells to 100x100 cells, i.e., between 4,545 µm and 90.9 µm.

4.3.1 Simulation of Copper Particles

4.3.1.1 Sample #1, MZn

In Figure 4.10, an example is provided of a plane from the simulated cube, where red cells represent copper (Cu) minerals and the blue background represents the matrix with other minerals. Table 4.3 displays the fraction of copper mineral grains, mixed grains, and non-copper grains for the three mentioned cut-off values. Cube simulation is conditioned to statistics of copper of the sample #1. The fraction of red cells is around 8.83%.

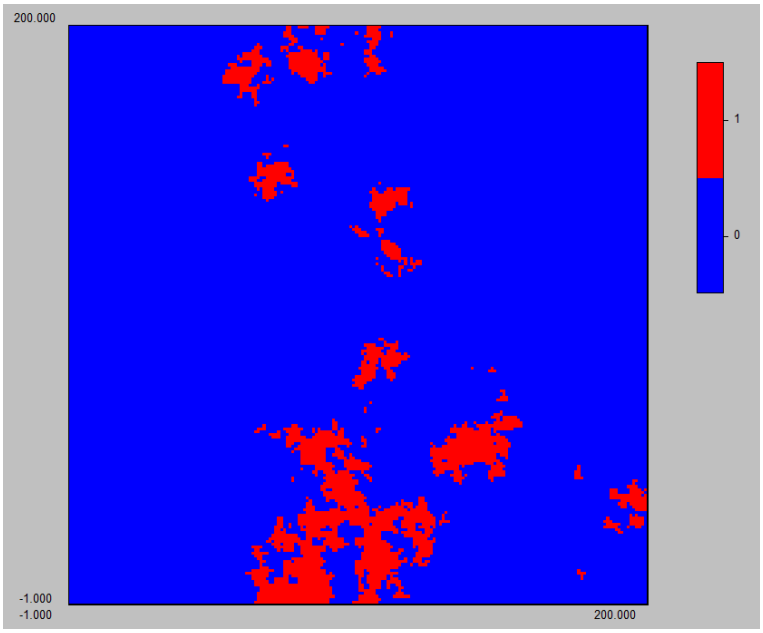

Figure 4.10 – Example of a simulated image on a random plane of the 3D simulated cube depicting copper mineral grains, conditioned to the statistics of sample #1.

Table 4.3 – Probabilities of encountering copper grains in simulated images with statistics of sample #1 across different mesh's

Grain size in µm	Frequency of grains with at least 70%, 80% or 90% of particles of Cu, matrix, or mixed								
	70%			80%			90%		
	Cu	mixed	not Cu	Cu	mixed	not Cu	Cu	mixed	not Cu
4.545	4%	8%	87%	3%	13%	84%	1%	19%	80%
9.09	2%	10%	88%	1%	16%	83%	0%	25%	75%
13.635	1%	10%	89%	0%	17%	83%	0%	28%	72%
18.18	0%	9%	91%	0%	17%	83%	0%	31%	69%
22.725	0%	7%	93%	0%	16%	84%	0%	33%	67%
27.27	0%	6%	94%	0%	15%	85%	0%	35%	65%
36.36	0%	3%	97%	0%	11%	89%	0%	37%	63%
45.45	0%	0%	100%	0%	7%	93%	0%	38%	62%
68.175	0%	0%	100%	0%	0%	100%	0%	31%	69%
90.9	0%	0%	100%	0%	0%	100%	0%	17%	83%

Table 4.3 shows that for a cut-off fraction of 70%, only a very fine fragmentation of the sample captures grains that are tendentially monomineralic. Even at this level of fragmentation, a minority of 4% of the sampled grains meets the criteria for "pure" copper mineral grains, 8% of the samples are identified as "mixed," and the majority of grains, around 87%, are "non-copper" (see graphic 4.10).

When the grain purity level is more stringent, in this case, 80%, these percentages decrease for all granulometries, and the same occurs when the criterion is more demanding at 90% purity, where only 1% of the grains meet this criterion. These samples are characterized by a moderate to low concentration of copper grains; hence, the fragmentation needs to be very fine to capture pure grains.

In contrast, the fraction of non-copper minerals is always high for all purity levels, although it obviously decreases with higher stringency. Increased stringency (higher cut-off) converts more grains into mixed compositions.

Graphic 4.10 – Particles of copper, non-copper (matrix), and mixed distribution across various mesh sizes in a simulated image with the statistics of sample #1.

4.3.1.2 Sample #2, MCu

In Figure 4.11, an example is provided of a plane from the simulated cube, where coloured cells have the same meaning of the previous analysis. Again, table 4.4 displays the fraction of copper mineral grains, mixed grains, and non-copper grains for the three mentioned cut-off values. Cube simulation is conditioned to statistics of copper of the sample #2 around 34.77% of red cells.

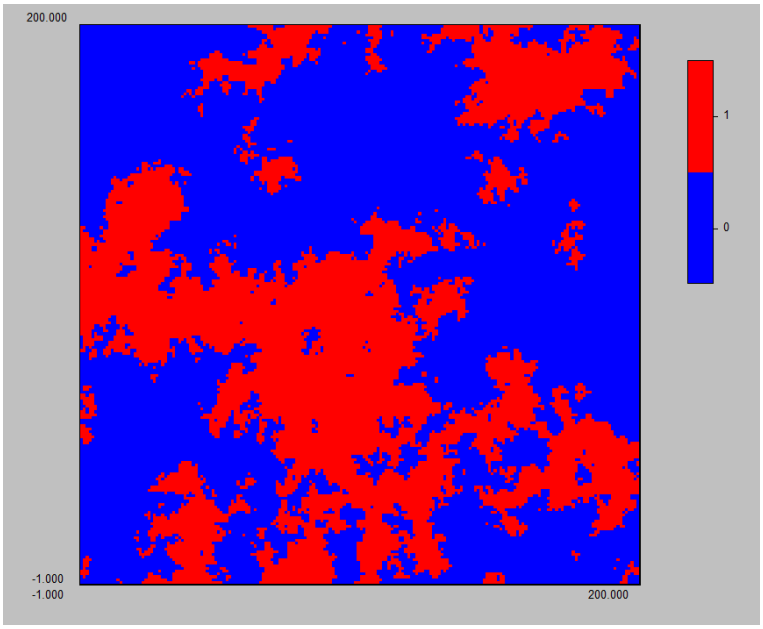

Figure 4.11 – Example of a simulated image on a random plane of the 3D simulated cube depicting copper mineral grains, conditioned to the statistics of sample #2.

Table 4.4 – Probabilities of encountering copper grains in simulated images with statistics of sample #2 across different mesh's

Grain size in µm	Frequency of grains with at least 70%, 80% or 90% of particles of Cu, matrix, or mixed								
	70%			80%			90%		
	Cu	mixed	not Cu	Cu	mixed	not Cu	Cu	mixed	not Cu
4.545	22%	23%	54%	17%	35%	48%	11%	51%	38%
9.09	16%	34%	51%	10%	51%	39%	4%	70%	26%
13.635	12%	40%	48%	5%	60%	34%	1%	79%	19%
18.18	7%	48%	44%	2%	70%	28%	0%	88%	12%
22.725	4%	54%	41%	0%	77%	23%	0%	92%	8%
27.27	1%	61%	38%	0%	82%	18%	0%	96%	4%
36.36	0%	69%	31%	0%	91%	9%	0%	99%	1%
45.45	0%	74%	26%	0%	97%	3%	0%	100%	0%
68.175	0%	88%	12%	0%	100%	0%	0%	100%	0%
90.9	0%	99%	1%	0%	100%	0%	0%	100%	0%

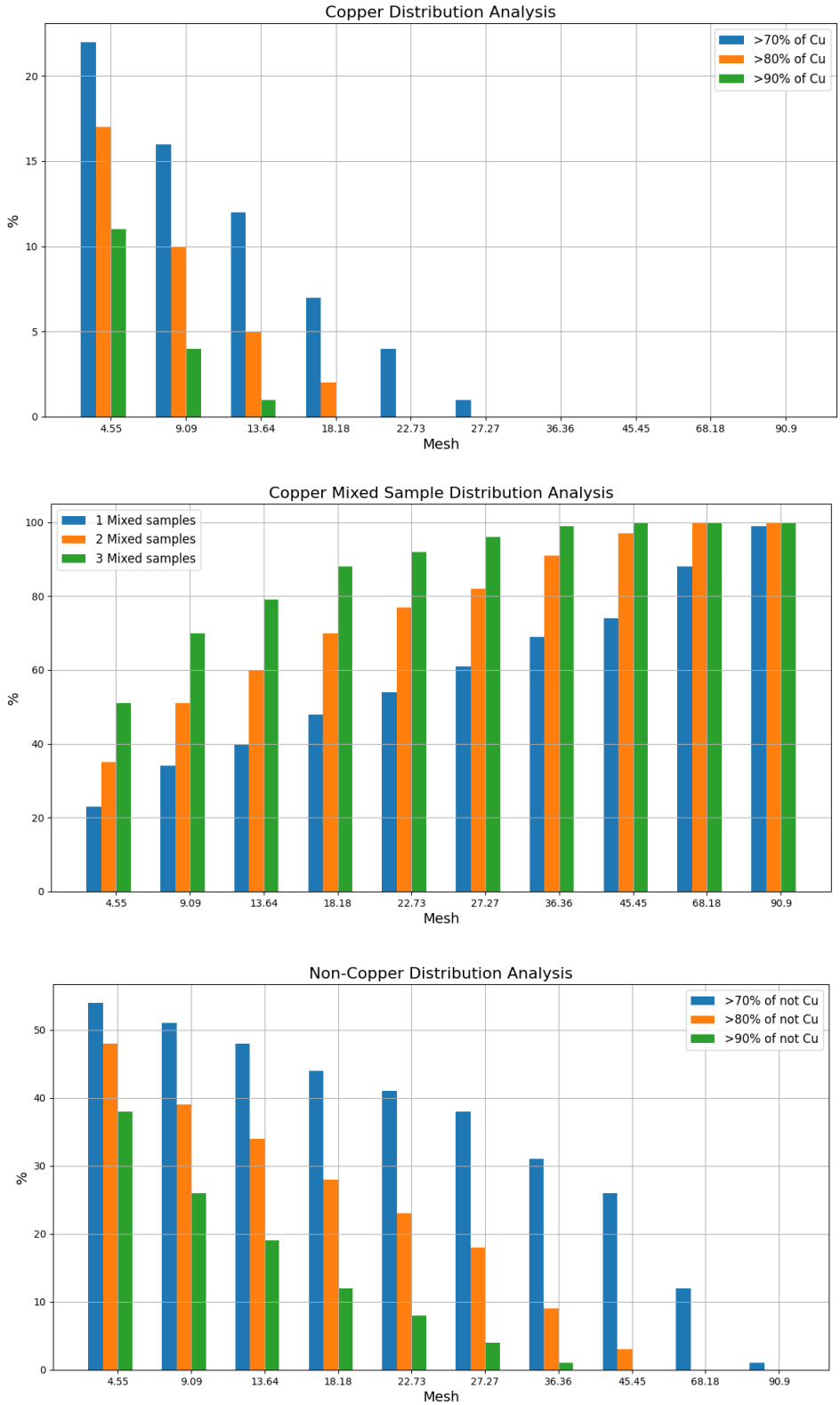

Graphic 4.11 – Particles of copper, non-copper (matrix) and mixed distribution across different mesh in simulated image with statistics of sample #2.

Sample #2 contains a higher fraction of copper minerals, so it is noticeable that for all three levels of grain purity requirements, the percentages of tendentially monomineralic grains are markedly higher, reaching up to 20%. Once again, as the grain size increases, these frequencies of pure grains drop rapidly. It is interesting to highlight that when the grain size is 4,545 μm (the smallest size analysed), for a purity requirement of 70%, the fraction of mixed grains is equal to that of pure grains.

The frequency of non-copper grains follows a trend similar to that of pure grains, such that as the purity requirement increases, both copper and non-copper grains convert into the mixed class.

4.3.1.3 Sample #3, MCu

In Figure 4.12, an example is provided of a plane from the simulated cube, where coloured cells have the same meaning of the previous analysis. Again, table 4.5 displays the fraction of copper mineral grains, mixed grains, and non-copper grains for the three mentioned cut-off values. Cube simulation is conditioned to statistics of copper of the sample #3 around 17.46% of red cells.

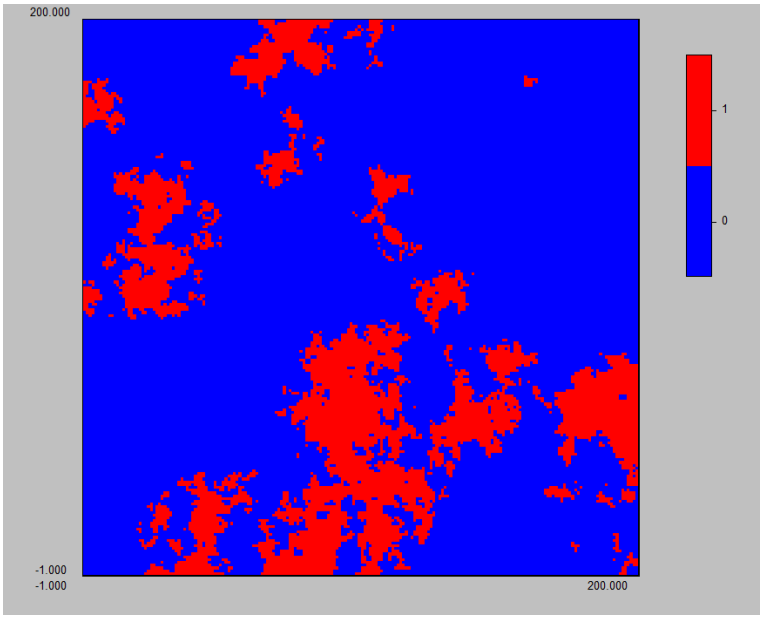

Figure 4.12 – Example of a simulated image on a random plane of the 3D simulated cube depicting copper mineral grains, conditioned to the statistics of sample #3.

Table 4.5 – Probabilities of encountering copper grains in simulated images with statistics of sample #3 across different mesh's

Grain size in µm	Frequency of grains with at least 70%, 80% or 90% of particles of Cu, matrix, or mixed								
	70%			80%			90%		
	Cu	mixed	not Cu	Cu	mixed	not Cu	Cu	mixed	not Cu
4.545	9%	15%	76%	6%	24%	70%	3%	34%	63%
9.09	5%	20%	75%	2%	31%	67%	0%	45%	54%
13.635	2%	21%	76%	1%	34%	65%	0%	50%	49%
18.18	1%	22%	77%	0%	36%	63%	0%	56%	44%
22.725	0%	22%	78%	0%	37%	63%	0%	61%	39%
27.27	0%	20%	80%	0%	39%	61%	0%	66%	34%
36.36	0%	14%	86%	0%	41%	59%	0%	75%	25%
45.45	0%	7%	93%	0%	44%	56%	0%	82%	18%
68.175	0%	0%	100%	0%	41%	59%	0%	95%	5%
90.9	0%	0%	100%	0%	25%	75%	0%	100%	0%

Sample #3 contains an intermediate fraction of copper minerals compared to samples #1 and #2. It is noticeable that, for all three levels of grain purity requirements, the percentages of tendentially monomineralic grains are also intermediate compared to those presented for the other tested samples #1 and #2. The most favourable value is 9%, obtained for a grain size of 4,545 µm (the smallest size analysed) with a purity requirement of 70%.

The frequency of non-copper grains follows a trend similar to that of pure grains, so, like in the other samples, as the purity requirement increases, both copper and non-copper grains convert into the mixed class.

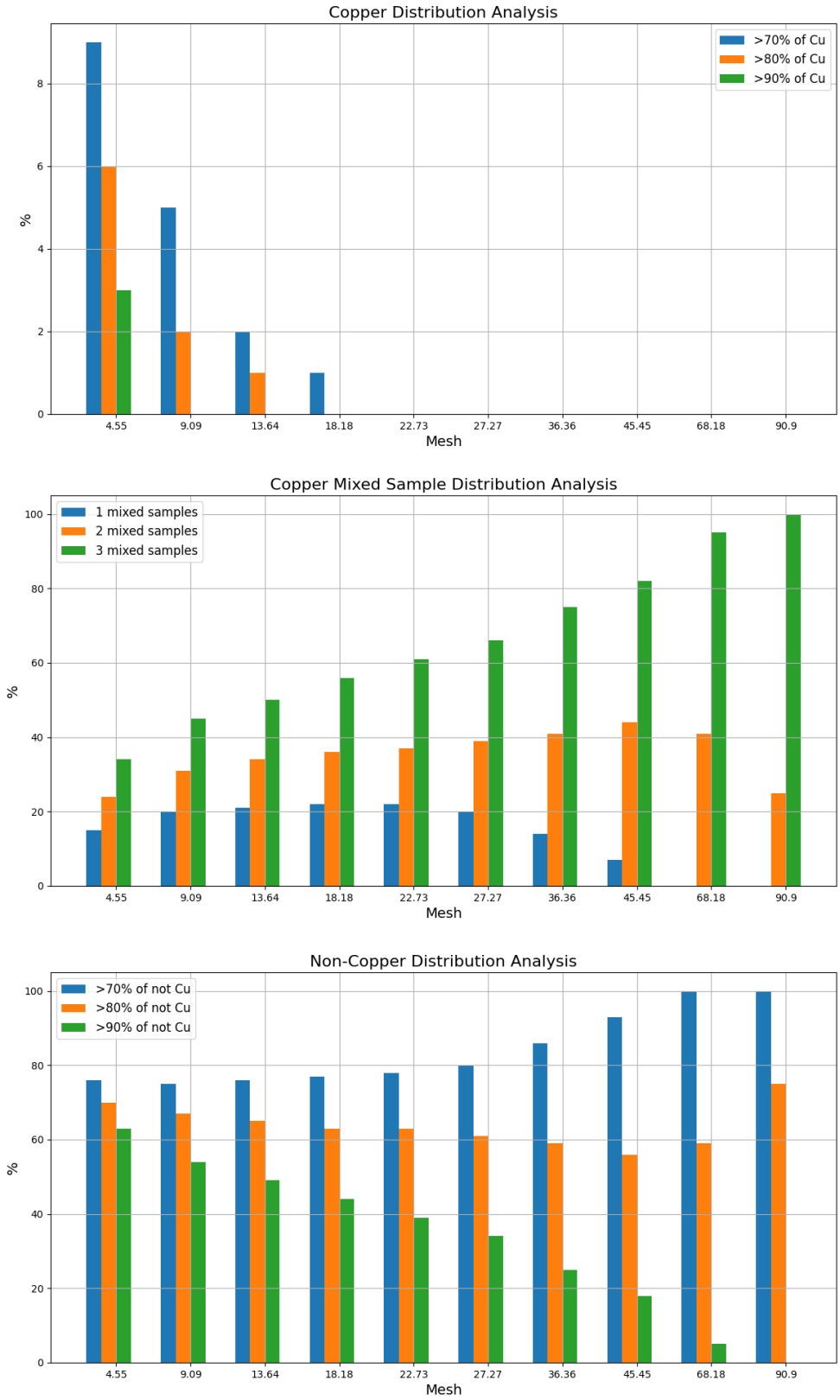

Graphic 4.12 – Particles of copper, non-copper (matrix) and mixed distribution across different mesh in simulated image with statistics of sample #3.

The percentage of mixed grains for threshold of purity of 70% in copper particles increases as the mesh size increases, and reaches its peak at 22% for a mesh size of 45.45 µm. This indicates that for larger mesh sizes, there is a substantial likelihood of encountering samples with diverse mineral compositions, even when the copper content is high. This finding highlights the complexity of mineral mixtures within these samples (see graph 4.12). As threshold of purity increases, the mixed grains percentage increases, and reaches 100% for larger grains. This emphasizes how coarser meshes favour lower copper concentrations and metal recovery.

Regarding samples that do not meet copper content thresholds (below 70%), smaller mesh sizes consistently exhibit a higher proportion of "non-copper," indicating that finer particles are more likely to contain varied mineral compositions beyond copper (see graph 4.12).

4.3.1.4 Discussion

A sample 1 exhibits a low fraction of copper minerals. Thus, for a purity requirement of at least 70%, for the two finer evaluated fragmentations of 4.55 and 9.09 µm, 4% and 2% of the grains, respectively, contain over 70% copper minerals. However, as the grain size increases, this percentage consistently decreases, suggesting that smaller particles tend to display higher copper concentrations and fewer mixed particles.

Sample #2 stands out for having a high fraction of copper minerals, and consequently, the fraction of pure particles is much higher than that of sample #1. Nevertheless, as the grain size increases, the fraction of pure particles decreases very rapidly.

Sample #3 presents an intermediate percentage of copper, and the results are consistently intermediate compared to samples #1 and #2. However, the percentage of mixed samples in sample #3 consistently lags behind sample #2, indicating a transfer of frequency to non-copper grains in this sample.

4.3.2 Simulation of Lead Particles

4.3.2.1 Sample #1, MZn

In Figure 4.13, an example is provided of a plane from the simulated cube, where red cells represent lead (Pb) minerals and the blue background represents the matrix with other minerals. Table 4.6 displays the fraction of lead mineral grains, mixed grains, and non-lead grains for the three mentioned cut-off values. Cube simulation is conditioned to statistics of lead of the sample #1. The fraction of red cells is around 94,73%.

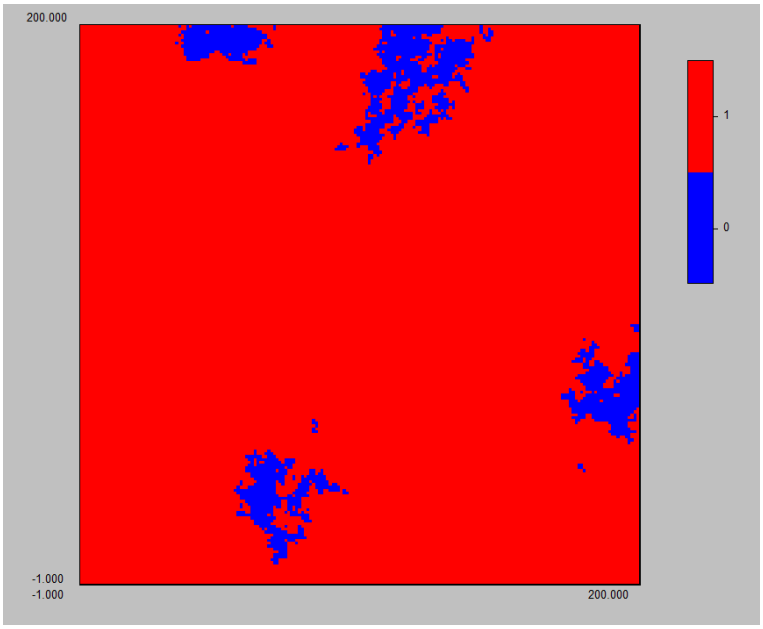

Figure 4.13 – Example of a simulated image on a random plane of the 3D simulated cube depicting lead mineral grains, conditioned to the statistics of sample #1.

Table 4.6 – Probabilities of encountering lead grains in simulated images with statistics of sample #1 across different mesh's

Grain size in µm	Frequency of grains with at least 70%, 80% or 90% of particles of Pb, matrix, or mixed								
	70%			80%			90%		
	Pb	mixed	not Pb	Pb	mixed	not Pb	Pb	mixed	not Pb
4.545	92%	5%	3%	90%	8%	2%	88%	11%	1%
9.09	92%	7%	1%	89%	10%	1%	84%	16%	0%
13.635	93%	7%	1%	89%	11%	0%	82%	18%	0%
18.18	94%	6%	0%	89%	11%	0%	81%	19%	0%
22.725	95%	5%	0%	89%	11%	0%	79%	21%	0%
27.27	96%	4%	0%	91%	9%	0%	78%	22%	0%
36.36	98%	2%	0%	94%	6%	0%	78%	22%	0%
45.45	99%	1%	0%	97%	3%	0%	80%	20%	0%
68.175	100%	0%	0%	100%	0%	0%	89%	11%	0%
90.9	100%	0%	0%	100%	0%	0%	96%	4%	0%

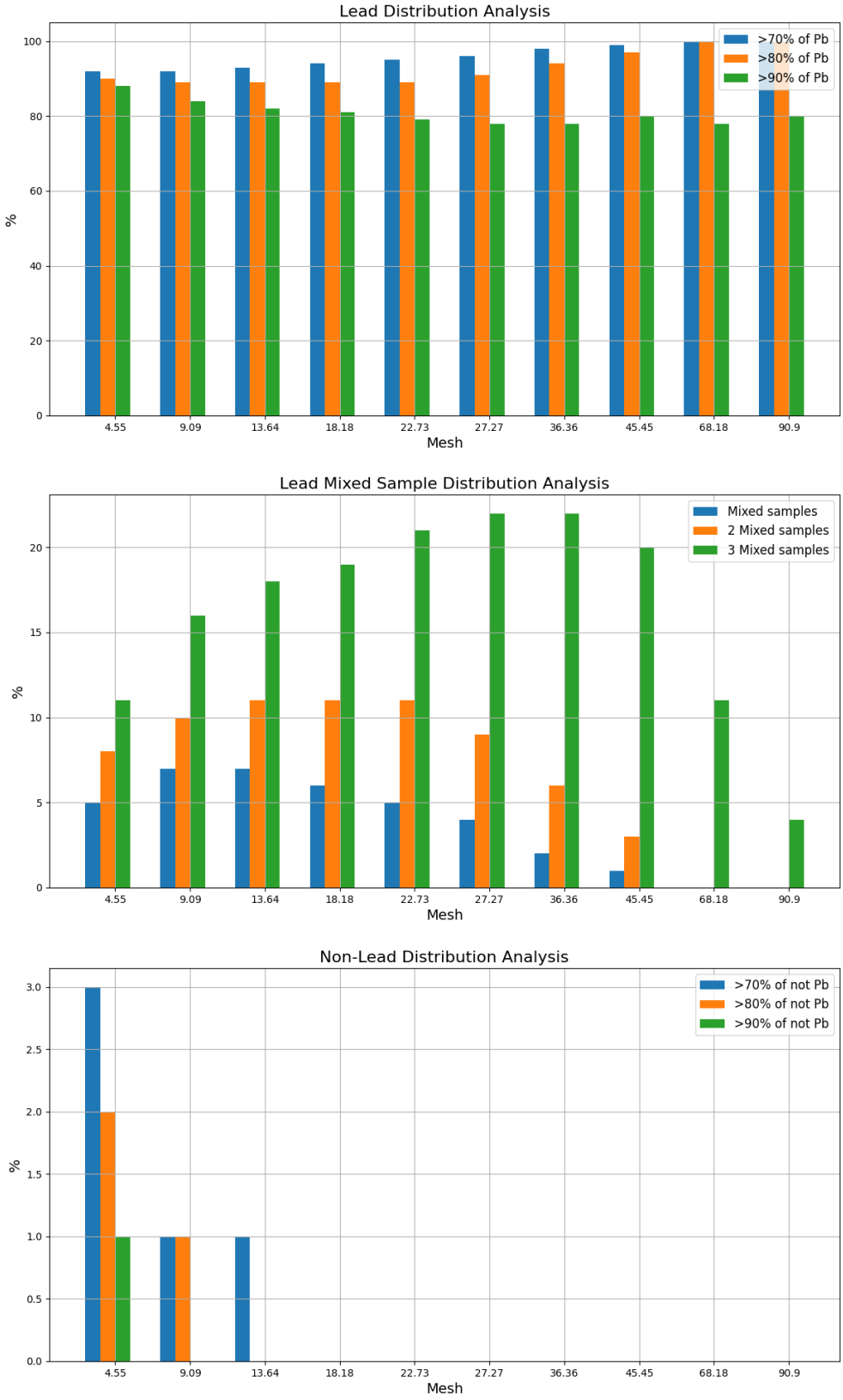

Graphic 4.13 – Particles of lead, non-lead (matrix) and mixed distribution across different mesh in simulated image with statistics of sample #1.

The sample #1 consistently demonstrates a remarkably high concentration of lead minerals (Pb), with values above 90%. With a particle size of 4.55 µm, an impressive 92% of the grains contain over 70% lead. This trend persists as the mesh size increases, highlighting the uniformity of lead content across the mesh size range.

In contrast, the numbers show that the fraction of mixed grains within the categories of samples with more than 70%, 80%, and 90% lead particles is lower, on the order of 10% or less. For example, with a mesh size of 4.55 µm, only 5% of the grains with over 70% lead particles are mixed. This proportion of mixed samples slightly increases with larger mesh sizes, indicating an increase in mineral diversity within the grain, as seen in all tested situations.

This analysis extends to higher lead content thresholds, where, for instance, with a mesh size of 4.55 µm, 90% of the grains contain over 80% lead particles, emphasizing the exceptionally high concentration of lead in these samples. This high percentage persists for all grain sizes.

The same trend continues for the 90% lead particle content threshold, where, for a grain size of 4.55 µm, 88% of the grains exceed this limit. The proportion of mixed samples varies slightly with mesh size, implying the existence of mineral mixtures even in samples with extremely high lead content.

4.3.2.2 Sample #2, MCu

In Figure 4.14, an example is provided of a plane from the simulated cube, where red cells represent lead (Pb) minerals and the blue background represents the matrix with other minerals. Table 4.7 displays the fraction of lead mineral grains, mixed grains, and non-lead grains for the three mentioned cut-off values. Cube simulation is conditioned to statistics of lead of the sample #2. The fraction of red cells is around 65,50%.

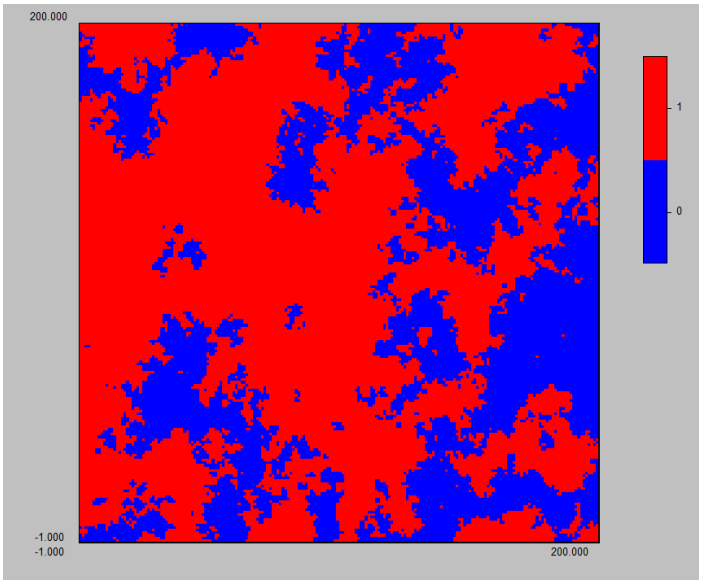

Figure 4.14 – Example of a simulated image on a random plane of the 3D simulated cube depicting lead mineral grains, conditioned to the statistics of sample #2.

Table 4.7 – Probabilities of encountering lead grains in simulated images with statistics of sample #2 across different mesh's

Grain size in µm	Frequency of grains with at least 70%, 80% or 90% of particles of Pb, matrix, or mixed								
	70%			80%			90%		
	Pb	mixed	not Pb	Pb	Pb	not Pb	Pb	mixed	not Pb
4.545	55%	22%	23%	49%	34%	18%	40%	48%	11%
9.09	53%	31%	16%	43%	47%	10%	31%	65%	4%
13.635	52%	37%	12%	39%	55%	6%	24%	74%	2%
18.18	51%	41%	7%	36%	62%	3%	19%	81%	1%
22.725	51%	44%	5%	33%	66%	1%	15%	85%	0%
27.27	51%	46%	3%	30%	69%	1%	10%	90%	0%
36.36	53%	46%	1%	25%	75%	0%	4%	96%	0%
45.45	55%	45%	0%	18%	82%	0%	1%	99%	0%
68.175	62%	38%	0%	2%	98%	0%	0%	100%	0%
90.9	67%	33%	0%	0%	100%	0%	0%	100%	0%

Again, the sample #2 consistently display a remarkably high concentration of lead minerals (Pb), with values above 65%, not so high of the previous sample. With a particle size of 4.55 µm, an impressive 55%, 49% and 40% of the grains contain over 70%, 80% and 90% of lead, respectively. As the mesh size increases, for 70% threshold quality the percentage of lead grains increases slightly, but for thresholds 80% and 90% decreases to zero, and grains are converted to mixed grains. This is due the percentage of lead present, around 65% and this mean amount interacts with the threshold results.

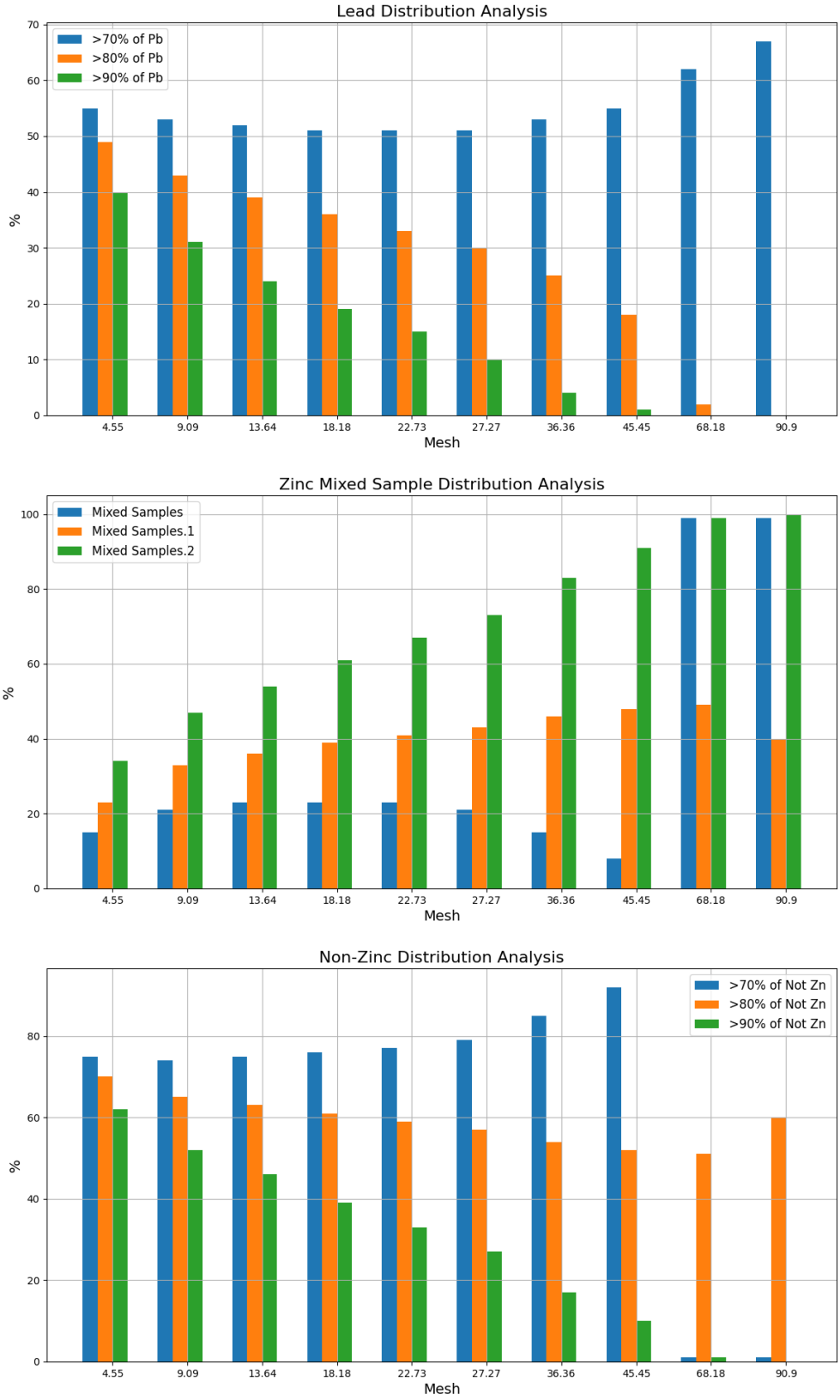

Graphic 4.14 – Particles of lead, non-lead (matrix) and mixed distribution across different mesh in simulated image with statistics of sample #2.

4.3.2.3 Sample #3, MCu

In Figure 4.15, an example is provided of a plane from the simulated cube, where coloured cells have the same meaning of the previous analysis. Again, table 4.8 displays the fraction of lead mineral grains, mixed grains, and non-lead grains for the three mentioned cut-off values. Cube simulation is conditioned to statistics of lead of the sample #3 around 77.53% of red cells.

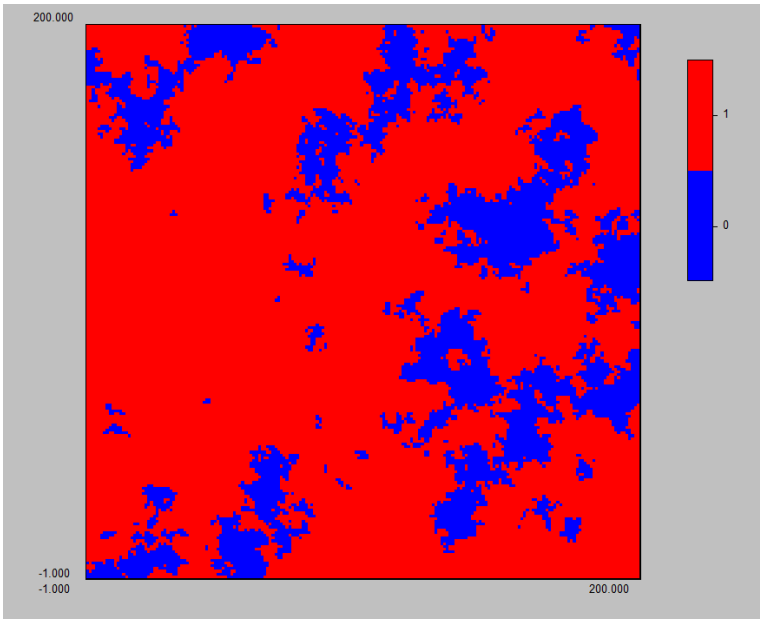

Figure 4.15 – Example of a simulated image on a random plane of the 3D simulated cube depicting lead mineral grains, conditioned to the statistics of sample #3.

Table 4.8 – Probabilities of encountering lead grains in simulated images with statistics of sample #3 across different mesh's

Grain size in µm	Frequency of grains with at least 70%, 80% or 90% of particles of Pb, matrix, or mixed								
	70%			80%			90%		
	Pb	mixed	Pb	Pb	Pb	not Pb	Pb	mixed	Pb
4.545	71%	17%	12%	65%	27%	9%	56%	39%	5%
9.09	70%	23%	7%	60%	36%	4%	47%	52%	1%
13.635	70%	26%	4%	57%	41%	2%	40%	59%	0%
18.18	71%	27%	2%	55%	45%	0%	34%	66%	0%
22.725	72%	27%	1%	54%	46%	0%	29%	71%	0%
27.27	75%	25%	0%	53%	47%	0%	24%	76%	0%
36.36	80%	20%	0%	51%	49%	0%	15%	85%	0%
45.45	86%	14%	0%	52%	48%	0%	8%	92%	0%
68.175	96%	4%	0%	47%	53%	0%	0%	100%	0%
90.9	100%	0%	0%	40%	60%	0%	0%	100%	0%

Finally, the simulation of lead particles with statistics of sample #3 consistently display a remarkably high concentration of lead minerals (Pb), with values above 77%. The behaviour of results are simulat to the previous ones, with a particle size of 4.55 µm, an impressive 71%, 65% and 56% of the grains contain over 70%, 80% and 90% of lead, respectively. As the mesh size increases, for 70% threshold quality the percentage of lead grains increases to 100% (because 70% is below the average of lead). For the remaining thresholds frequencies of the grains decreases, and the level of decreasing is high for the 90% threshold as expected.

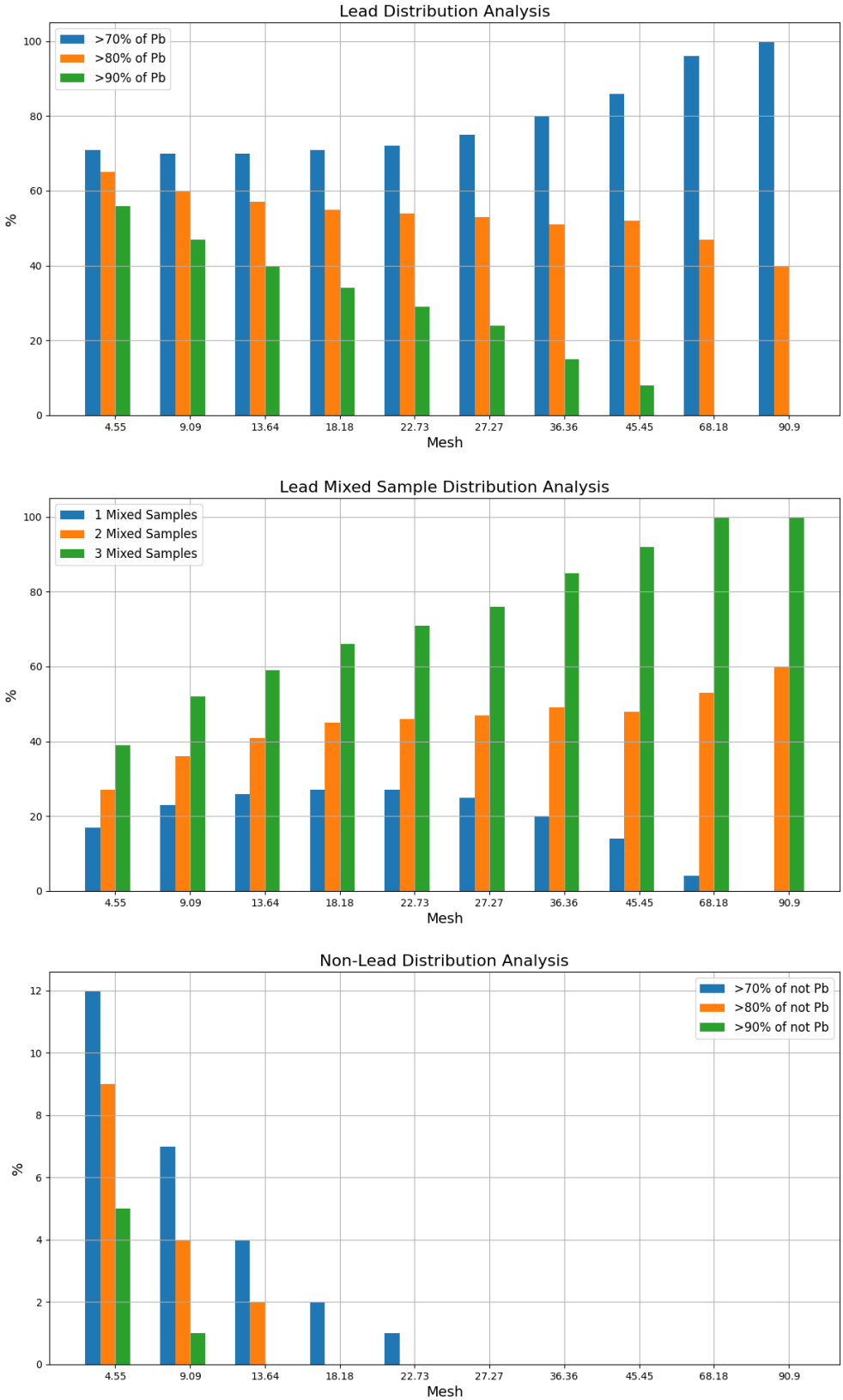

Graphic 4.15 – Particles of lead, non-lead (matrix) and mixed distribution across different mesh in simulated image with statistics of sample #3.

4.3.2.4 Discussion

All three samples, designated as samples #1, #2, and #3, show high Pb concentrations in average and this amount interfere with the threshold of quality. In fact, is possible that the higher frequency of Pb grains is due to a lower grade threshold used in the analysis. Sample demonstrates the highest lead content across all mesh sizes, with 100% lead content at the largest mesh size (90.9). Sample 2 has less lead compared to sample 1, and sample 3 shares similar lead concentration characteristics with sample 1.

The high amount of lead particles (95%, 65% and 77%) interfere with the threshold percentage quality and the partition between pure grains and mixed grains, as displayed before. Due to a very high amount of lead particles, sample #1 maintains a low proportion of mixed samples, ranging from 1% to 11%, with a decreasing trend as mesh size increases. Sample #2 has a higher proportion of mixed samples compared to sample #1, ranging from 4% to 38%, with an increasing trend as mesh size becomes coarser. Sample #3 falls between sample #1 and sample #2 as mixed samples, with proportions ranging from 1% to 27%, also decreasing with larger mesh sizes. In excluding non-lead minerals, all three samples become more efficient as mesh size becomes smaller.

4.3.3 Simulation of Zinc Particles

4.3.3.1 Sample #1, MZn

In Figure 4.16, an example is provided of a plane from the simulated cube, where coloured cells have the same meaning of the previous analysis. Again, table 4.9 displays the fraction of zinc mineral grains, mixed grains, and non-zinc grains for the three mentioned cut-off values. Cube simulation is conditioned to statistics of zinc of the sample #1 around 18.65% of red cells.

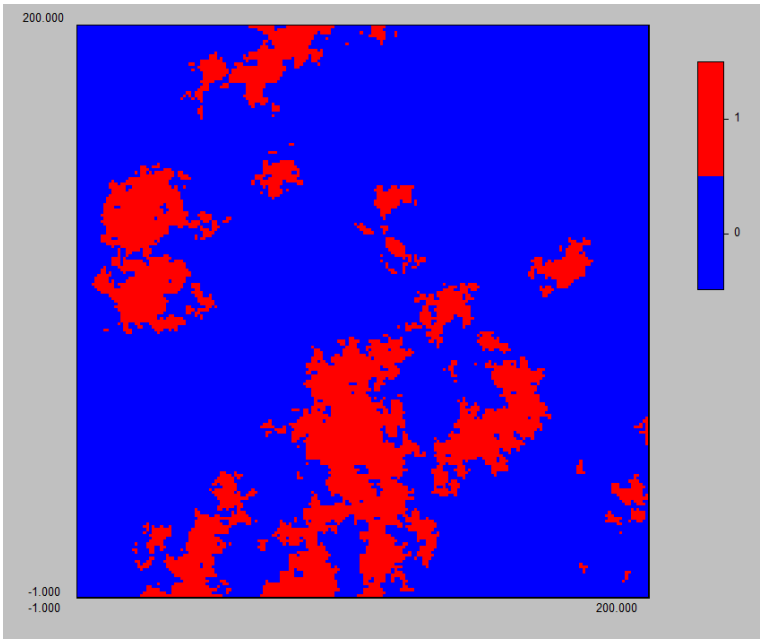

Figure 4.16 – Example of a simulated image on a random plane of the 3D simulated cube depicting zinc mineral grains, conditioned to the statistics of sample #1.

Table 4.9 – Probabilities of encountering zinc grains in simulated images with statistics of sample #1 across different mesh's

Grain size in µm	Frequency of grains with at least 70%, 80% or 90% of particles of Pb, matrix, or mixed								
	70%			80%			90%		
	Zn	mixed	Not Zn	Zn	mixed	Not Zn	Zn	mixed	Not Zn
4.545	10%	15%	75%	7%	23%	70%	4%	34%	62%
9.09	5%	21%	74%	2%	33%	65%	1%	47%	52%
13.635	2%	23%	75%	1%	36%	63%	0%	54%	46%
18.18	1%	23%	76%	0%	39%	61%	0%	61%	39%
22.725	0%	23%	77%	0%	41%	59%	0%	67%	33%
27.27	0%	21%	79%	0%	43%	57%	0%	73%	27%
36.36	0%	15%	85%	0%	46%	54%	0%	83%	17%
45.45	0%	8%	92%	0%	48%	52%	0%	91%	10%
68.175	0%	1%	99%	0%	49%	51%	0%	99%	1%
90.9	0%	1%	99%	0%	40%	60%	0%	100%	0%

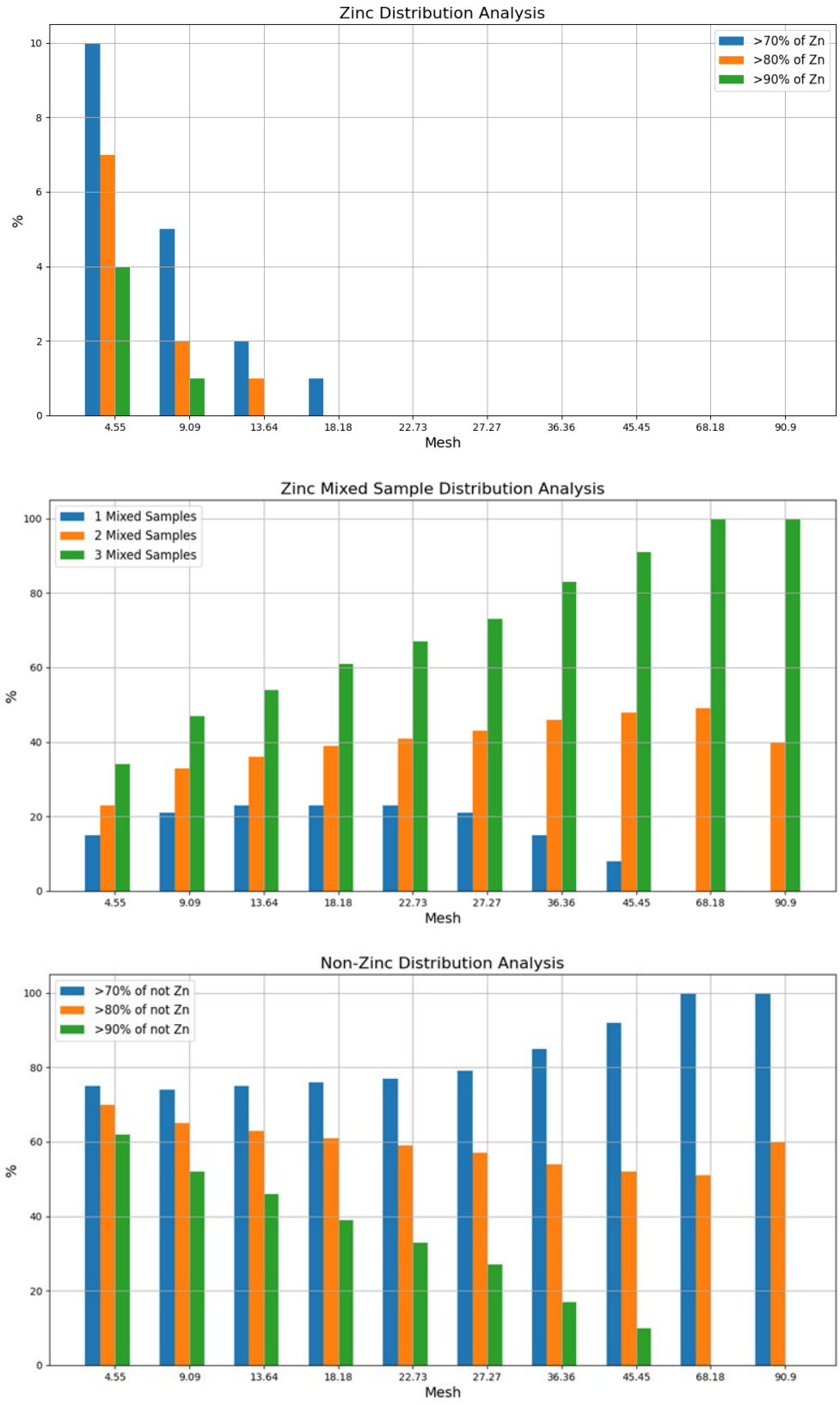

Graphic 4.16 – Particles of zinc, non-zinc (matrix) and mixed distribution across different mesh in simulated image with statistics of sample #1.

The sample #1 consistently demonstrates a low concentration of zinc minerals (Zn), with values below 20%. With a particle size of 4.55 μm, only 10% of the grains contain over 70% lead, and 4% if the percentage increases to 90%. Due to the low percentage of zinc minerals and their grain sizes, when the grain size increases, the estimated recovery decreases very quickly.

In contrast, the numbers show that the fraction of mixed grains within the categories of samples with more than 70%, 80%, and 90% zinc particles is low for small grains, but it increases quickly when the grain size increases. Also, the proportion of non-zinc grains is medium-high for small grain sizes and as grain size increases then they are transferred to mix grains.

4.3.3.2 Sample #2, MCu

In Figure 4.17, an example is provided of a plane from the simulated cube, where coloured cells have the same meaning of the previous analysis. Again, table 4.10 displays the fraction of zinc mineral grains, mixed grains, and non-zinc grains for the three mentioned cut-off values. Cube simulation is conditioned to statistics of zinc of the sample #2 around 12.21% of red cells.

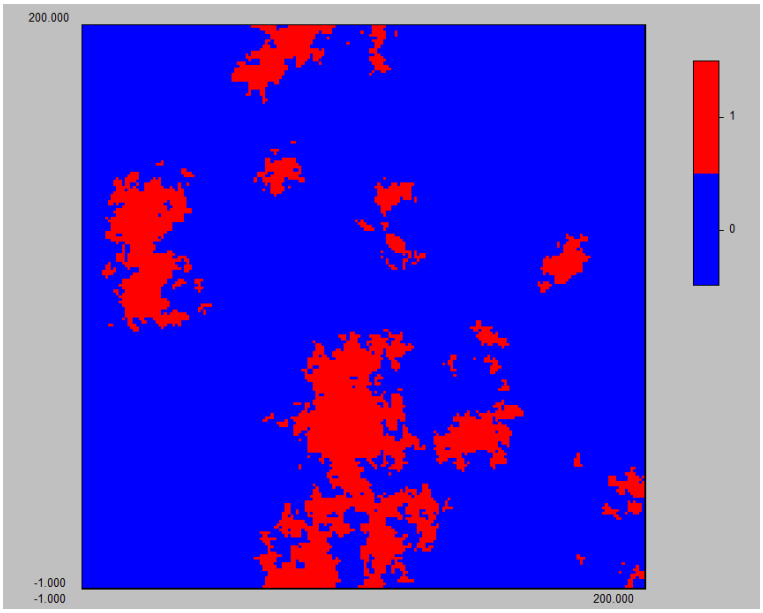

Figure 4.17 – Example of a simulated image on a random plane of the 3D simulated cube depicting zinc mineral grains, conditioned to the statistics of sample #2.

Table 4.10 – Probabilities of encountering zinc grains in simulated images with statistics of sample #2 across different mesh's

Grain size in µm	Frequency of grains with at least 70%, 80% or 90% of particles of Zn, matrix, or mixed								
	70%			80%			90%		
	Zn	mixed	not Zn	Zn	mixed	not Zn	Zn	mixed	not Zn
4.545	6%	11%	83%	4%	17%	79%	2%	24%	74%
9.09	3%	14%	84%	1%	22%	77%	0%	33%	67%
13.635	1%	14%	84%	0%	24%	76%	0%	37%	63%
18.18	0%	13%	86%	0%	24%	76%	0%	41%	59%
22.725	0%	12%	88%	0%	24%	76%	0%	45%	55%
27.27	0%	10%	90%	0%	23%	77%	0%	49%	51%
36.36	0%	4%	96%	0%	19%	81%	0%	56%	44%
45.45	0%	1%	99%	0%	13%	87%	0%	62%	38%
68.175	0%	0%	100%	0%	1%	99%	0%	73%	27%
90.9	0%	0%	100%	0%	0%	100%	0%	88%	12%

The behaviour of the sample #2, is very similar to the sample #1, and the percentage of zinc particles in sample #2 is around 12%, a lower value than sample #1. So, values in the column of more pure zinc grains are systematically lower than the previous sample and, for example, with a particle size of 4.55 µm, only 6% of the grains contain over 70% lead, and 2% if the percentage increases to 90%. Again, due to the low percentage of zinc minerals and their grain sizes, when the grain size increases, the estimated recovery decreases very quickly.

In contrast, the numbers show that the fraction of mixed grains within the categories of samples with more than 70% and 80% decreases, but for 90% increases. Also, the proportion of non-zinc grains is medium-high for small grain sizes and as grain size increases then they are transferred to mix grains in the 90% of purity.

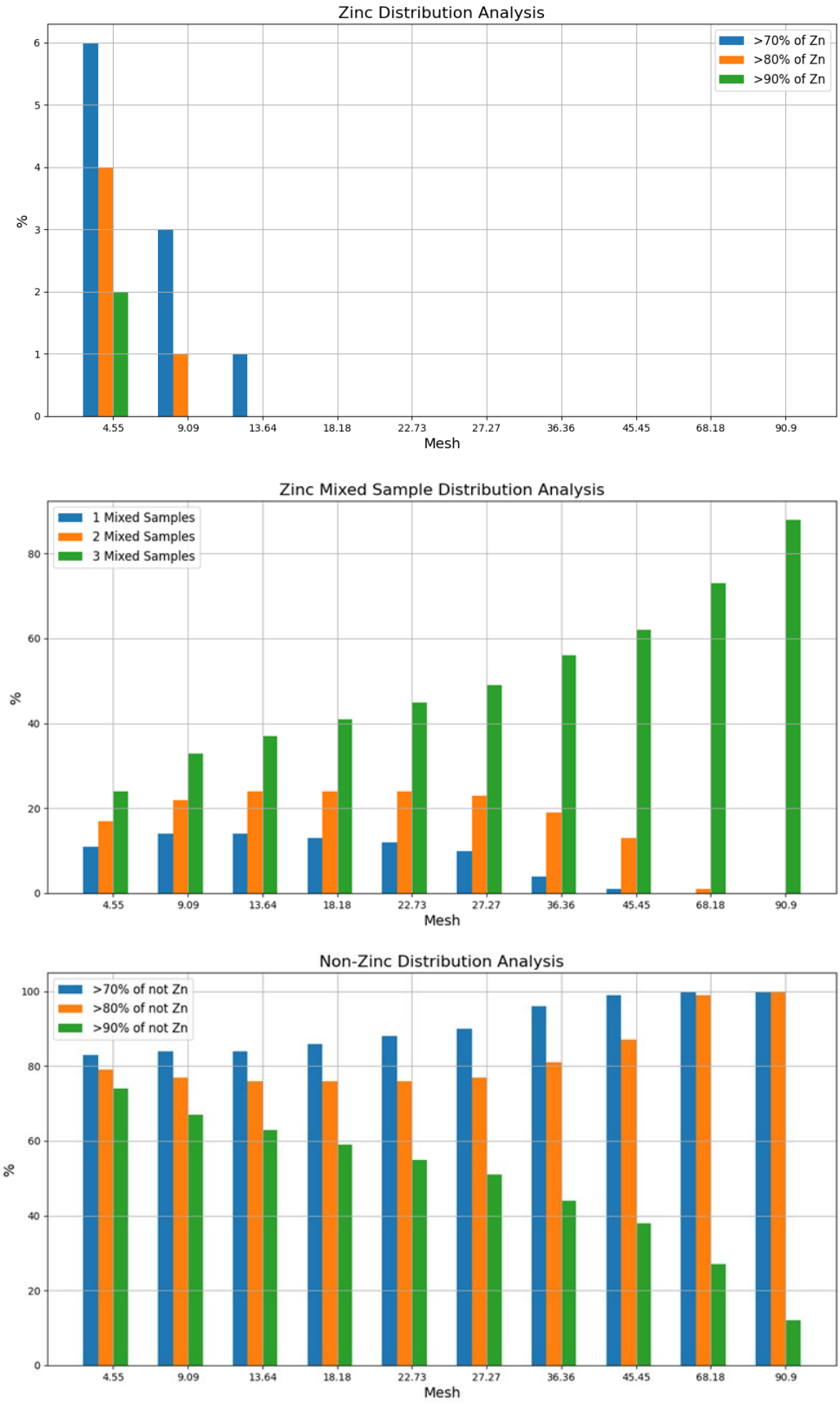

Graphic 4.17 – Particles of zinc, non-zinc (matrix) and mixed distribution across different mesh in simulated image with statistics of sample #2.

4.3.3.3 Sample #3, MCu

In Figure 4.18, an example is provided of a plane from the simulated cube, where coloured cells have the same meaning of the previous analysis. Once more, table 4.11 displays the fraction of zinc mineral grains, mixed grains, and non-zinc grains for the three mentioned cut-off values. Cube simulation is conditioned to statistics of zinc of the sample #3 around 21.91% of red cells.

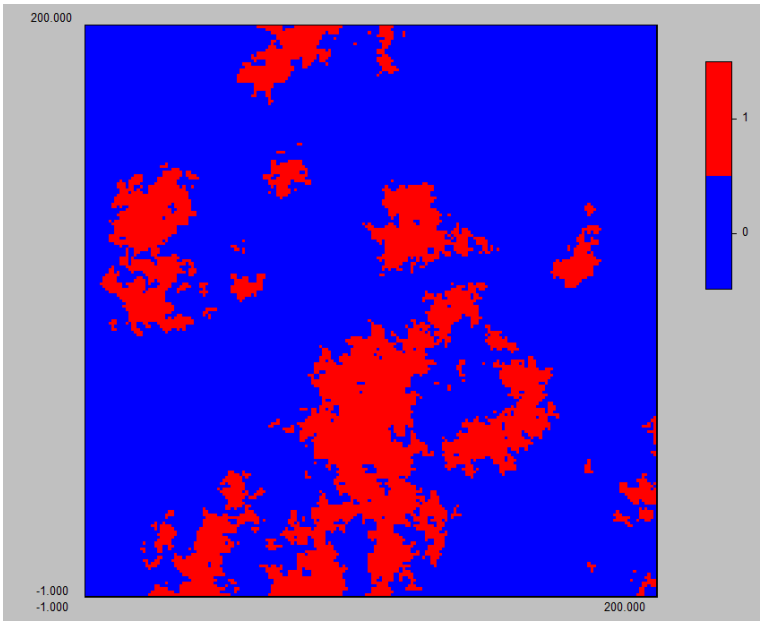

Figure 4.18 – Example of a simulated image on a random plane of the 3D simulated cube depicting zinc mineral grains, conditioned to the statistics of sample #3.

Table 4.11 – Probabilities of encountering zinc grains in simulated images with statistics of sample #3 across different mesh's

Grain size in µm	Frequency of grains with at least 70%, 80% or 90% of particles of Zn, matrix, or mixed								
	70%			80%			90%		
	Zn	mixed	not Zn	Zn	mixed	not Zn	Zn	mixed	not Zn
4.545	12%	18%	70%	8%	27%	64%	5%	40%	56%
9.09	7%	25%	69%	3%	38%	59%	1%	53%	46%
13.635	4%	28%	68%	1%	44%	55%	0%	62%	38%
18.18	1%	30%	68%	0%	48%	52%	0%	69%	31%
22.725	0%	31%	69%	0%	51%	49%	0%	76%	24%
27.27	0%	30%	70%	0%	54%	46%	0%	82%	18%
36.36	0%	26%	74%	0%	60%	40%	0%	92%	8%
45.45	0%	17%	83%	0%	66%	34%	0%	98%	2%
68.175	0%	2%	98%	0%	81%	19%	0%	100%	0%
90.9	0%	0%	100%	0%	96%	4%	0%	100%	0%

Finally, the behaviour of the sample #3, is very similar to the samples #1 and #2, and the percentage of zinc particles in sample #3 is around 22% close to the amount of sample #1. There are not much more to explain, values in the column of more pure zinc grains are decreasing abruptly, from 12% to zero increasing the particle size from 4.55 µm to 22.725 µm for the threshold of 70%, and the values are proportionally lower for higher thresholds.

Similarly, the numbers show that the fraction of mixed grains within the categories of samples with more than 70% and 80% decreases, but for 90% of threshold increases. Also, the proportion of non-zinc grains is medium-high for small grain sizes and as grain size increases then they are transferred to mix grains in the 90% of purity.

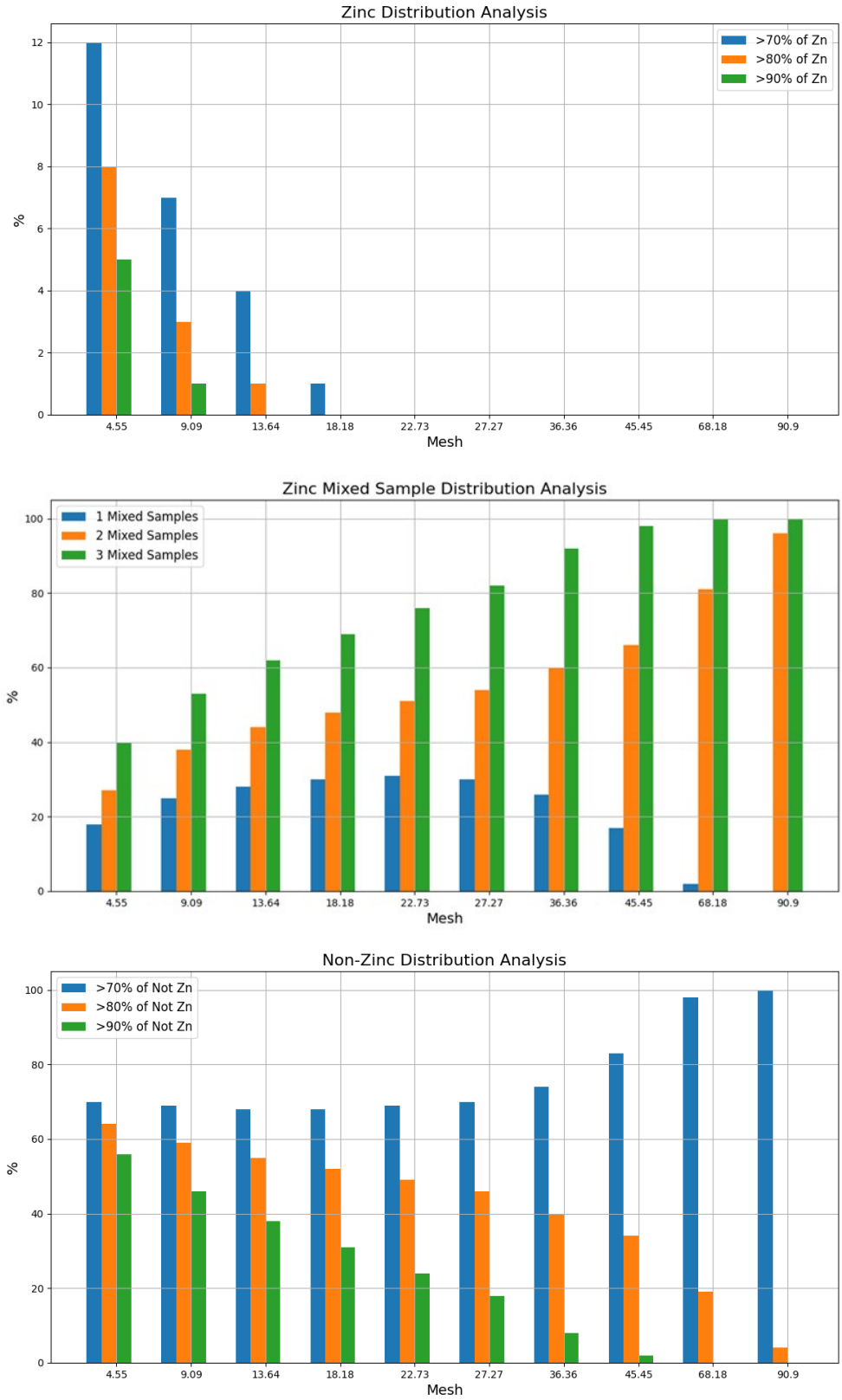

Graphic 4.18 – Particles of zinc, non-zinc (matrix) and mixed distribution across different mesh in simulated image with statistics of sample #3.

4.3.3.4 Discussion

The analysis of zinc (Zn) particles in the three studied samples and varying mesh sizes in the three samples reveals important insights. Sample #1 consistently exhibited the highest Zn content across all mesh sizes, showcasing its efficiency in retaining Zn material even at larger mesh sizes, which is consistent with the category. In contrast, sample #2 and sample #3, while still demonstrating a similar trend of decreasing Zn content with increasing mesh size, showed lower Zn concentrations compared to sample #1. This suggests again that smaller mesh sizes are more effective to retaining more pure particles of Zn.

The presence of mixed samples, indicative of impurities and the coexistence of minerals alongside Zn-rich ones, varied among the three samples. Sample #1 maintained a relatively low proportion of mixed samples, indicating its potential for producing purer Zn material. In contrast, sample #2 displayed a higher proportion of mixed samples, emphasizing the importance of milling more to separate impurities effectively. Sample #3, positioned between sample #1 and sample #2 in terms of mixed samples, suggests a middle ground in impurity levels.

The analysis of non-Zn minerals across varying mesh sizes underscores the effectiveness of coarser mesh sizes in eliminating impurities and maximizing Zn content. At the largest mesh size (90.9), none of the grains in sample #1, sample #2 and sample #3 contains less than 100% of Zn. Ultimately, the choice of mesh size can impact the quality and purity of Zn products, with smaller mesh sizes proving advantageous in retaining Zn content and minimizing impurities.

4.4 Summary of the Results Towards Optimization of Froth Flotation

During this study, an empirical behaviour was observed, where a smaller particle size is associated with greater mineral liberation. This phenomenon was consistently observed in all samples for the metals copper and zinc; however, for lead, this evidence was not confirmed, as it is the most abundant element in the ore. Given the practical limitations imposed by the lower size limit of particles set by foam flotation equipment and the associated costs of excessive comminution, achieving finer particle sizes becomes a significant disadvantage.

To summarize the previous results, in the following Graphics 4.19 to 4.21 it is illustrated the frequency of monomineral grains of copper, lead and zinc for samples #1, #2 and #3.

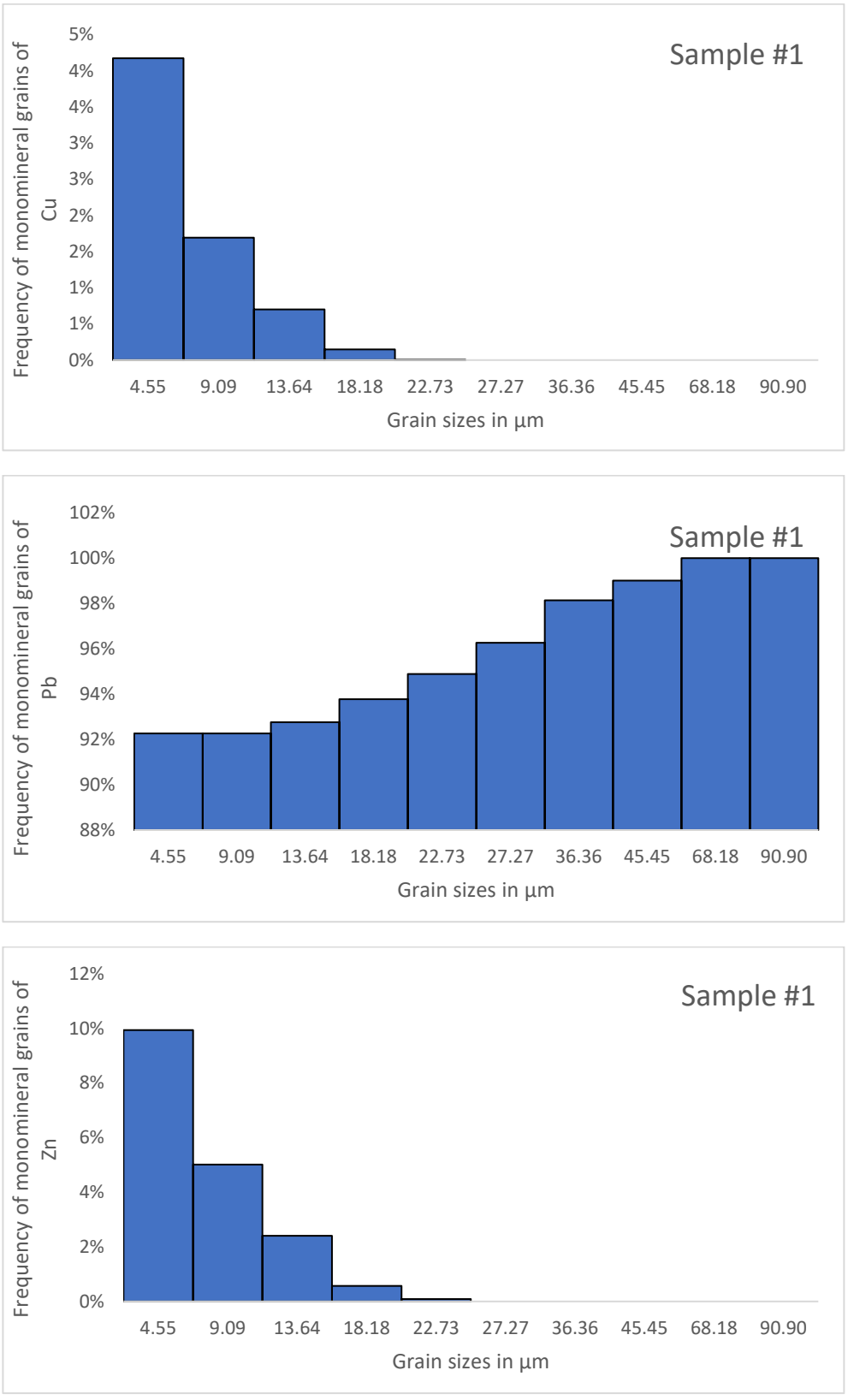

Graphic 4.19 – Fragmentation rate vs frequency of monomineral particles of copper, lead and zinc minerals in sample #1

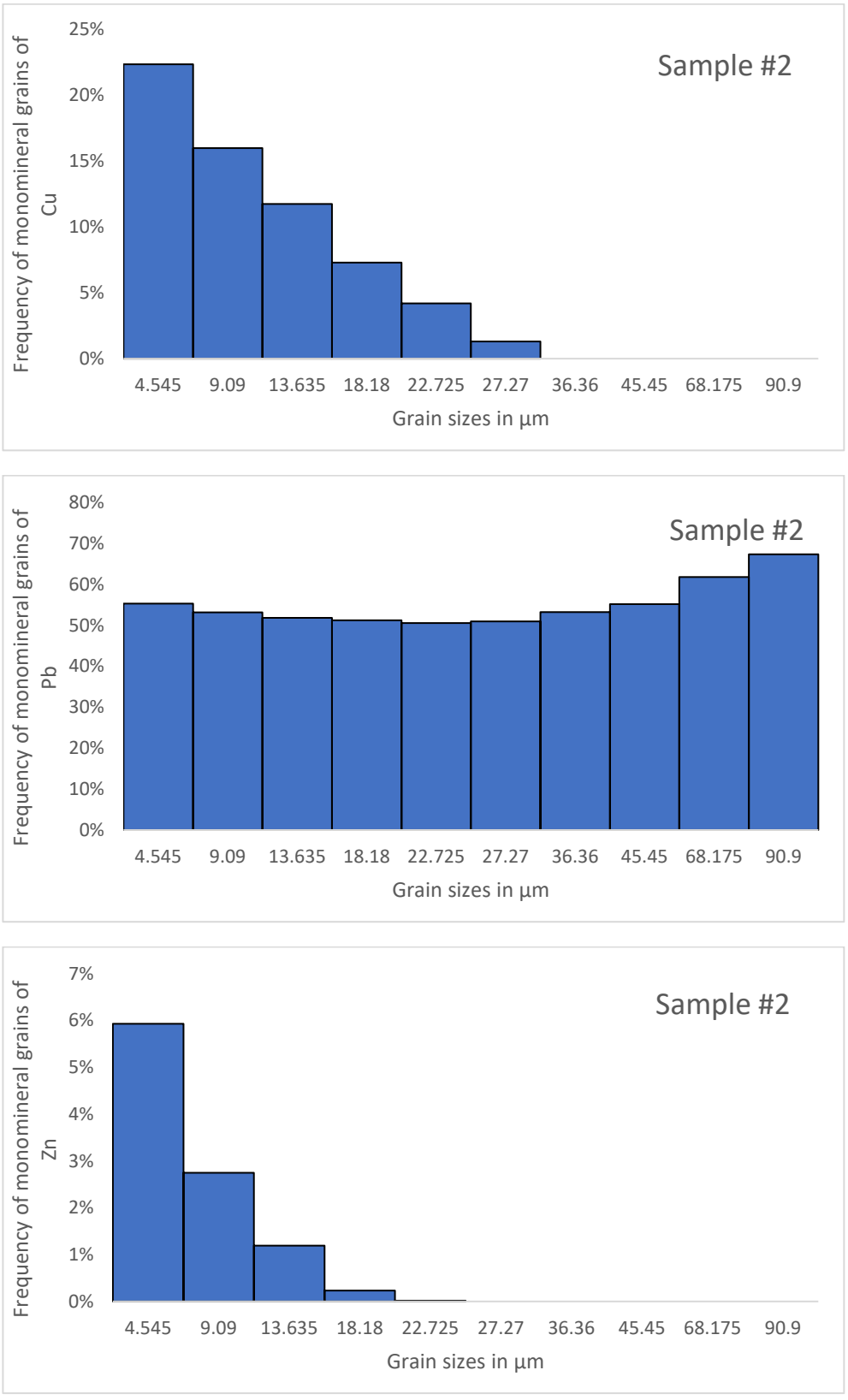

Graphic 4.20 – Fragmentation rate vs frequency of monomineral particles of copper, lead and zinc minerals in sample #2

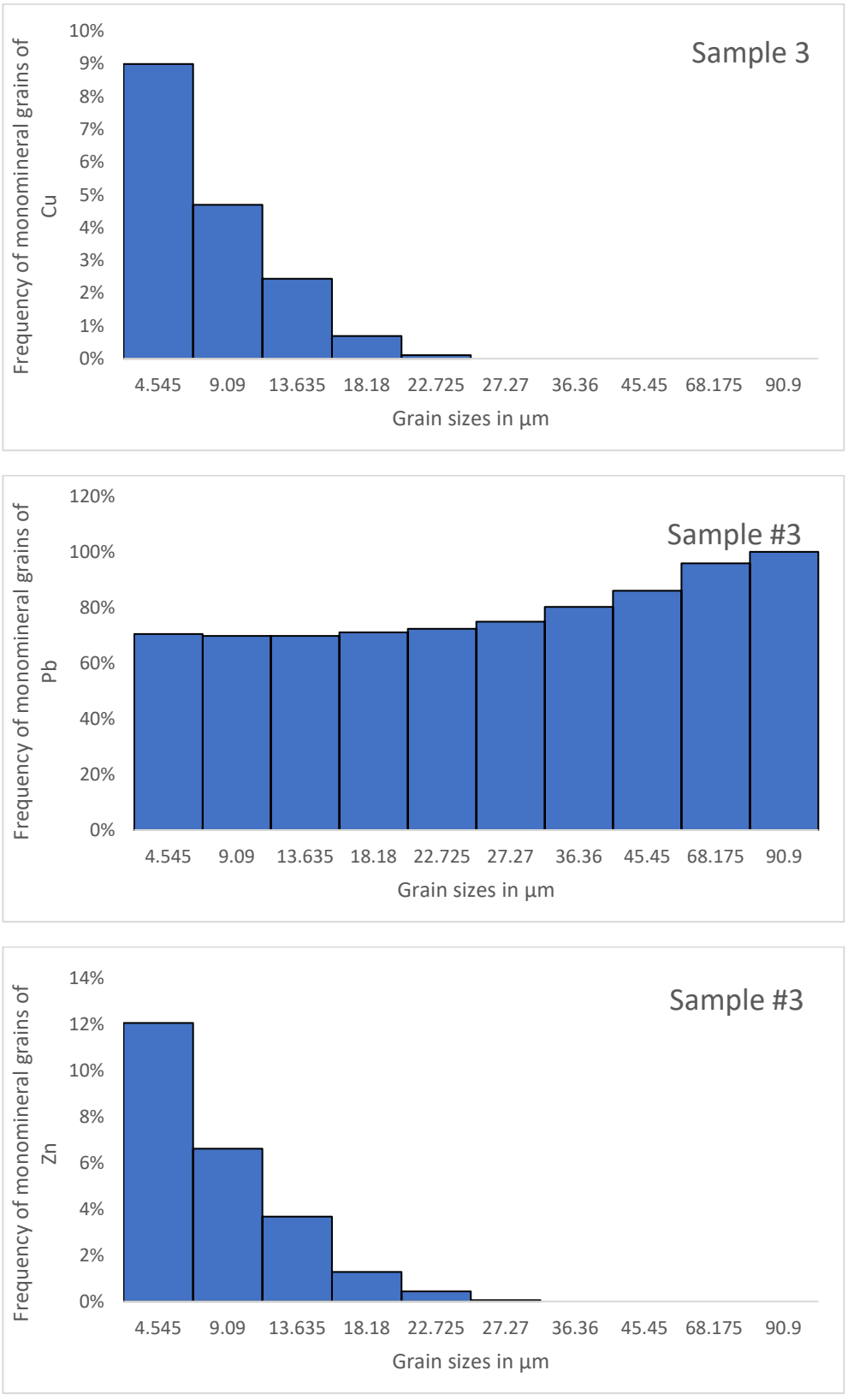

Graphic 4.21 – Fragmentation rate vs frequency of monomineral particles of copper, lead and zinc minerals in sample #3

The issue addressed in this dissertation is a complex problem involving three closely related key variables: purity rate in mineralogical terms, degree of comminution, and metal recovery rate. Given the intricate nature of this problem, a practical approach was adopted by simulating the indicator to characterize this process. One of these variables, the purity rate, was intentionally fixed at three different values (70%, 80%, and 90%) to evaluate its impact. This approach served as an initial step in this comprehensive investigation, establishing the foundation for a more in-depth exploration of this multifaceted issue. By fixing one variable at a time while varying the other two, we sought to gain insights into the interaction of these factors in two dimensions and explain their implications for mineral separation processes.

This situation requires the consideration of mixed grains, as it becomes imperative to accept certain levels of impurities to enhance the recovery of valuable materials, especially due to the low particle size thresholds for monomineral components such as copper and zinc.

Based on the available data, a grain size of 13.64 µm seems to ensure a favourable balance between monomineral grains and mixed grains, especially for copper and zinc metals and towards separation.

The particle size of 13.64 µm is suggested after a detailed analysis of Tables 4.3, 4.4, 4.5, 4.9, 4.10, and 4.11. In these tables, it became evident that this size offered the desired balance between monomineral grains and mixed grains. This conclusion is supported by the associated graphical representations, which, while not indicating the size with the highest propensity for monomineral content, clearly demonstrate that the lower presence of mixed grains contributes significantly to enhanced material recovery.

A lower rate of mixed grains can improve metal recovery rates due to their lower inherent heterogeneity. Notably, these mixed mineral compositions do not consist uniformly of a 50-50 distribution of valuable mineral and gangue components. Instead, their actual ratios can exhibit considerable variation, disadvantaging the increase in overall metal recovery.

Furthermore, even when classified as mixed grains, the composition of these grains often retains a substantial percentage of metals, remaining a significant reservoir of recoverable material.

This understanding highlights the intricate and multivariable nature of mineral separation. The distribution and composition of mixed grains are far from uniform, and these variations significantly influence the overall metal recovery rates. In the case of lead, as indicated in the tables related to lead, there is a notable consistency observed across various particle sizes. Therefore, with the currently available data, the need for meticulous particle size selection may not be as imperative as in the previous cases. However, it is important to emphasize that further studies are required to increase the level of confidence in these findings.

5 EIT- CHAPTER

5.1 Life Cycle & Circular Economy

Although this study did not conduct a comprehensive Life Cycle Assessment (LCA), it is essential to recognize the potential social and environmental benefits associated with optimizing ore milling and particle size distribution for copper, zinc, and lead ores extraction. One critical aspect that could be impacted across the life cycle is energy consumption during the milling and crushing processes. Further analysis through a complete LCA would provide more precise insights into these environmental and social implications.

This project plays a pivotal role in advancing resource efficiency within the mining industry, particularly concerning copper, zinc, and lead. The core strategy focuses on maximizing mineral recovery while minimizing waste generation. These efforts are in alignment with the principles of the circular economy, which emphasizes extending the life of valuable resources and reducing environmental impact. As such, the outcomes of this work hold the potential to significantly contribute to a more sustainable and circular approach to resource management, with a direct application to these three essential minerals.

The project's optimization of ore processing methods, specifically for copper, zinc, and lead, presents an opportunity to enhance the sustainability of raw materials. This enhancement arises from the efficient utilization of resources and the reduction in waste. By extending the useful life of these materials, the project aligns with the broader objective of ensuring the availability of critical raw materials for an extended duration. Furthermore, this increased sustainability can have far-reaching impacts on the broader supply chain for these minerals, reinforcing their availability for various industrial applications.

While this project doesn't directly engage with materials currently listed as "critical," it remains vital to maintain vigilance regarding the potential future criticality of resources, especially copper, zinc, and lead. This proactive approach is essential to ensure the resilience of supply chains that rely on these minerals. As industrial needs and global dynamics evolve, monitoring for shifts in criticality is crucial to avoiding disruptions in the availability of these essential materials.

The implications of this work for the circular economy are highly significant. By significantly reducing waste generation, optimizing resource efficiency, and making efficient use of energy during the extraction of copper, zinc, and lead, the project stands to play a pivotal role in fostering a more sustainable and circular approach to mining these critical minerals. In effect, the project directly supports the circular economy's fundamental principles, promoting resource longevity and environmentally responsible practices in the mining industry, ultimately contributing to a more sustainable future (Critical Raw Materials, s.d.) (Sphera, s.d.) (Stephen J. Bigelow, s.d.).

5.2 Techno-Economic Analysis & Business Potential

A comprehensive Techno-Economic Analysis (TEA) of the ore milling and size distribution optimization process was beyond the scope of this research. Nevertheless, preliminary assessments suggest the potential for significant economic benefits. Further study would entail collecting data on operational costs, energy savings, and mineral recovery rates to conduct a thorough TEA.

The project holds substantial potential to stimulate innovative business activities within the mining sector. Optimizing ore processing methods, especially for copper, zinc, and lead, could lead to the development of advanced technologies and services aimed at improving the efficiency and sustainability of mineral extraction.

While a full business plan is beyond the scope of this academic research, a preliminary business model could involve offering consulting and technology solutions to mining companies looking to enhance their ore processing methods. This business model would focus on providing expert guidance, software solutions, and process optimization services to improve mineral recovery and reduce waste.

Initiating this new venture would involve collaborating with mining companies in regions with significant copper, zinc, and lead extraction operations. These regions would be ideal starting points due to their existing reliance on these minerals. Beginning here allows for easier integration of innovative processes and technologies. However, expansion into other mineral-rich regions could be considered based on demand and market opportunities.

5.3 SWOT Analysis

A SWAT analysis of this study is provided in the sext subsections (see Table 5.1).

5.3.1 Strengths

The project's innovative approach sets it apart by leveraging geostatistics and data analytics to optimize ore processing in the mining industry, demonstrating a commitment to data-driven solutions. It showcases resource efficiency by prioritizing the maximization of valuable mineral recovery, aligning with circular economy principles. Additionally, the focus on reducing the amount of material sent to tailings contributes to waste reduction and environmental sustainability. By improving the milling process efficiency, the project also lowers energy consumption, adhering to sustainable practices and reducing carbon emissions. Moreover, the project has the potential to make a positive social impact on local communities and stakeholders by reducing environmental impacts and promoting responsible resource management.

Table 5.1 – SWOT analysis

SWAT Analysis	
Strength	**Weaknesses**
Innovative approach Resource efficiency Waste reduction Energy savings Positive social impact	Data requirements Implementation complexity Initial costa
Opportunities	**Threats**
Market demand Partnership Government initiatives	Market competitors Market volatility Regulatory changes

5.3.2 Weaknesses

One potential challenge is the extensive data requirements for conducting geostatistical analyses and data-driven optimization, which may be difficult to obtain. Additionally, integrating new technology and processes into existing mining operations can be complex and may face resistance from well-established practices. Another drawback is the initial investment costs involved in implementing geostatistics and data analytics tools, which could serve as a barrier for some mining companies looking to adopt these innovations.

5.3.3 Opportunities

The project is well-positioned to capitalize on the growing market demand for sustainable mining practices and resource efficiency. It can attract clients seeking to improve their environmental performance by offering innovative solutions. Furthermore, forming strategic partnerships with technology providers, equipment manufacturers, and sustainability consultants can enhance the project's service offerings and create new business opportunities. The project can also align with government initiatives promoting sustainable mining practices to access potential funding and gain recognition in the market.

5.3.4 Threats

Competition from other companies offering similar optimization services poses a potential threat. The mining industry's susceptibility to fluctuations in commodity prices and market demand can impact the willingness of potential clients to invest in optimization services, making market volatility a concern.

Additionally, changes in environmental regulations or permitting requirements can affect the feasibility of certain mining projects, potentially reducing the demand for optimization services. It's crucial to navigate these threats while leveraging the project's strengths and opportunities to succeed in the market (Stephen J. Bigelow, s.d.) (parabol, s.d.).

6 CONCLUSIONS

The 3D simulation of the spatial arrangement pattern of the particles of the main minerals that are the source of the metals copper, zinc, and lead highlights the significant importance of mesh size selection in the separation and recovery of minerals in an ore concentration unit. The results of this study consistently demonstrate that smaller grain sizes (finer comminution), especially in the range of 13.64 µm, are effective in separating particles of copper and zinc minerals. However, for lead mineral particles, given their high frequency, such separation would not require such a low dimension.

A possible explanation for the abnormally high quantity of lead particles is that the samples may originate from a lead-rich zone and may not be representative of a specific deposit. However, it is crucial to emphasize that this is only a preliminary hypothesis, and confirming this assertion requires further investigation. Therefore, additional studies are needed to verify whether this assumption is indeed substantiated, particularly regarding the representativeness of the samples.

An important observation in all samples is the prevalence of fine-grained minerals in the spatial arrangement of the mineral puzzle, justifying further investigation into the mineral associations present. These patterns confirm the hypothesis that finer mesh sizes result in higher recovery rates, offering valuable insights for geological interpretation and exploration planning.

The analysis of the abundance of mixed grains demonstrates the methodology's effectiveness in areas with substantial copper and zinc content. However, it is essential to recognize that the methodology's performance may vary depending on mineral composition, sample characteristics, and research objectives. In samples with more sparsely distributed and/or low-concentration minerals, the precision of this methodology will be lower. Therefore, researchers should carefully assess the suitability of this approach, considering the material characteristics and research goals.

A noteworthy observation arises from the comparative analysis of copper concentrations in sample #1 and zinc concentrations in sample #2, suggesting potential correlations or geological factors influencing their distribution. This evidence raises further questions about the interaction of these elements in geological processes, opening avenues for future investigations.

Finally, the analysis of mixed grains in sample #3 introduces a new dimension to the study. Unlike samples #1 and #2, this fraction exhibits a random mixture of minerals, deviating from previous patterns of uniformity and predictability. This finding highlights the complexity of mineral associations and distribution patterns within different samples, encouraging further research to unravel the underlying factors.

In summary, the study's results provide valuable insights into mesh size selection for more efficient mineral recovery, the influence of fine-grained materials, and the varied behaviours of elements in

different sample compositions. Additional research in this field has the potential to uncover additional nuances and correlations in mineral distribution, enriching our knowledge of geological phenomena.

7 FUTURE RECOMMENDATIONS

One must acknowledge some inherent limitations in this study. During the variogram calculation and adjustment process, it is noteworthy that the methodology employed required manual variogram modelling through graphic iterations. This approach, though common, introduces the possibility of parallax errors due to the subjectivity inherent in manual adjustments. In future studies of this nature, it is advisable to explore and implement more automated methods for variogram modelling, especially considering variograms calculated on images with a high density of steps. Utilizing automated techniques can help mitigate the influence of human subjectivity, resulting in more precise and reproducible variograms.

Another limitation was the similarity of range values, specially for the first structure, determined among the samples, which is attributed to the use of a set of samples with very similar characteristics. It is therefore advisable to extend the study to more diverse samples. This approach would allow for a more comprehensive exploration of the relationships and nuances between amplitudes and copper content thresholds, facilitating a more robust geostatistical analysis.

To gain a comprehensive understanding of grain distribution and spatial relationships among mineral particles within a sample, it is recommended to conduct a cross-analysis of the various metals present to elucidate the spatial interaction among these diverse elements and minerals.

The analysis of mixed grains, especially regarding lead mineral particles, has highlighted limitations in effectively predicting correlations and spatial patterns. The current approach falls short of capturing the complexities of mixed samples, emphasizing the need for methodological improvements. These improvements may involve advanced spatial analysis techniques, more detailed sampling, geological modelling, and cross-referencing with other elements. Enhancing the analysis of mixed samples is essential to gain a comprehensive understanding of element distribution within these intricate geological contexts, crucial for geological exploration and resource management.

A concrete improvement would be the implementation of co-kriging or multivariate geostatistics. These methods consider complex interactions and spatial dependencies among multiple elements in mixed samples. By considering the co-occurrence patterns of mineral particles, it becomes possible to develop more accurate predictive models for mixed samples, enhancing our ability to understand and manage the distribution of elements in challenging geological contexts.

While the observed similarity between zinc and copper concentrations in samples #1 and #2 is intriguing, it is essential to exercise caution in drawing definitive conclusions. Further studies are imperative to determine the nature and significance of this similarity. These studies should explore potential geological and mineralogical mechanisms that could explain the observed pattern. Additionally, statistical analyses

and geospatial investigations should be conducted to establish whether this phenomenon is a coincidental occurrence or indicative of a substantive relationship between copper and zinc distribution in the studied area.

Finally, a sensitivity analysis can provide valuable insights for future recommendations. By systematically varying key parameters and input data, this analysis assesses how changes in these factors influence the simulation results. Through this process, the study aims to identify which parameters have the most significant impact on mineral distribution patterns, concentration, and other critical outcomes. The findings from the sensitivity analysis will not only enhance the understanding of the simulation model but also guide informed recommendations for further research or practical applications in the field.

One practical recommendation arising from these findings is the possibility of conducting additional readings to further investigate the abundance of lead, eventually applying less sensitive threshold values. Repeating the readings can help determine whether the unusually high concentration of lead observed in the dataset is consistent or if it was an anomalous occurrence specific to a sample or even if it is due to higher sensitivity of the measuring equipment.

8 REFERENCES

Advameg. (n.d.). *Copper, Chemical Element – Overview, Discovery and naming, Physical properties, Chemical properties, Occurrence in nature, Isotopes*. Retrieved 10 6, 2023, from Chemistryexplained.com: http://www.chemistryexplained.com/elements/C-K/Copper.html

Alexandra Gomez Escobar, J. M. (2021, Semptember 14). Physical–Chemical Characterization of the Neves Corvo Extractive Mine Residues: A Perspective Towards Future Mining and Reprocessing of Sulfidic Tailings. *Journal of Sustainable Metallurgy*.

Almeida, J. (2018). *Geoestatística e tratamento de Dados.* Lisbon.

Copper allience. (2022, February 10). *Copper allience*. Retrieved from Copper allience: https://copperalliance.org/resource/copper-recycling/

Critical Raw Materials. (n.d.). Retrieved 10 14, 2023, from http://ec.europa.eu/growth/sectors/raw-materials/specific-interest/critical_en

Davuluri, P. (2015). *Quanta SEM for Materials Science*. Retrieved 10 6, 2023, from http://fei.com/products/sem/quanta-sem-for-materials-science

Davuluri, P. (2018). *An Introduction to Electron Microscopy - SEM*. Retrieved 10 6, 2023, from https://fei.com/introduction-to-electron-microscopy/stem

Diggle, P. J., & Giorgi, E. (2019). *Model-based Geostatistics for Global Public Health:Methods and Applications*. Retrieved 10 6, 2023, from https://taylorfrancis.com/books/9781315188492

electronicsforu. (2020, augost 13). *electronicsforu*. Retrieved from electronicsforu: https://www.electronicsforu.com/market-verticals/power-electronics/lithium-ion-batteries

electronicstakeback. (2008). *Electronic Waste (E-waste) Recycling Facts*. Retrieved 10 6, 2023, from electronicstakeback: http://www.electronicstakeback.com/resources/facts-and-figures/

Goovaerts, P. (2006). *Geostatistical Modeling of the Spaces of Local, Spatial, and Response Uncertainty for Continuous Petrophysical Properties*. Retrieved 10 6, 2023, from http://archives.datapages.com/data/specpubs/ca05/chapter06/images/chapter06.pdf

Goovaerts, P. (2006). Geostatistical Modeling of the Spaces of Local, Spatial, and Response Uncertainty for Continuous Petrophysical Properties. *AAPG Special Volumes*.

Hohn, M. E. (2000). Geostatistics and Petroleum Geology (2nd ed.). *Technometrics, 42*(4), 444-444. Retrieved 10 6, 2023, from https://tandfonline.com/doi/abs/10.1080/00401706.2000.10485747

Hustrulid, W. A. (2023). Retrieved from Britannica: https://www.britannica.com/technology/mining/Surface-mining

Hustrulid, W. A. (2023). *Concentration*. Retrieved from Britannica: https://www.britannica.com/technology/mineral-processing/Concentration

Hustrulid, W. A. (2023). *Underground Mining*. Retrieved from https://www.britannica.com/technology/mining/Underground-mining

Jam Making 101: The Tools and Techniques for Success. (n.d.). Retrieved 10 6, 2023, from http://www.seriouseats.com/2014/07/jam-making-101-tools-techniques.html

Jinchi Chu, W. X. (1994). 3-D Implementation of Geostatistical Analyses--The Amoco Case Study. In W. X. Jinchi Chu, *Stochastic Modeling and Geostatistics* . The American Association of Petroleum Geologists. .

Kanevski, M., Parkin, R., Pozdnukhov, A., Pozdnukhov, A., Timonin, V., Maignan, M., . . . Canu, S. (2004). Environmental data mining and modeling based on machine learning algorithms and geostatistics. *Environmental Modelling and Software, 19*(9), 845-855. Retrieved 10 6, 2023, from https://sciencedirect.com/science/article/pii/s1364815203002032

Kobylińska, K. (2016, December 20). *The Use of Indicator Kriging for Analyzing Prices in the Real Estate Market.*

Krzak, M. (2021). Is the EU's Resource Base of Copper Ore Deposits Large? A Fuzzy Set Theory Approach. *Resources* .

Langetepe, E. (2010). *On the optimality of spiral search*. Retrieved 10 6, 2023, from https://dl.acm.org/citation.cfm?id=1873602

lundinmining. (n.d.). *Neves-Corvo*. Retrieved 10 6, 2023, from https://docs.google.com/viewer?a=v&q=cache:RWvMwfdY0-YJ:www.lundinmining.com/i/pdf/Summary_Report_Neves-Corvo.pdf+silverstone+resources+portugal+life+of+mine&hl=en&gl=ca&pid=bl&srcid=ADGEESgbh95W-PUeIp-qeLE28CU0eypfp5WSJJIRU1Mx6-4H7MOLef-55q2oxGg5pS6b4JCR_CMgZ6tAd4qI_24cZl-IeJ4aoAuQ12p6hPNerWQqdTC83VNSO3EaXeV0gC9T4ydkm_en&sig=AHIEtbQCBJeLFHyAs8AeDxFY0AOmmtJ1qw

Monier, V., Hestin, M., Impériale, A.-C., Prat, L., Hobbs, G., Adams, K., . . . Ramos, M. (2017). *Resource Efficient Use of Mixed Wastes.* Deloitte.

Moura, A. (2008). Metallogenesis at the Neves Corvo VHMS deposit (Portugal): A contribution from the study of fluid inclusions. *Ore Geology Reviews, 34*(3), 354-368. Retrieved 10 6, 2023, from https://sciencedirect.com/science/article/pii/s0169136808000450

Moura, A. (2008). Metallogenesis at the Neves Corvo VHMS deposit (Portugal): A contribution from the study of fluid inclusions.

National Minerals Information Center. (2023, September). *Zinc Statistics and Information*. Retrieved from USGS: https://www.usgs.gov/centers/national-minerals-information-center/zinc-statistics-and-information

ODS. (2022, September 28). *Zinc – Fact Sheet for Health Professionals*. Retrieved 10 6, 2023, from Office of Dietary Supplements, US National Institutes of Health: https://ods.od.nih.gov/factsheets/Zinc-HealthProfessional

Olea, R. A. (1994). *Fundamentals of Semivariogram Estimation, Modeling, and Usage*. Retrieved 10 6, 2023, from http://archives.datapages.com/data/specpubs/compapp3/chap04/0027.htm

Olea, R. A. (n.d.). *Geostatistical Glossary and Multilingual Dictionary.* Oxford University Press. Retrieved 10 6, 2023

Olea, R. A. (n.d.). *Geostatistics for Engineers and Earth Scientists.* Kluwer Academic. Retrieved 10 6, 2023

Oliveira. (2013, January 31). Geology of the Rosário–Neves Corvo antiform, Iberian Pyrite Belt, Portugal: new insights from physical volcanology, palynostratigraphy and isotope geochronology studies. *Mineralium Deposita*.

Oliveira, J. T., Rosa, C. J., Pereira, Z., Rosa, D. R., Matos, J. X., Inverno, C., & Andersen, T. (2013). Geology of the Rosário–Neves Corvo antiform, Iberian Pyrite Belt, Portugal: new insights from physical volcanology, palynostratigraphy and isotope geochronology studies. *Mineralium Deposita, 48*(6), 749-766. Retrieved 10 6, 2023, from https://link.springer.com/article/10.1007/s00126-012-0453-0

Oliver, M. A., & Webster, R. (2014). A tutorial guide to geostatistics: Computing and modelling variograms and kriging. *Catena, 113*, 56-69. Retrieved 10 6, 2023, from https://sciencedirect.com/science/article/pii/s0341816213002385

parabol. (n.d.). Retrieved from https://www.parabol.co/templates/sprint-retrospectives/swot-analysis/?utm_term=&utm_campaign=ET+%7C+DSAs+%7C+Catch-All&utm_source=adwords&utm_medium=cpc&hsa_acc=5979328244&hsa_cam=20508327301&hsa_grp=153363080136&hsa_ad=671925603007&hsa_src=g&hsa_tgt=dsa-

Rosa, C. J., Rosa, C. J., McPhie, J., Relvas, J. M., Pereira, Z., Oliveira, T., & Pacheco, N. (2008). Facies analyses and volcanic setting of the giant Neves Corvo massive sulfide deposit, Iberian Pyrite Belt, Portugal. *Mineralium Deposita, 43*(4), 449-466. Retrieved 10 6, 2023, from https://eprints.utas.edu.au/10509

Silva, A. M. (2019). *Tratamento de Matérias Primas e Resíduos II.* Porto.

Somincor. (2023). *Technical Report on the Neves Corvo Mine, Southern Portugal*. Retrieved 10 6, 2023, from https://www.sec.gov/Archives/edgar/data/1377085/000120445907001642/lundintechrep1.pdf

Sphera. (n.d.). *Sphera*. Retrieved from https://sphera.com/glossary/what-is-a-life-cycle-assessment-lca/

Srivastava, R. M. (1994). The Visualization of Spatial Uncertainty. *Seg Technical Program Expanded Abstracts*, 339-345. Retrieved 10 6, 2023, from http://archives.datapages.com/data/specpubs/compapp3/chap24/0339.htm

Stephen J. Bigelow, M. K. (n.d.). *TechTarget* . Retrieved from TechTarget : https://www.techtarget.com/searchcio/definition/SWOT-analysis-strengths-weaknesses-opportunities-and-threats-analysis

Supergeo. (n.d.). *Supergeo*. Retrieved from Supergeo: https://www.supergeotek.com/Spatial_Statistical_ENG_HTML/spherical_mode.htm

Swapp, S. (n.d.). *Scanning Electron Microscopy (SEM)*. Retrieved 10 6, 2023, from University of Wyoming: http://serc.carleton.edu/research_education/geochemsheets/techniques/SEM.html

Tescan. (n.d.). Retrieved from https://www.tescan.com/pt-br/product/sem-for-materials-science-tescan-vega/

Tolcin, A. C. (2022). *Lead.* USGS.

Tolcin, A. C. (2023). *Zinc.* USGS.

Williams, C. K. (1998). *Learning in Graphical Models.* Retrieved 10 6, 2023

Zeiss. (n.d.). *Zeiss*. Retrieved from https://www.zeiss.com/content/dam/z/rms/reference-master/products/electron-ion/sem/geminisem/geminisem460-monitore-insitu.jpg/_jcr_content/renditions/original.image_file.1440.1440.240,0,1680,1440.file/geminisem460-monitore-insitu.jpg

2023

Filipe Amaral Lopes

PARTICLE SIZE ANALYSIS AND 3D MOD-ELING OF MINERALS FOR MINERAL PROCESSING OPTIMIZATION: A CASE STUDY of NEVES-CORVO